Quantum nuclear effects on surfaces and dispersion bonded systems

Erlend Davidson

A dissertation submitted in partial fulfillment

of the requirements for the degree of

Doctor of Philosophy

of the

University College London.

Department of Chemistry

University College London

November 8, 2012

I, Erlend Davidson confirm that the work presented in this thesis is my own. Where information has been derived from other sources, I confirm that this has been indicated in the thesis.

Abstract

Computer simulation methods are established as extremely useful approaches for understanding physical and chemical processes. Density functional theory is one of the most popular theoretical methods used to study a variety of systems, from gas phase molecules to bulk materials and surfaces. However despite its success, there remain challenges that must be resolved before density functional theory is generally applicable across all system types. In particular long range van der Waals dispersion forces and quantum nuclear effects are typically ignored by standard calculations, however as algorithms have matured and fast parallel computing resources are now more widely available it is possible to include these in simulations. We use state of the art methods to include van der Waals dispersion and quantum nuclear effects on a range of well defined model systems. By comparing with experiment whenever possible we provide new insight into how quantum tunnelling, zero point motion and long range dispersion forces can affect physical processes.

Publications

The work presented in this thesis has led to the following publications:

E. R. M. Davidson, A. Alavi, A. Michaelides, Dynamics of quantum tunneling: Effects on the rate and transition path of OH on Cu(110). Phys. Rev. B. **81**, 153410 (2010).

E. R. M. Davidson, J. Klimeš, D. Alfè, A. Michaelides, The combined role of H atom tunneling and van der Waals in the carbon-catalyzed H_2 formation reaction. (*submitted*).

During my Ph.D. studies I also contributed to the following publication:

A. Maniopoulou, E. R. M. Davidson, R. Grau-Crespo, A. Walsh, I. J. Bush, C. R. A. Catlow and S. M. Woodley, Introducing k-point parallelism into VASP. Comput. Phys. Commun. **183**, 1696 (2012).

Acknowledgements

I would like to thank my supervisor, Prof. Angelos Michaelides, for his guidance and discussions, without which the work presented herein would have not been possible. I am aware that my writing and presentation skills have improved greatly over the past four years, and for this I am extremely grateful. I also wish to thank my second supervisor, Prof. Dario Alfè, for helpful discussions and in particular for making available to me his implementation of path-integral molecular dynamics in the VASP code. Once I made modifications to port the code to a recent version of VASP which contained the vdW-DF, this enabled a significant portion of my thesis to exist as it does.

The ICE group has been a very pleasant and stimulating working environment for me, for which I thank the past and present members. Xinzheng Li, Steve Cox and Gabriella Graziano for helpful discussions about chemistry. Ming Ma for interesting questions during group discussions. I am fortunate to have benefited from the vdW-DF implementation in VASP by Jiří Klimeš, and I thank Jiří for useful discussions about VASP and DFT. I also wish to thank Gabriele Tocci for providing a constant supply of good quality coffee beans throughout my Ph.D.

Finally I would like to thank my parents for their support and encouragement.

Contents

List of Figures

List of Tables

Chapter 1

Introduction

Computational science is an extremely powerful tool across many disciplines including but not limited to physics, chemistry, materials and surface science. Accurate calculations at the atomic and molecular scale add valuable insight to experimental data, enabling scientists to virtually see into many physical processes with more fine detail than any experiment can provide [1, 2]. These simulations have, for example, aided the interpretation of scanning-tunnelling microscopy (STM) images [3–5], the identification of infrared absorption spectra [6] and even assisted the determination of reaction mechanisms [7, 8]. As the accuracy and reliability of results from computational studies improves there is a shift towards making real predictions. This is particularly powerful for processes where experimental probes are impossible or prohibitively expensive, such as studies in deep space [9–25], the Earth's core [26–29] and ultrafast processes [30]. There has also been considerable progress in identifying new crystal structures and phases of materials [31–40], which is now having an impact on important industrial and economic issues [41].

A widely discussed contemporary example of the industrial impact of computational materials modelling is in the design of new batteries. In past two decades lithium-ion batteries have become one of the most popular batteries for commercial applications. Ceder *et al.* [42] used electronic structure calculations to predict that the energy density of lithium-ion batteries could be increased by reducing the amount of transition metal in the cell cathode, which they replaced with aluminium. This prediction was used to guide experiments of aluminium doping on $LiCoO_2$,

verifying the calculations [42]. Since then there has been a full scale effort using high-throughput computer simulations to screen thousands of materials for their suitability as a cathode [43]. Another exciting medium for the storage and transportation of energy is hydrogen, however in its standard gaseous state hydrogen has a volumetric energy density which is too low to be efficient for transport. As a result of this, and the potential for hydrogen to be a clean and abundant form of energy, there has been an ongoing effort to find materials capable of storing hydrogen effectively. Computational studies are capable of probing many thousands of similar materials, requiring much less time and expense than experiments on the same scale. In this theme Alapata *et al.* [44] performed over 100 simulations of dehydrogenation reactions where ternary metal hydrides were reacted to form hydrogen. From these calculations they identified five reactions not yet experimentally examined [44], one of which has since been confirmed by experiment [45]. On an even larger scale there is a considerable worldwide effort to design better catalysts for industrial processes with improved selectivity and an increase in catalyst activity. There is a shift towards using simulation with high-throughput computers to characterise new materials, vastly reducing the number of experiments which need to be conducted [46, 47].

Atomistic simulations are generally either *ab initio* or they rely on force fields fitted to empirical data. While empirical force fields are very much faster than *ab initio* calculations they must be manually constructed for each species being studied. Although expensive, computing from first principles enables us to easily study a wide variety of new systems. As a result density functional theory (DFT) has become the workhorse of the materials simulation and condensed matter fields due to relatively modest computational cost coupled with the predictive power it offers. The sustained improvement in algorithms over the last few decades combined with the exponential increase in the availability and speed of computers (from university clusters through to massively parallel national resources) means that impressive DFT calculations can be conducted routinely.

Despite the enormous success of DFT over the past couple of decades there

remain issues concerning the accuracy of the method. It is often said that DFT is exact "in principle", however the reality is that we do not know the true form of exchange and correlation as a functional of the electronic density (this term is called the exchange-correlation functional, more on this later) and so calculations are always approximate. One effect of this approximation, which remains an intriguing challenge to the entire field of computational materials research, is the lack of long-range van der Waals forces in standard calculations. This means DFT will not correctly describe the binding between noble gas atoms [48], and it is generally unsuitable for biological molecules [49]. Traditional attempts to include van der Waals dispersion in DFT involve adding an r^{-6} dependent term (where r is the interatomic distance) at the end of the electronic structure calculation, and while this may give good accuracy in many cases it does suffer from a lack of transferability, blindness to changes in the chemical environment and potentially a poor description of reaction barriers. Methods to include dispersion within the calculation of the electronic structure in DFT are now reaching maturity, with some methods displaying chemical accuracy and impressive transferability between molecules and surface-adsorption systems [50–54]. This exciting development presents the opportunity to successfully apply DFT to systems where it would have previously failed.

Another huge challenge for materials modelling is how to describe the quantum mechanical effects on the nuclei of lighter elements, in particular hydrogen. While DFT treats the electrons quantum mechanically, in calculations it is normally assumed that the nuclei behave classically. The lightest element, hydrogen, is only about 2000 times heavier than an electron and so displays quantum effects such as tunnelling and zero-point motion.

At low temperatures these quantum nuclear effects (QNEs) can dominate over classical (thermal) effects, which can have important implications for a range of systems [55–64]. It has been predicted that quantum mechanical effects can change the nature of the H-bond in water at surfaces, gas phase molecules and in bulk ice [55, 56, 58, 60, 61, 65]. It is also known that H-atoms can tunnel through energy barriers, facilitating proton transfer in enzymes [66, 67], the fast diffusion of hydrogen

at surfaces [68, 69], and the absorption of hydrogen [70–72].

One of the most successful theoretical methods to look at QNEs is path-integral molecular dynamics (PIMD) [62, 73–75]. This is based on the Feynman path-integral formulation of quantum mechanics, where the probability of a particle going from one point to another is calculated as a sum over all the possible paths it can take between these [76]. Although PIMD calculations are computationally expensive they are well suited to run on large parallel computers. As these machines become more accessible to the scientific community, so too do detailed studies of QNEs. This, combined with the recent inclusion of reliable dispersion energies within DFT, means that the time is basically right to consider the effects of quantum nuclei and van der Waals.

The remainder of this thesis is concerned with improving our understanding of these effects. We do this by studying well-defined model system, meaning real physical systems for which experimental reference data exists. These systems are simple enough to be computationally tractable, yet they are in and of themselves of importance to surface science. In chapter 2 an overview of the theoretical methods, from DFT to PIMD, used to examine these systems is given. In chapter 3 the flipping of a hydroxyl adsorbed on Cu(110) due to quantum tunnelling is discussed. There are several different paths along which the hydroxyl can flip, while still giving the same inital and final structures. Using a semiclassical approach the rates of tunnelling through the associated barriers are computed, and it is concluded that the tunnelling path is quite different from the classical reaction coordinate. The rates obtained agree well with experimental findings. Chapter 4 deals with the effects of dispersion, QNEs and thermal effects on the water dimer adsorption at Cu(110). While dispersion and thermal effects have little measurable effect, QNEs are found to weaken the H-bond in the dimer, consistent with recent predictions for H-bonded gas phase molecules and solid systems [55]. The combined effect of van der Waals dispersion and QNEs is studied in chapter 5. Here we look at the intriguing problem of how a H atom can chemisorb at graphene when the computed barrier is considered too high. It is found that both dispersion and QNEs significantly lower this barrier

at low temperatures, making the hydrogenation of graphene much easier than previously predicted and enabling the carbon-catalyzed formation of H_2 in space. In chapter 6 ice Ih is examined for any possible proton transfer events that could be mediated by quantum tunnelling, motived by a recent experimental paper [77]. The proton transfer barriers computed are too high for tunnelling to be a significant process, although the low temperature annealing of Bjerrum defects may be facilitated by QNEs. The final chapter summarises the thesis and presents an outlook for our future understanding of these effects.

Chapter 2

Theory

The work in this thesis would not have been possible were it not for the development of DFT over the past several decades. DFT is a method to model the ground state electronic structure of atomic and molecular systems, using the electron density at each point in space. It has become an extremely popular method due to the accuracy it offers compared with its favourable computational cost. The following few sections will describe the principles of DFT, from its theoretical basis (the Hohenberg-Kohn and Kohn-Sham papers [78, 79]) and the more recent developments which have been necessary to make it a computationally useful method. The later part of this theory chapter covers ways to obtain the estimates for the classical and quantum mechanical transition rates for chemical processes.

2.1 Quantum mechanics for atoms and molecules

To describe the behaviour of atomic and molecular systems we are interested in solving the time-independent Schrödinger equation,

$$\hat{H}\Psi(\boldsymbol{r}, \boldsymbol{R}) = E\Psi(\boldsymbol{r}, \boldsymbol{R}), \tag{2.1}$$

where the r, R are the electronic and nuclear coordinates respectively. $\Psi(\boldsymbol{r}, \boldsymbol{R})$ is the quantum mechanical wavefunction with energy E. The non-relativistic Hamil-

tonian in atomic units (i.e. $m_e = \hbar = z_e = 1$) is,

$$\hat{H} = -\frac{1}{2}\sum_{i}^{N_e}\nabla_i^2 - \frac{1}{2}\sum_{A}^{N_n}\frac{1}{M_A}\nabla_A^2 - \sum_{i,A}^{N_e,N_n}\frac{Z_A}{|\boldsymbol{r}_i - \boldsymbol{R}_A|} + \sum_{i,j}^{N_e,N_e}\frac{1}{|\boldsymbol{r}_i - \boldsymbol{r}_j|} + \sum_{A,B}^{N_n,N_n}\frac{Z_A Z_B}{|\boldsymbol{R}_A - \boldsymbol{R}_B|}, \tag{2.2}$$

where the indices i, j run over electrons while index A, B counts nuclei, such that $i \neq j$ and $A \neq B$. N_e, N_n are the number of electrons and nuclei respectively, Z_A is the nuclear charge and M_A is the nuclear mass. The terms in Eq. 2.2 are (from left to right) the kinetic energy of the electrons and the kinetic energy of nuclei. The final three terms are for the Coulombic interactions of the electrons with the nuclei, the electrons with other electrons and finally the nuclei with each other.

In the following we will describe one very popular method, DFT, that enables us to solve the time-independent Schrödinger equation of atomic and molecular systems for the quantum mechanical wavefunction and energy. What we present here is an overview of the DFT method, an extensive explanation of all aspects of DFT can be found in many books (in particular refs. [80, 81]).

2.2 Born-Oppenheimer approximation

The task of determining the quantum mechanical wavefunction of a molecule is extremely challenging. The Schrödinger equation of a typical molecule would consist of many hundreds of degrees of freedom, which is generally unsolvable even given the fastest computers available today. Recognising that the nuclei are many thousands of times heavier than the electrons, it is acceptable to separate the total Hamiltonian into two parts solving for the nuclear and electronic degrees of freedom separately. The Born-Oppenheimer approximation [82] separates the electronic and nuclear degrees of freedom so that the electronic and nuclear Schrödinger equations can be solved separately. Therefore the total wavefunction can be written,

$$\Psi^{e,n}(\boldsymbol{r}, \boldsymbol{R}) = \Psi^{n}(\boldsymbol{R})\Psi^{e}(\boldsymbol{r}, \boldsymbol{R}), \tag{2.3}$$

with associated total energy,

$$E^{e,n} = E^{n} + E^{e}, \tag{2.4}$$

where $\Psi^{e,n}$, $E^{e,n}$ are the total wavefunction, energy and the superscript n or e indicate the nuclear or electronic component of the wavefunction or energy. In atomic units the electronic Hamiltonian is,

$$\hat{H}(\boldsymbol{r}, \boldsymbol{R}) = -\frac{1}{2}\sum_{i}^{N_e} \nabla_i^2 - \sum_{i,A}^{N_e,N_n} \frac{Z_A}{|\boldsymbol{r}_i - \boldsymbol{R}_A|} + \sum_{i,j}^{N_e,N_e} \frac{1}{|\boldsymbol{r}_i - \boldsymbol{r}_j|}, \tag{2.5}$$

where the terms have the same meaning as in Eq. 2.1. The nuclear Hamiltonian can then be written,

$$\hat{H}(\boldsymbol{R}) = -\frac{1}{2}\sum_{A}^{N_n} \frac{1}{M_A}\nabla_A^2 + E_{el}(\boldsymbol{R}) + \sum_{A,B}^{N_n,N_n} \frac{Z_A Z_B}{|\boldsymbol{R}_A - \boldsymbol{R}_B|}, \tag{2.6}$$

where M_A is the nuclei mass in atomic units and $E_{el}(\boldsymbol{R})$ is the potential felt by the nuclei due to the electrons (which comes from the solution of the electronic Schrödinger equation). It should be noted that there are situations were the Born-Oppenheimer approximation fails, for example the dissociative adsorption of H_2 or O_2 at surfaces [83–86]. Furthermore the relatively large mass of the nuclei motivates us to consider them as localised, point-like particles. This assumption works very well for the heavier elements, however for hydrogen and its isotopes at low temperature there can be significant quantum mechanical delocalisation of the nuclei, leading to effects such as tunnelling and shared protons in hydrogen bonds.

We will now discuss how one practically calculates the electronic energy from the Hamiltonian in Eq 2.5.

2.3 Density functional theory

The work presented here relies on the advances made during the last 50 years in developing an efficient and accurate computational tool for ground-state *ab initio* electronic structure calculations. DFT reduces the many-electron problem to something much more computationally feasible by replacing the interactions between electrons with a mean-field which each electron feels. It is exact in principle, however an approximate form of the exchange-correlation functional is needed (later). DFT is made possible due to the Hohenberg and Kohn theorem [78], which states that the ground state electronic energy is uniquely determined by the ground state

electron density $n(\mathbf{r})$ (Eq. 2.7).

$$\begin{aligned} \Psi_0 &= \Psi[n_0] \\ E_0^e &= E^e[n_0], \end{aligned} \tag{2.7}$$

where Ψ_0 is the ground state wavefunction, E_0^e is the ground state electron energy, and n_0 is the ground state electron density. To see how this is useful consider the total electronic energy as a functional of the electron density, broken down in to its various components,

$$E^e[n] = T^e[n] + V^{e-n}[n] + E^{Hartree}[n] + E^{xc}[n], \tag{2.8}$$

where $T^e[n]$ is the kinetic energy functional, V^{e-n} is the electrostatic potential felt by the electrons due to the nuclei, and the last two terms are the Coulombic (Hartree) energy and the exchange-correlation energy. The Hartree energy is the Coulombic interaction between electrons, in terms of electron density,

$$E^{Hartree}[n] = \frac{1}{2} \int \int \frac{n(\boldsymbol{r}) n(\boldsymbol{r'})}{|\boldsymbol{r} - \boldsymbol{r'}|} \, d^3\boldsymbol{r} \, d^3\boldsymbol{r'}, \tag{2.9}$$

where the integrations with respect to $\boldsymbol{r}$ and $\boldsymbol{r'}$ are over the entire spatial domain. The electron exchange interactions and correlation effects are accounted for by the exchange-correlation functional $E^{xc}[n]$.

An exact and general density functional for the exchange-correlation energy, and for the kinetic energy of many interacting electrons is not known. Kohn and Sham suggested that the kinetic energy functional be replaced by the kinetic energy of non-interacting electrons, $T_s[n]$, and the unknown interacting part of the kinetic energy may be absorbed by the exchange-correlation energy functional, which is now the only undefined quantity [79]. The ability to write the kinetic energy of interacting electrons in a consistent, and in principle exact, way like this overcomes one of the biggest shortfalls of Thomas-Fermi theory [87, 88]. This makes it possible to use the Schrödinger equation of a single electron moving in a mean-field representing the average interaction of all the other electrons in the system. This

simplification is achieved by defining an effective potential $V^{eff}(\boldsymbol{r})$,

$$\begin{aligned} V^{eff}(\boldsymbol{r}) &= \frac{\delta}{\delta n(\boldsymbol{r})}\left\{V^{e-n}[n] + E^{Hartree}[n] + E^{xc}[n]\right\} \\ &= V^{e-n}(\boldsymbol{r}) + \int \frac{n(\boldsymbol{r'})}{|\boldsymbol{r}-\boldsymbol{r'}|} d^3\boldsymbol{r'} + \frac{\delta E^{xc}[n]}{\delta n(\boldsymbol{r})}, \end{aligned} \tag{2.10}$$

which is subsequently used in the single particle Schrödinger equation,

$$\left(-\frac{1}{2}\nabla^2 + V^{eff}(\boldsymbol{r})\right)\phi_0^i(\boldsymbol{r}) = E_0^i(\boldsymbol{r})\phi_0^i(\boldsymbol{r}). \tag{2.11}$$

This introduces the ground state Kohn-Sham orbital ϕ_0^i for the i^{th} electron. The electron density at position $\boldsymbol{r}$ can be calculated as,

$$n(\boldsymbol{r}) = \sum_{i=1}^{N} |\phi_0^i(\boldsymbol{r})|^2. \tag{2.12}$$

The second Hohenberg and Kohn theorem [78] states that the total electronic energy functional obeys a variational principle, and so any electron density n which is not the ground state density will give a higher energy (i.e. for all $n \neq n_0,\ E[n] > E[n_0]$). The minimum electron density (and ground state energy) are computed by iteratively applying equations 2.11 and 2.12, until the density $n(\boldsymbol{r})$ or associated electronic energy $E^e[n(\boldsymbol{r})]$ reach convergence. The Hohenberg and Kohn theorems therefore provide the basis for the evaluation of the ground state energy of a system of interacting electrons.

2.3.1 Exchange-correlation energy

The calculation of the electronic energy up until this point is exact within the Born-Oppenheimer approximation. Unfortunately we do not know the exact form of the exchange-correlation functional $E^{xc}[n]$, and so it is necessary to approximate it. Two of the most popular exchange-correlation functionals in use within the materials science community today are the local-density approximation (LDA) [79], and a class of generalised gradient approximation (GGA) [89–92].

The LDA divides the simulation box into small cells, within which it is assumed the electronic density is uniform. Since we know the exchange-correlation energy of the homogeneous electron gas for any density, either from analytic means or from

quantum Monte Carlo simulations [93], the energy of each cell can be calculated. The LDA is computationally inexpensive, however it performs poorly for atoms, molecules and systems with quickly varying densities. Despite this the LDA has been successful in describing a number of systems, including metal surfaces [94]. Written as a functional of the electron density, the LDA is,

$$E_{LDA}^{xc}[n] = \int n(\boldsymbol{r})\, \epsilon[n(\boldsymbol{r})]\, d^3\boldsymbol{r}, \tag{2.13}$$

where $\epsilon[n]$ is the exchange-correlation energy per electron in the homogeneous electron gas of density n.

GGAs try to account for varying electron densities by including the gradient of the density at each cell [95]. A general form for the GGA class of exchange-correlation functionals is,

$$E_{GGA}^{xc}[n] = \int n(\boldsymbol{r})\, \epsilon[n(\boldsymbol{r})\nabla n(\boldsymbol{r})]\, d^3\boldsymbol{r}, \tag{2.14}$$

where ∇ is the vector differentiation operator. These often give an improved description of bulk systems, atomisation energies and barriers compared with the LDA. However surface energies computed with the GGA are actually less accurate compared with the LDA [96].

The natural development after GGA is to include the second derivative (Laplacian) of the density, forming what is called a meta-GGA. Examples include PKZB, TPSS and revTPSS exchange-correlation functionals [97–99]. PKZB performs well for atomisation energies, surface energies, and lattice constants but it contains one empirical parameter and overestimates molecular bond lengths [100]. TPSS gives good values for the atomisation and surface energies, but predicts lattice constants that are too long [98]. The "revised TPSS" (revTPSS) gives good results for the lattice constants, surface energies and atomisation energies of materials [99].

Another advance in exchange-correlation functionals has been to include a certain amount of exact exchange, forming what is known as hybrid functionals (since these are a mix of Hartree-Fock and density functional theory). These alleviate part of the self-interaction problem which affects the atomisation energies from DFT,

and give an improved estimate of reaction barriers. The most commonly used hybrid functionals are PBE0, HSE and B3LYP [101–103], however due to the computational expense of evaluating exact exchange within a plane-wave code these are normally used to benchmark values from other exchange-correlation functionals, or they are more commonly used in codes which rely on localized basis sets.

These types of exchange-correlation functional make use only of local information of the density, and so miss long-range correlation effects which are responsible for London dispersion effects. Often the correction in energy due to dispersion is relatively small compared with the energies of chemical bonds, and so this is sometimes not a large problem. There are however systems across a broad range of the physical sciences in which these weak dispersion forces play an important role, and correspondingly there has been growing interest in finding approaches to include these within DFT.

At long separations r the dispersion energy can be obtained from second order perturbation energy,

$$E_{disp} = -\frac{C_6}{r^6} - \frac{C_8}{r^8} - \frac{C_{10}}{r^{10}}. \tag{2.15}$$

One of the simplest methods for approximately including dispersion involves adding the leading $1/r^6$ correction term in the form shown in Eq. 2.16 to the total electronic energy,

$$E_{disp} = -\frac{1}{2}\sum_{i}^{N}\sum_{j}^{N}\left\{\frac{C_6^{ij}}{|\boldsymbol{r}^i - \boldsymbol{r}^j|^6} f(|\boldsymbol{r}^i - \boldsymbol{r}^j|)\right\}, \tag{2.16}$$

which is a pairwise additive summing over the N atoms, with each pair of atoms i or j separated by $\boldsymbol{r}^i - \boldsymbol{r}^j$. C_6^{ij} is the dispersion coefficient for the atomic pair i, j and $f(\boldsymbol{r})$ is a damping function to effectively switch off dispersion interactions at close distances, typically around the length of a chemical bond. Two methods based on this approach, DFT-D and DFT-D2 [104, 105], have been very popular due to the ease with which they can be implemented in codes, and for having practically no computational overhead. The main limitation of this approach is that the C_6 coefficients are kept constant for each set of elements, while in reality these should vary to reflect changes to the local chemical environment.

DFT-D3 [106] includes both C_6 and C_8 terms. The dispersion coefficients are computed using the Casimir-Polder formula [107] with polarisabilities determined using time-dependent DFT calculations. Changes in the atomic environment are then approximately accounted for by scaling the dispersion coefficients with the number of neighbouring atoms. The method of Tkatchenko and Scheffler [108] approximates the effect of the atomic environment by scaling the reference dispersion coefficients C_6^{free} with the volume V change of the atom in the bound and free states (Eq. 2.17).

$$C_6 = \left(\frac{V}{V^{free}}\right)^2 C_6^{free}. \tag{2.17}$$

The method we use in this thesis is the van der Waals density functional (vdW-DF) developed in the groups of Langreth and Lundqvist [109], with modifications by Klimeš *et al.* [50]. The vdW-DF exchange-correlation functional is noteworthy as it includes dispersion directly in DFT at the electronic structure level, and applies to all elements in the periodic table at arbitrary distances. The vdW-DF exchange-correlation functional is written,

$$E^{xc}[n] = E_x^{GGA}[n] + E_c^{LDA}[n] + E_c^{nl}[n], \tag{2.18}$$

with,

$$E_c^{nl}[n] = \frac{1}{2}\int\int d^3\boldsymbol{r}_1 d^3\boldsymbol{r}_2\, n(\boldsymbol{r}_1)\phi(q_1 r_{12}, q_2 r_{12})n(\boldsymbol{r}_2). \tag{2.19}$$

The term r_{12} is the magnitude of the position vector connecting over regions of density, i.e. $r_{12} = |\boldsymbol{r}_1 - \boldsymbol{r}_2|$, and q_1, q_2 are values of a functional of the form $q_i[\, n(\boldsymbol{r}_i), |\nabla n(\boldsymbol{r}_i)|\,]$. The form of the correlation kernel ϕ is chosen such that $E_c^{nl} \equiv 0$ for any system with constant density and at large separations an r_{12}^{-6} dependence is achieved.

In the original vdW-DF the exchange part of revPBE was used for E_x^{GGA}. It was noticed by Klimeš *et al.* [50] that the accuracy of vdW-DF could be improved by modifying the exchange functional. In particular two optimised exchange functionals, based on Becke88 and PBE, were developed by fitting to higher order benchmark data to yield more accurate binding energies. These exchange-correlation functionals are referred to as optB88-vdW, optPBE-vdW, and the original vdW-DF will be called revPBE-vdW throughout this work (since it uses exchange from

revPBE). Benchmark studies on the performance of optPBE-vdW, including the application to adsorption, can be found in refs. [50, 52–54].

2.3.2 Basis functions

Basis functions are a means to represent an electronic wavefunction in a form suitable for computation. These can be either localised basis functions such as a linear combination of gaussians, or as plane-waves. All of the results presented in this thesis use the latter, which we now describe here. For a periodic system, the use of plane-waves to represent the electronic structure follows naturally from Bloch's theorem [110]. For an electron experiencing a periodically repeating potential its wavefunction may be written as the the product of a plane-wave function and a Bloch function $f(\boldsymbol{r})$ with periodicity equal to that of the underlying potential (Eq. 2.20),

$$\phi(\boldsymbol{r}) = e^{i\boldsymbol{k}.\boldsymbol{r}} f(\boldsymbol{r}) \text{ with } \boldsymbol{r} = j\boldsymbol{a}, \tag{2.20}$$

for some integer j and primitive lattice vector $\boldsymbol{a}$. Within the Brillioun zone (when $|\boldsymbol{k}| \leq \pi/a$), varying values of $\boldsymbol{k}$ yield different wavefunctions corresponding to different ways of overlapping the electronic orbitals. Values of $\boldsymbol{k}$ outside of this range yield repeated wavefunctions, and thus the energy eigenvalues are periodic, $\varepsilon(\boldsymbol{k}) = \varepsilon(\boldsymbol{k} + \boldsymbol{K})$, where $\boldsymbol{K}$ is the reciprocal lattice vector. In an infinite surface, or bulk, system the electronic bands are completely continuous across $\boldsymbol{k}$-space. However in practice we can only sample a reduced set of $\boldsymbol{k}$-points determined through convergence tests of important properties of the system (be that surface energy, adsorption energy or a geometric feature such as a bond length). All the work in this thesis samples $\boldsymbol{k}$-space based on points selected by the Monkhorst-Pack scheme [111].

2.3.3 Describing the nuclear potential

What has been described so far would be enough to calculate the total electronic energy given a potential due to the nuclei of (V^{e-n}). However, close to the nucleus this potential would be very steep, leading to a very high kinetic energy of electrons and a quickly oscillating wavefunction. The number of plane-waves required to accurately describe this wavefunction would be extremely large, requiring inordinate

amounts of both computational time and memory. Since usually the electrons nearest the nuclei aren't involved in the chemical bonding of atoms this issue is resolved by treating the electrons within a core region surrounding the nucleus differently, with the purpose of making the Kohn-Sham wavefunctions smooth within this region.

An early approach was the norm-conserving pseudopotential method, where the real Coulombic potential is replaced by a pseudo-potential which gives a pseudowavefunction with the same chemistry as the original, physical, wavefunction. There are some requirements a pseudopotential must satifsy. As the wavefunctions outside of the core region are chemically important we need the pseudowavefunction and true wavefunctions in this region to match. The pseudopotential method must also conserve the charge (number of electrons) within the core region. If r_c gives the cutoff radius, so that $r < r_c$ indicates core electrons and $r > r_c$ indicates valence electrons, then a norm-conserving pseudopotential must satifsy,

$$\int_0^{r_c} d\boldsymbol{r}\, |\phi_{AE}(\boldsymbol{r})|^2 = \int_0^{r_c} d\boldsymbol{r}\, |\phi_{PS}(\boldsymbol{r})|^2, \tag{2.21}$$

where $\phi_{AE}(\boldsymbol{r})$ and $\phi_{PS}(\boldsymbol{r})$ are the all-electron and pseudowavefunctions respectively. However for wavefunctions without any nodes this is not helpful, as the pseudowavefunction will look very similar to the original wavefunction. For this reason newer methods to treat the core electrons are often used.

In ultrasoft pseudopotentials the norm-conservation constraint is relaxed by removing the troublesome core electrons from the self-consistent cycle and replacing these with an augmentation charge [112]. Outside of the core region, the valence electrons are described by a smooth pseudopotential similar to the norm-conserving case. By treating the core and valence regions separately ultrasoft pseudopotentials allow for much more aggressive softening than norm-conserving pseudopotentials. This therefore allows for a huge reduction in the size of the basis set required, and therefore also the kinetic energy cutoff.

The projector augmented wave (PAW) approach was developed [113] to unify all-electron and pseudopotential methods by defining a new auxillary wavefunction which is smooth and easily represented in a plane-wave basis. The auxillary wave-

function $\tilde{\Psi}$ and physical wavefunction Ψ are related by a transformation operator $\hat{\mathcal{U}}$, and its inverse $\hat{\mathcal{T}}$,

$$\tilde{\Psi}(r) = \hat{\mathcal{U}}\Psi(r) \iff \Psi(r) = \hat{\mathcal{T}}\tilde{\Psi}(r). \tag{2.22}$$

The expectation value of a physical observable can be written in terms of the auxillary and physical wavefunctions,

$$\langle A \rangle = \sum_n \langle \Psi_n | \hat{A} | \Psi_n \rangle = \sum_n \langle \tilde{\Psi}_n | \mathcal{T}^\dagger \hat{A} \mathcal{T} | \tilde{\Psi}_n \rangle, \tag{2.23}$$

The Schrödinger equation in terms of the auxillary wavefunctions becomes,

$$\mathcal{T}^\dagger \hat{H} \mathcal{T} | \tilde{\Psi}_n \rangle = \mathcal{T}^\dagger \mathcal{T} | \tilde{\Psi}_n \rangle E_n. \tag{2.24}$$

Outside of the augmentation radius r_c the physical and auxillary wavefunctions must be identical. To write a transformation operator which satifies these requirements a projector function $\langle \tilde{p}_i |$ is introduced such that,

$$\langle \tilde{p_i} | \tilde{\phi_j} \rangle = \delta_{i,j}, \text{ and within } r_c\text{: } \sum_i |\tilde{\phi_i}\rangle\langle \tilde{p_i}| = 1. \tag{2.25}$$

The transformation operator is then written,

$$\mathcal{T} = 1 + \sum_R \mathcal{S}_R, \text{ where } \mathcal{S}_R = \sum_i (|\phi_i\rangle - |\tilde{\phi_i}\rangle)\langle \tilde{p_i}|, \tag{2.26}$$

such that the all electron wavefunction can be written as,

$$|\Psi\rangle = |\tilde{\Psi}_n\rangle + \sum_i (|\phi_i\rangle - |\tilde{\phi_i}\rangle)\langle \tilde{p_i}|\tilde{\Psi}\rangle \tag{2.27}$$

2.4 Transition state theory

There is a disparity between the time-scales of many real physical processes and the time-scales we can practically simulate with DFT based molecular dynamics (MD). A typical DFT-MD time-step would be of the order of 1 fs, and with current hardware we may routinely run for approximately $100,000$ MD steps. In order to study processes which occur on a longer timescale it is necessary to make use of transition state theory (TST). In a simple transition (or reaction) there are three regions in

which the system can exist, the initial state which we call the reactants, a final state which we call the products and an energy barrier (transition state) separating the reactants from the products. By knowing this energy barrier it is possible to compute an approximate rate at a given temperature (T) using the empirical Arrhenius equation,

$$k(T) = A\, e^{-E_a/k_B T}, \tag{2.28}$$

where E_a is the activation energy for the reaction, k_B is the Boltzmann constant and A is an experimentally determined prefactor which corresponds to the rate of the reaction as $T \to \infty$. The units of A determine the units of the rate constant, which for a first order reaction is s^{-1}. Thus A is often thought of as the attempt frequency of the reaction, while the dimensionless $exp(-E_a/k_B T)$ is the probability of one of these attempts resulting in a successful reaction. It is clear that either reducing the activation energy required (E_a) or increasing the temperature (T) will result in a faster reaction rate.

The purpose of TST is to provide a purely theoretical means to compute the reaction rate constant at a particular temperature. All successful reactions must pass from the reactant state to the product state by going through a transition state (TS), which is a dividing surface between them with its plane perpendicular to the direction of the reaction coordinate at the saddle point. For a generalised spatial coordinate $q(t)$, and a dividing surface $q^\dagger$, Eyring's TST can be written [114],

$$\begin{aligned} k_{\text{TST}} &= \frac{\langle \dot{q}\, \Theta(\dot{q})\, \delta(q^\dagger - q) \rangle}{\langle \Theta(q^\dagger - q) \rangle}, \\ &= \text{rate of going from TS to products } \times \text{ probability of being at TS}. \end{aligned} \tag{2.29}$$

The denominator is the average population of reactants and the numerator is the reactive flux assuming no recrossing ($\Theta(\dot{q})$ counts every reaction which crosses the transition state to the products). The average velocity $\langle v \rangle$ is $\sqrt{k_B T/2\pi m}$, and so the TST rate constant becomes,

$$k_{\text{TST}} = \langle v_P \rangle P_R^\dagger = \sqrt{\frac{k_B T}{2\pi m}} \frac{e^{-E_a/k_B T}}{Q}, \tag{2.30}$$

where v_P is the forward velocity (towards products), $P_R^\dagger$ is the probability for reactant states to reach the transition state and Q is the reactants partition function.

Making a one-dimensional harmonic approximation at the well bottom for the reactants gives,

$$Q = \sqrt{\frac{2\pi k_B T}{m\omega_0^2}}, \tag{2.31}$$

and a one-dimensional harmonic rate constant,

$$k_{\text{HTST}} = \frac{\omega_0}{2\pi} e^{-E_a/k_B T}. \tag{2.32}$$

In more than one dimension,

$$k_{\text{TST}} = \frac{k_B T}{h} \frac{Q^\dagger}{Q} e^{-E_a/k_B T}, \ \frac{Q^\dagger}{Q} \simeq \frac{\prod_{i=1}^{3N-1} k_B T/\hbar\omega_i^\dagger}{\prod_{i=1}^{3N} k_B T/\hbar\omega_i}. \tag{2.33}$$

This leads to an expression for the harmonic rate constant,

$$k_{\text{HTST}} = \frac{\prod_{i=1}^{3N} \omega_i}{\prod_{i=1}^{3N-1} \omega_i^\dagger} e^{-E_a/k_B T}. \tag{2.34}$$

The best estimate of the rate is obtained by finding the dividing surface that gives the lowest rate constant. However this will still be an overestimation of the real rate, since recrossing of states from the products back towards reactants is not accounted for.

2.5 Nudged elastic band

Eq. 2.34 provides a means to compute a rate from theory if we know the activation energy E_a and the vibrational modes at the top of the barrier. This requires that we know the transition state for the reaction. Several methods have been developed to locate transition states, based typically on following the minimum mode from the reactants [115, 116], or optimising a chain of states from the initial state to the final state [117–120]. In this work we use the climbing image nudged elastic band (CI-NEB) method [119] since this gives us the transition state and a pathway for the reaction, called the minimum energy path (MEP). The CI-NEB is also well suited to running on modern supercomputers since we exploit parallelism across the images.

The basic elastic band method simply involves a number of replicas of the system (called images), and choosing these images along some trial reaction coordinate going from the initial state to the final state. The neighbouring images are

connected by harmonic springs, with zero natural length, so that each image experiences a force from the underlying potential energy surface, and from the springs. The overall energy of the elastic band is then minimised to give a reaction path, i.e. by minimising,

$$E_{\text{band}} = \sum_{i=0}^{N} V(\boldsymbol{r}_i) + \sum_{i=0}^{N-1} \frac{k}{2}(\boldsymbol{r_i} - \boldsymbol{r_{i+1}})^2, \tag{2.35}$$

where N is the number of images, $V(\boldsymbol{r}_i)$ is the potential of the i^{th} image positioned at $\boldsymbol{r}$ and k is the spring constant of the elastic band. The first and last image, corresponding to $i = 0$ and $i = N$, are always kept fixed. There are two problems with the basic elastic band method which mean it does not give the correct transition state [8, 118, 121]. The first of these is that for a finite number of images the springs pull the chain so that there is corner-cutting of the MEP at the saddle point. The basic elastic band may also fail for a curved reaction coordinate even for an infinite number of images, since there will be a component of force orthogonal to the MEP [8].

These problems are resolved by the nudged elastic band (NEB) method [8, 118], which uses a projection of the spring force tangential to the chain, and a perpendicular projection of the forces from the underlying potential energy surface. The CI-NEB is a small modification to NEB for the highest energy image in which the spring force is neglected and the parallel component of the force parallel to the potential energy surface is negated to push the image up the chain to the transition state [119]. The spacing between images on one side of the chain is likely to be slightly altered by this, and so to keep this to a minimum normally a short NEB (without a climbing image) is run before CI-NEB is used.

Once an accurate transition state has been located, the barrier for a transition E_a is just the difference in energies between this state and the initial state, i.e. $E_a = E_{TS} - E_{IS}$.

2.6 Harmonic quantum transition state theory

The harmonic quantum transition state theory (HQTST) method, also known as instanton, provides a means to account for quantum tunnelling through an energy bar-

rier E_a. The instanton method is derived from the Feynman path integral approach to quantum mechanics, where transition probabilities are determined from a sum over all possible paths between the initial and final states,

$$\int e^{iS[x]/\hbar}\,[dx], \quad S[x] = \int_0^t T - V\,dt \tag{2.36}$$

The functional $S[x]$ is the classical action which is the integral of the Lagrangian ($\mathcal{L} = T - V$, where T and V are the kinetic and potential energy respectively) with respect to time t. The $[dx]$ term indicates an integration over all paths.

In this form Eq. 2.36 is not useful for numerical computation, as it represents an infinite number of nested integrals of an oscillating function, over all of space and time. The standard treatment is to take only the closed-paths where the initial and final states are the same and make a Wick rotation ($\tau = it$). This transforms to Euclidean space-time, and the path integral becomes,

$$\int e^{-S_{eu}[x]/\hbar}\,[dx], \quad S_{eu}[x] = \int_0^\tau T + V\,d\tau. \tag{2.37}$$

This form of the path integral converges exponentially, as the most important paths - those which contribute most to the integral - have been brought to the fore. Discretising the action,

$$S_{eu}[x] = \Delta\tau \sum_i^N \frac{1}{2} m \left(\frac{x_{i+1} - x_i}{\Delta\tau}\right)^2 + V(x_i), \tag{2.38}$$

and making the substitution $k(T) = mN(k_B T/\hbar)^2$, the action becomes,

$$\begin{aligned} S_{eu}[x] &= \hbar\,\beta\,V^{eff}(x,T), \\ V^{eff}(x,T) &= \frac{1}{2}\,k(T) \sum_i^N \left(\frac{x_{i+1} - x_i}{\Delta\tau}\right)^2 + \frac{V(x_i)}{N}. \end{aligned} \tag{2.39}$$

The weight $exp(-S_{eu}[x]/\hbar)$ of each path in Eq. 2.37 resembles the Boltzmann factor $exp(-E/k_B T)$ for a classical particle of energy E and temperature T. The quantum mechanical system has now been refactored into an infinite number of classical replicas connected by springs in a ring-polymer indicative of a necklace (and so the replicas are often called beads). Since the harmonic springs connecting each classical replica to its neighbour are mass and temperature dependent the ring-polymer

collapses to recover a single (classical) system at high temperatures or large particle mass. The external potential experienced by each bead is the potential experienced by the quantum system divided by the number of beads (N).

Gillan [122] recognised that the quantum partition function for a system at the top of a barrier could be obtained by constraining the centroid of the ring-polymer to the TS, enabling the use of TST based methods for the rate constant. This method was generalised to work on an asymmetric double well potential [123, 124] and later developed into the HQTST method (also known as instanton or ImF theory) [125]. The quantum mechanical rate is extracted from the HQTST method by making a harmonic expansion of $S_{eu}[x]$ around the minimum action path (MAP),

$$k^{HQTST} = \frac{1}{Q}\sqrt{\frac{S_0}{2\pi\hbar}}\frac{1}{\Delta\tau|\prod_i \omega_i|}e^{-S_{eu}[x]/\hbar}, \tag{2.40}$$

where S_0 is the action of a free particle, ω_i and S are the normal modes and centroid energy of the ring-polymer respectively.

2.7 Path-integral molecular dynamics

To obtain quantum mechanical observables from Eq. 2.38 and 2.39 it is necessary to generate a (very) large number of independent configurations of the ring-polymer. This can be done effectively using Monte Carlo sampling or MD with fictitious time and momentum. For example, to sample ring-polymer configurations with Metropolis Monte Carlo one bead is moved by a small random amount and this is then accepted with probability $exp(-\Delta S/k_B T)$ (ΔS is the change in action resulting from the move) [126–128]. Then the next bead in the ring-polymer is moved, and so on along the entire ring-polymer. While this works it only allows for local changes in configuration, and so subsequent Monte Carlo steps lead to very similar states. There are Monte Carlo methods to reduce this correlation between configurations, for example hybrid Monte Carlo which uses fictitious molecular dynamics to locate a new trial configuration followed by an accept-reject step similar to Metropolis [129–131]. However since DFT provides ionic forces, normally we sample path-integrals with molecular dynamics, the basics of which we describe now (see ref. [132, 133] for a detailed explanation). In order to introduce molecular

dynamics sampling the effective potential in Eq. 2.39 is combined with a fictitious kinetic energy term,

$$\mathcal{L}_{eu} = \sum_{i}^{N} \left[\frac{p_i^2}{2m'} + \frac{1}{2}\, k(T) \left(\frac{x_{i+1} - x_i}{\Delta\tau} \right)^2 \right] + \frac{V(x_i)}{N}, \tag{2.41}$$

and subsequently the following equations of motion,

$$\dot{x}_i = \frac{p_i}{m'}\,, \quad \dot{p}_i = -k(T)(2x_i - x_{i+1} - x_{i-1}) - \frac{1}{N}\frac{\partial V(x_i)}{\partial x_k}. \tag{2.42}$$

These are propagated by a leapfrog or Verlet integration scheme in the presence of a thermostat, for instance Andersen or Langevin [134], so as to sample paths from the canonical partition function.

Note that we are free to choose m' as we like, as it does not affect equilibrium quantities. In practice we use a finite number of ring-polymer beads which are determined by convergence tests and comparing against benchmark simulations. In practical terms, each bead is an independent DFT electronic minimisation. Once the electronic structure is determined the ionic forces for each bead are a sum of the forces from the electrons and the spring forces from neighbouring beads. PIMD can therefore be parallelised over a relatively large number of processes relatively easily. However as there is no guarantee that the electronic structure of each bead will take the same amount of time to converge, load balancing can limit its efficiency.

There is one more important issue before eqns. 2.42 are practical for a real simulation. For a finite number of beads (N), there is a spectrum of vibrational modes up to a maximum of $4Nk_BT/\hbar$, and so for reasonably large N we require a small MD time-step. This means a simulation would have to be run for very many MD steps in order to include the slower vibrational modes of the ring-polymer. Two commonly used solutions involve a change of variables via the staging transformation, or similarly a normal-mode transformation [130, 135]. These select fictitious masses m' in Eq. 2.41 such that there is only one harmonic frequency along the ring-polymer, ensuring that all modes are sampled. In recent years advanced thermostatting schemes have emerged to speed up ring-polymer convergence [136, 137]. Although these are not used in this work they are a promising development for future *ab initio* PIMD calculations.

It should be emphasized that there is no real time dynamics in PIMD. Each bead represents an imaginary time slice and the molecular dynamics sampling is purely to generate new ring-polymer states. Physical insight from PIMD is gained by averaging observables over the course of a long simulation, for example a spatial probability distribution can be obtained by keeping a normalised histogram of bead positions. For the calculation of reaction rates and transition barriers there are methods based on measuring correlation functions and the potential of mean force (PMF) on the centroid of the ring-polymer, which have been successfully applied [57, 64, 75, 122, 138, 139].

Chapter 3

Quantum tunnelling of OH at Cu(110)

Abstract

Recent low temperature scanning-tunnelling microscopy experiments [T. Kumagai *et al.* Phys. Rev. B. **79**, 035423 (2009)] observed the possible quantum tunnelling of hydroxyl groups between two equivalent adsorption configurations on Cu(110). Here we analyse the quantum nuclear tunnelling dynamics of hydroxyl on Cu(110) using density functional theory based techniques. We calculate classical, semi-classical and quantum mechanical transition rates for the flipping of OH between two degenerate energy minima. The classical transition rate is essentially zero at the temperatures used in experiment, and the tunnelling rate along the minimum energy path is also much too low compared to experimental observations. When tunnelling is taken into account along a direct path connecting the initial and final states with only a minimum amount of the oxygen movement the transition rate obtained is in much better agreement with experiment, suggesting quantum tunnelling effects cause a deviation of the reaction coordinate from the classical transition path.

3.1 Introduction

The quantum tunnelling of hydrogen plays a role in a wide variety of scientific disciplines, such as the functioning of enzymes in biological processes [66, 67], diffusion

through metals [140] and high pressure ice [63], to name but a few. Through well-defined experiments at surfaces it is now possible to shed light on quantum nuclear effects at the level of individual adsorbates. In particular with low-temperature STM it has been possible to measure tunnelling rates for a number of diffusion processes involving individual atoms and molecules. Notable examples are the measurement of the diffusion rate of H and D on a Cu surface [141] and the diffusion of water clusters, suggested to be assisted by hydrogen bond tunnelling, on a Pd surface [4, 7].

In an intriguing recent development Kumagai *et al.* [142] interpreted STM images of hydroxyl molecules on Cu(110) as direct evidence of quantum tunnelling of the hydrogen atom between two equivalent states. Individual adsorbed hydroxyl molecules were imaged as symmetric double protrusions which were suggested to correspond to a superposition of two equivalent tilted configurations either side of a symmetric transition state. Since the experiments were performed at only 6 K, and the barrier for the flipping process was calculated with DFT to be > 0.1 eV, it was concluded that the flipping between two degenerate energy minima must be the result of rapid quantum tunnelling. Estimates of the rate from Wentzel-Kramers-Brillouin (WKB) theory with the assumption that oxygen doesn't move during the transition, and the observation of a kinetic isotope effect when deuterized OH (OD) was used, provided further evidence that the low temperature transition is mediated by quantum tunnelling. These observations are interesting and suggest that OH on Cu(110) could be a well defined and relatively simple model system for the study of quantum nuclear effects. While the DFT and WKB modelling of Kumagai *et al.* was an important step in describing this system, there are still questions that remain unanswered. The most pressing of these is the role of oxygen in the tunnelling event, and the question of how the classical and quantum reaction paths may differ. In addition it is unclear how well WKB describes this particular tunnelling transition. Answering these questions will not only provide deeper understanding of the quantum tunnelling dynamics of adsorbed hydroxyl but will be instrumental towards developing a general understanding of the quantum effects of small molecules on surfaces.

In this work we present an account of our DFT based studies of the flipping of OH between two equivalent states on Cu(110). First we use the NEB [118] method to determine the activation energy and MEP for the transition. We find that the barrier for the flipping process is 166 meV (145 meV including zero-point energy effects) and that while the H flips there is a surprisingly large movement of the oxygen. Applying classical transition state theory to this barrier yields rates very much smaller than the experimentally measured rate and due to the combined oxygen and hydrogen movement, semi-classical estimates of the tunnelling rate along the MEP are also very low. Since semi-classical methods rely on a transition path being specified, we applied a wavefunction approach over the independent hydrogen and oxygen reaction coordinates to further understand the process. Overall we find that quantum tunnelling can be responsible for the transition at low temperatures as long as the oxygen motion during the transition is suppressed via corner-cutting of the MEP.

3.2 Method

The DFT calculations used the CASTEP [143] and VASP [144–147] codes. Vanderbilt ultra-soft pseudopotentials [112] were used in CASTEP and projector augmented wave potentials [113] in VASP. Wavefunctions were expanded in terms of a plane wave basis set with a cutoff energy of 350 eV (CASTEP) and 415 eV (VASP). The PBE [95] exchange-correlation functional was used throughout. The surface was represented as a p(3×3) periodic supercell, with the bottom two of the four layers fixed and 14 Å of vacuum in the z-direction, normal to the surface plane. Sampling of reciprocal space was done using a $4 \times 4 \times 1$ Monkhorst-Pack **k**-point mesh [111]. These choices of cutoff energy, slab thickness and **k**-points were made after an extensive set of convergence tests which focussed specifically on accurately describing the energy barrier for the OH flipping process. These established, for example that the barrier obtained with an eight layer setup and $8 \times 8 \times 1$ **k**-points was only 25 meV away from that obtained with the chosen computational setup. Likewise the barrier and adsorption structures obtained with the two DFT codes were very similar (Table 3.3). CASTEP [143] was used to calculate the potential energy

	a_0 (Å)	B_0 (mbar)	E_{coh} (eV)
$2 \times 2 \times 2$	3.688	1.15	2.838
$4 \times 4 \times 4$	3.654	1.26	3.420
$8 \times 8 \times 8$	3.636	1.33	3.480
$12 \times 12 \times 12$	3.638	1.32	3.480
Other DFT	3.635	1.36	3.484
Experiment	3.603	1.42	3.490
FP-LAPW	3.630	1.42	3.510

Table 3.1: Lattice constant (a_0), bulk modulus (B_0) and cohesive energy (E_{coh}) for bulk copper using different **k**-point meshes. Values from other DFT studies [149], from experiment [150] and all-electron full-potential linearized augmented plane-wave (LAPW) calculations [151] have been included for comparison.

Number of layers	E_{ads} (eV)
4	3.530
6	3.488
8	3.520

Table 3.2: OH/Cu(110) adsorption energy for various numbers of layers, calculated using $4 \times 4 \times 1$ **k**-points. The bottom two layers in each slab were kept fixed, the rest were allowed to fully relax.

surface (PES) for the transition, as VASP does not have non-linear constraints.

The choice of the above parameters were based on convergence tests, comparing the DFT calculated quantities with values known from experiment and all-electron calculations. A Murnaghan equation of state [148] was used to determine a suitable copper lattice constant, and **k**-points (Table 3.1). The number of layers was converged by considering the OH adsorption energy (table 3.2). To ensure the **k**-points were still effective for this surface, adsorption energy was recalculated for the four-layer slab using $8 \times 8 \times 8$ **k**-points. This yielded 3.534 eV, compared with 3.530 eV for $4 \times 4 \times 1$ **k**-points.

3.3 Results

Initially a single OH monomer was adsorbed on the Cu(110) surface. The molecule adsorbs with the oxygen near a short bridge site, and the O−H tilted by about 60° to the surface normal (Table 3.3, Fig 3.1). This adsorption geometry agrees with the theoretical geometries from Kumagai *et al.* [142]. By symmetry there are two equivalent adsorption structures, as shown in Fig. 3.1. NEB calculations revealed that these two equivalent adsorption sites are separated by a classical barrier (ΔE) of 166 meV, and the transition state (TS) for this process involves a perfectly upright OH (shown in Fig. 3.2, image 8).

	IS	TS
ΔE (meV)	-	166 (155)
O−H bond (Å)	0.98 (0.98)	0.97 (0.97)
O−Cu bond (Å)	1.96 (1.96)	1.95 (1.92)
θ ($^\circ$)	59.9 (62.8)	0.0 (0.0)
$\Delta_{\mathrm{O-Cu}}$ (Å)	0.02 (0.04)	0.00 (0.00)

Table 3.3: Some relevant DFT-PBE calculated properties for OH/Cu(110). ΔE is the classical activation barrier for the OH flip. θ is the angle of the OH to the surface normal. The $\Delta_{\mathrm{O-Cu}}$ lateral distance is the lateral displacement of the oxygen from the precise short bridge site. The values above are calculated using VASP. The values in brackets are from CASTEP.

Applying classical transition state theory, the rate for the flipping process as a function of temperature (T) is,

$$\text{Rate(T)} = Ae^{-\beta\Delta E}, \text{ where } A = \frac{\prod_{i=1}^{N} \nu_i^{\mathrm{IS}}}{\prod_{i=1}^{N-1} \nu_i^{\mathrm{TS}}}. \tag{3.1}$$

A is the "prefactor", $\beta = (k_B T)^{-1}$ and the ν^{IS}, ν^{TS} are the initial and transition state vibrational frequencies of the OH molecule on Cu(110). With the substrate fixed there are six modes at the IS and five at the TS, as the lowest frequency becomes imaginary and is consequently ignored. At the 6 K used in the experiments of Kumagai *et al.* [142] classical transition state theory predicts a negligible rate

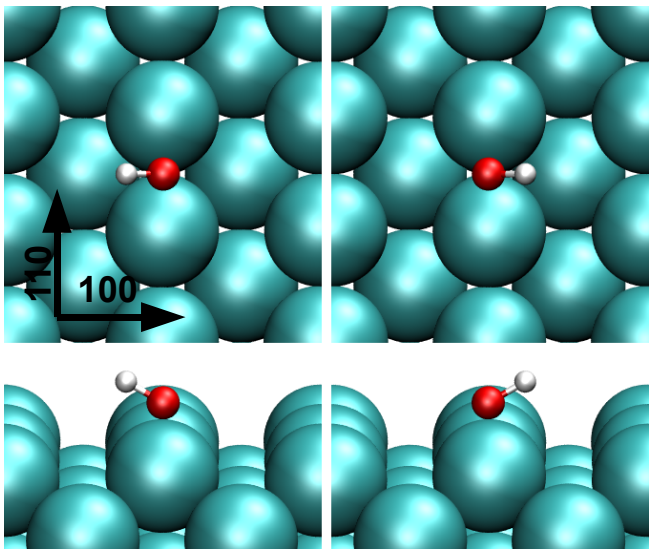

Figure 3.1: The adsorption geometry of OH on Cu(110) shown from above (top) and from the side (bottom). Two equivalent structures are possible due to symmetry. In our discussion we will refer to the image on the left as the initial state (IS) and the image on the right as the final state (FS).

(less than 10^{-100} s^{-1} for OH and OD). Therefore, as Kumagai *et al.* discussed, the double depressions achieved in one low temperature STM image suggest that the molecule tunnels between two equivalent structures. Employing a simple harmonic semiclassical approximation to the transition state suggests quantum effects should be relevant below about 80 K for OD or 100 K for OH [1]. This is much higher than the 6 K used in the experiments, and so quantum tunnelling effects need to be considered.

One of the simplest methods to approach tunnelling is the WKB approximation. This gives an estimate for the rate,

$$\text{Rate} = \nu e^{-\frac{2}{\hbar}\int_0^a dx\sqrt{2m(V(x)-E)}}, \tag{3.2}$$

where ν (in s^{-1}) is the initial state frequency along the reaction coordinate, a is the transition path length (chosen such that $[0, \text{a}]$ corresponds with with nonclassical region where $E < V(x)$), m is the mass of the tunnelling species, and $\hbar$ is

[1] Using the equation, $T_\text{c} = \hbar\nu^{\text{TS}}/(2\pi k_\text{B})$ where ν is the (imaginary) frequency at the transition state (4.3×10^{12} s^{-1} for OH, 4.1×10^{12} s^{-1} for OD), k_B is Boltzmann's constant and $\hbar = h(2\pi)^{-1}$. This is discussed in [J. Phys. C: Solid State Phys, 20 (1987)].

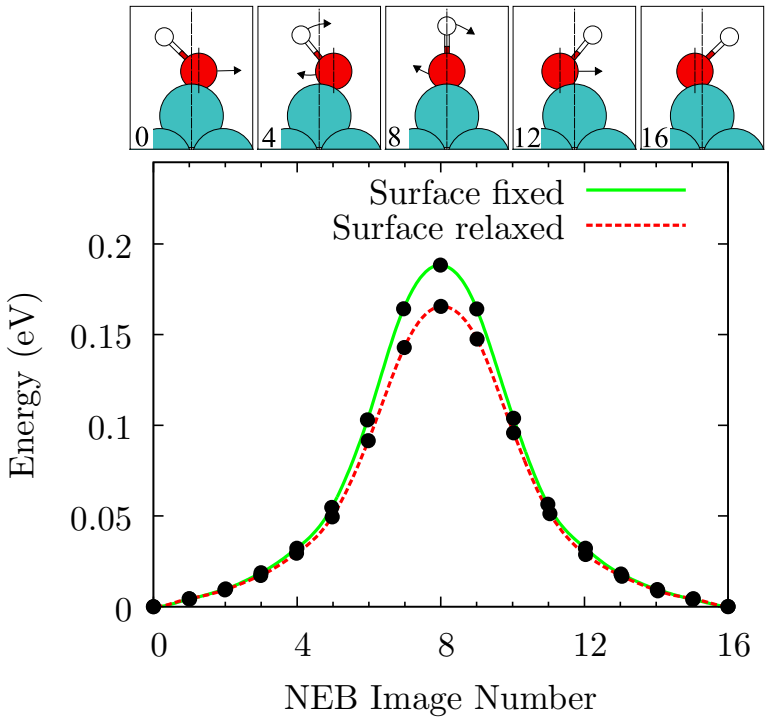

Figure 3.2: MEP obtained from a 15-image NEB calculation for the hydroxyl flip process on Cu(110). The red (dashed) and green (solid) curves correspond to the converged MEP with the top two layers of the surface relaxed or fixed in their bulk truncated configuration respectively. The relaxed and fixed models predict transition barriers of 166 and 187 meV respectively. The cartoons at the top of the graph are schematic illustrations of how the molecule moves during the flipping process, with the arrows indicating how the molecule moves from one step to the next. Although the difference in position between the O atom in the initial and final states is very small, along the MEP the oxygen undergoes a large displacement before passing through the transition state. It is this supplementary oxygen movement which greatly supresses the tunnelling rate along the MEP.

Planck's constant over 2π. $V(x)$ and E are the potential barrier and initial energy respectively. Here E is the zero-point energy (ZPE) contribution [2]. Within WKB a transition path must be *a priori* defined, however since for the process considered

[2]The zero-point energy contribution to the activation energy barrier is determined from the initial state and transition state frequencies. The ZPE of a state is $E^{\text{ZPE}} = \frac{\hbar}{2}\sum_i^N \nu_i$, where N is the number of vibrational modes (six at the initial state, five at the transition state). The effect of ZPE on the barrier is given by $E_{\text{TS}}^{\text{ZPE}} - E_{\text{IS}}^{\text{ZPE}}$.

here several different, yet still feasible, paths exist this is an immediate drawback. Nonetheless one obvious choice is to start by choosing the MEP. If we solve Eq. 3.2 for tunnelling of OD or OH along the MEP.[3] we obtain a rate of less than 10^{-6} s^{-1}. This is a much lower rate than the one determined in experiment.

Previous work has shown that a deviation from the MEP is sometimes preferred in transitions involving several different masses [152], and so to better understand the transition and possible alternative tunnelling paths we mapped out the PES for hydrogen and oxygen motion during the transition. This was done on the fixed Cu(110) surface since it reduces the transition to just two degrees of freedom (lateral oxygen movement, and displacement of the hydrogen), and the barrier is only changed by $\sim$20 meV. The calculated PES is shown in Fig. 3.3. If we use the classical transition path (Fig. 3.2, black line in 3.3) with the total mass of the OH molecule and the center of mass as the reaction coordinate, the transition rate is approximately 10^{-8} s^{-1} for OD (10^{-6} s^{-1} for OH) similar to that obtained on the relaxed surface and still a far lower rate than experimental observations suggest. Assuming the hydrogen moves in a circular path, and that the oxygen is completely stationary (as done originally by Kumagai *et al.*), the WKB rate is approximately 10^{4} s^{-1} for OD (10^{6} s^{-1} for OH). Therefore movement of the oxygen during the transition has a substantial quenching effect on the rate. Another possibility is that the oxygen neither remains completely stationary nor follows the MEP but instead takes a "direct" path from its IS to its FS position (the straight solid white line in Fig. 3.3). This results in a simple reaction coordinate which is orthogonal to the MEP with a total oxygen displacement of just 0.04 Å, compared to about 1 Å along the MEP. Using this path with WKB we evaluate a tunnelling rate of about 10^{5} s^{-1}.

So far we see that tunnelling is certainly possible at the temperature used in experiments. The calculation of the rates from WKB is complicated because it requires the prior selection of the reaction path, and as we have just seen this choice can have a huge impact on the obtained rate. Explicit calculation of the wavefunctions from the PES allows for an estimate of the transition rate without choosing a

[3]Using the full OH (or OD) mass along a reaction coordinate given by the movement of the center of mass of the molecule.

particular reaction coordinate.

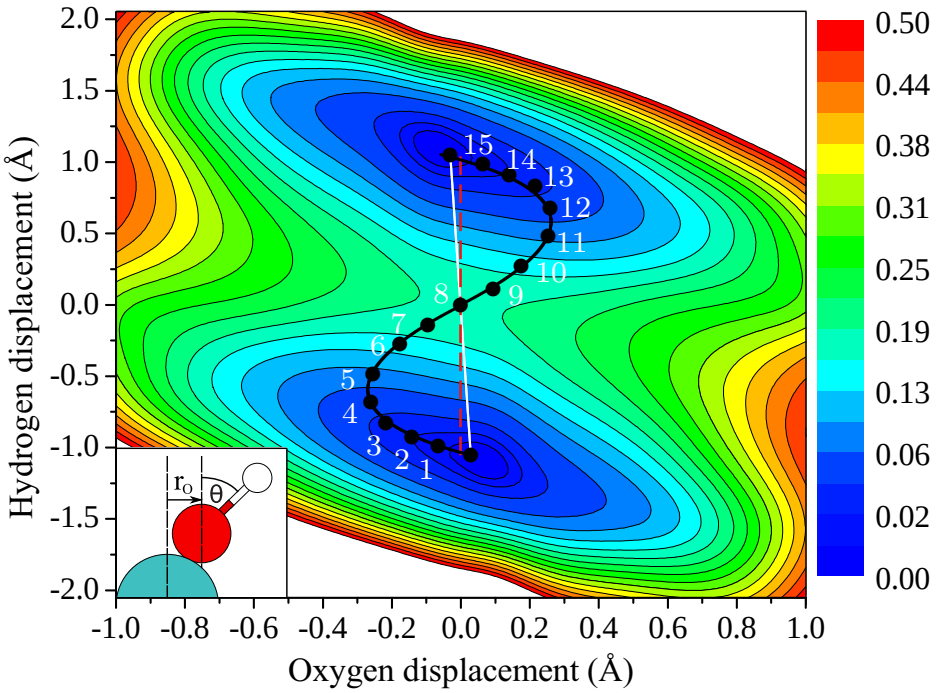

Figure 3.3: Potential energy surface in eV for the hydroxyl flip process on the bulk truncated Cu(110) surface as a function of oxygen and hydrogen displacement. This was generated by constraining the angle of the OH to surface normal (θ in the inset) and fixing the oxygen position at each displacement in the Cartesian x and y axes, both parallel to the surface. At each displacement ($r_O = \Delta_{O-Cu}$) the hydroxyl was free to relax both by moving in the z direction (normal to the surface plane) and by varying the OH bond length. A total of 90 DFT calculations were performed, and the results interpolated to a finer mesh by means of a cubic spline. The MEP is shown as a black curve, and each image (except for the initial and final states) is numbered. Bead number eight is the transition state. The white solid line is the "direct" path joining the initial and final configurations with minimal movement of the oxygen. The dashed red line with no oxygen movement represents the WKB tunnelling path used by Kumagai *et al.*

We can write the time-independent Schrödinger equation in terms of the hydrogen and oxygen movement,

$$\left[-\frac{\hbar^2}{2m_H}\frac{\partial^2}{\partial r_H^2} - \frac{\hbar^2}{2m_O}\frac{\partial^2}{\partial r_O^2} + V(r_H, r_O)\right]\psi(r_H, r_O) = E\psi(r_H, r_O), \tag{3.3}$$

where r_H, r_O are the hydrogen and oxygen degrees of freedom, and m_{H}, m_{O} are the masses of hydrogen (or deuterium) and oxygen respectively. $V(r_{\mathrm{H}}, r_{\mathrm{O}})$ is the potential energy surface (Fig. 3.3).[4] The nuclear wavefunction $\psi(r_H, r_O)$ was expanded in a plane-wave basis, up to a cutoff of 5 Ry. The Hamiltonian is solved using an iterative Lanczos algorithm [153, 154], in which the kinetic energy operator is applied in Fourier space, and the potential energy operator is applied in real space. The result is a sequence of energy levels and their corresponding wavefunctions (eigenvalues and eigenvectors of the discretised Hamiltonian). At a particular temperature the probability density (P) will be a superposition of all the calculated eigenstates weighted by the Boltzmann factor,

$$P = \sum_{i=1} |\psi_i|^2 \frac{e^{-\beta E_i}}{Z}, \quad Z = \sum_{i=1} e^{-\beta E_i} \tag{3.4}$$

where the index i runs over consecutive eigenstates, the $\{\psi_i\}$ and $\{E_i\}$ are eigenvectors and eigenvalues from the Lanczos procedure respectively. The results from the wave-like calculations of the density functions for OH and OD are shown in Fig. 3.4. The probability densities exhibit a double peaked structure with the two peaks centered on the two minima of the PES (Figs. 3.3 and 3.4). By appealing to a semi-classical transition state theory approximation, we can relate the probability of a tunnelling event to the ratio of probability densities at the initial (r_{IS}) and transition (r_{TS}) states,

$$\text{Rate} = \nu \frac{P(T, r_{TS})}{P(T, r_{IS})}. \tag{3.5}$$

The initial state frequency (ν) is essentially the number of transition attempts. Eq. 3.5 has the usual limitations of conventional transition state theory, in particular recrossing of the saddle point is not considered and we are assuming the initial harmonic frequency along the path directly connecting and IS and TS is valid. Using the calculated frequency along the PES reaction coordinate of $\nu = 2.98 \times 10^{12}$ s^{-1} for OD in the initial state ($\nu = 3.17 \times 10^{12}$ s^{-1} for OH) we calculate rates of $\sim 1 \times 10^5$ s^{-1} for OD and $\sim 1 \times 10^8$ s^{-1} for OH (Table 3.4). Thus the wavefunction calculations also clearly indicate that rapid flipping is possible. The rate predicted

[4] r_{H} is determined as the arc-length of the hydrogen from the surface normal position using $r_{\mathrm{H}} = r\pi\theta/180$, where r is the OH bond length.

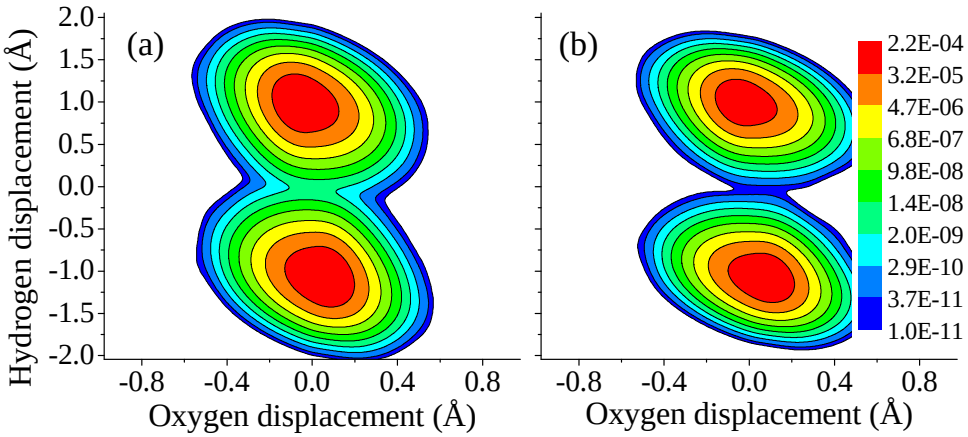

Figure 3.4: Probability densities of OH (a) and OD (b) position on Cu(110) at 6 K. Both graphs show a double peaked structure, with a small probability at the transition state (the transition state is where oxygen and hydrogen displacements are both zero). A logarithmic scale is used to emphasise the probability at the barrier region.

by this method is greater than that to come from experiment and WKB (when there is minimal or no displacement of oxygen). This overestimation may be a drawback of the reduced dimensionality of the wavefunction model.

The WKB calculations predicted a corner-cutting deviation from the MEP, and further evidence for this can be seen with wavefunction calculations with a fictitious mass. Varying the oxygen mass has relatively little effect on the transition probability compared with the change from OD to OH, suggesting that oxygen plays a small role in the transition. For example if the mass of oxygen is increased to 32 a.u. the transition probability is only reduced to 10^{-6} (compared with 10^{-5} for OH).

	OH	OD
Experiment	-	$0.9 \times 10^3 \pm 0.4 \times 10^3$
Classical TST	$< 10^{-100}$	$< 10^{-100}$
WKB MEP	7×10^{-8}	$< 10^{-10}$
WKB O-stationary	3×10^6	1×10^4
WKB direct	7×10^5	1.9×10^3
Wavefunction	1×10^8	1×10^5

Table 3.4: Rates (in s^{-1}) for the OH and OD flipping process on Cu(110) at 6 K. The classical TST rate is the one obtained from the Arrhenius equation (Eq. 3.1) using the classical energy barrier. The "WKB MEP" rate is calculated along the classical transition path. The "O-stationary" transition is represented by the dashed red line in Fig. 3.3. The "WKB direct" transition is the one shown by the solid white line in Fig. 3.3. The transition rate labelled "wavefunction" is the one obtained from Eq. 3.5. Rates include a contribution from ZPE.

3.4 Summary and Discussion

Having used DFT WKB and wavefunction modelling to examine the flipping of OH between two equivalent adsorption geometries, we can now further understand the STM result of Kumagai *et al.* Quantum tunnelling can make the flipping process possible at the low temperatures used, however for tunnelling to occur at an appreciable rate there must be a change in the reaction pathway of the classical transition. In particular the superfluous zig-zag movement of oxygen during the transition must be minimised. One way this can happen is for the oxygen to remain completely stationary. Another more likely scenario is a direct transition (solid white line in Fig. 3.3), since the path length is significantly shortened and the barrier height is identical to the classical transition. The fact that the path length can be considerably shortened but the transition still proceeds through the lowest energy transition state is a particularly unusual and noteworthy feature of this system. In general the dynamics of a classical transition for hydrogenated molecules such as OD (OH) will show considerable movement of the heavy species, due to the MEP following the lowest frequency mode. For these systems it may be expected that tunnelling yields a much higher transition rate along a path orthogonal to the MEP, which reduces movement of the heavy species and should couple the new reaction coordinate to a harder vibrational mode. This is similar to the large curvature tunnelling path methods discussed for heavy-light-heavy nuclei [152].

We have used various techniques to compute rates for the hydroxyl flipping process on Cu(110). All of these methods have drawbacks but they do indicate that tunnelling is possible under a change in the reaction coordinate from the MEP. Ideally a complete treatment of this system would include the full dimensionality and anharmonic effects, such as is possible using PIMD.

Chapter 4

Quantum hydrogen bonds at surfaces: the water dimer at Cu(110)

Abstract

The relatively light hydrogen mass can make QNEs such as tunnelling and zero point motion relevant, however these are often ignored in theoretical treatments. By considering small water clusters adsorbed at a metal substrate progress has been made recently in understanding the quantum nature of the proton, providing insight into quantum effects on larger water systems. Here we present a theoretical account of QNEs using semiclassical and path-integral molecular dynamics methods with density functional theory to examine the adsorption structure and dynamics of a water dimer at Cu(110). We find that the H-bond, O−Cu distances and H-bond angle are all increased by QNEs. On this particular surface a simple tunnelling mediated interchange of the hydrogen bond donor-acceptor of the type discussed in [T. Kumagai *et al.* Phys. Rev. Lett. **100**, 166101 (2008) and V. A. Ranea *et al.* Phys. Rev. Lett. **92**, 136104 (2004)] is not identified, although we do propose another transition involving rapid rotation of the H-bond donor water molecule.

4.1 Introduction

The importance of H-bonds in nature is clear: they are responsible for the double helix structure of DNA, and they play a vital role in the structure of water and ice.

H-bonding is therefore an active area of research, yet our understanding is still far from complete. The nature of H-bonds at low temperatures is directly affected by QNEs, due to the relatively light mass of the H atom. Continued improvement of computational methods, in particular *ab initio* PIMD [62, 73, 74, 155], and the availability of massively parallel computers has allowed valuable progress to be made in this field [55–63]. For example, by studying a selection of molecules and solids Li *et al.* [55] proposed that stronger H-bonds are made further stronger by QNEs, whereas relatively weak H-bonds become weaker. Another effect to come from a quantum nuclear description is the sharing of the proton involved in the H-bond. Bulk ice under ambient pressures has an O–O distance ~ 2.8 Å with well defined asymmetric H-bonds (where the proton is associated with one oxygen), however the reduction in O–O distance to ~ 2.3 Å under high pressure (≥ 70 GPa) combined with ZPE and tunnelling effects lead to a quantum mechanical delocalization of the proton [63]. A different way to change the H-bond length is to adsorb a water overlayer at a metal interface, so that the O$-$O distance is affected by the lattice constant of the substrate, i.e. surfaces with a smaller lattice constant squeeze the adsorbed water, reducing the H-bond length [156]. It has been suggested that on a compressed water overlayer QNEs will lead to a sharing of the proton, by simulations of water-hydroxyl overlayers adsorbed at Pt(111), Ru(0001) and Ni(111) [56]. An understanding of the behavior of water molecules at metal interfaces is an important field of study, with application in electrochemistry, heterogeneous catalysis and energy production [6].

Studies of small water clusters at metal interfaces provide insight into the nature and dynamics of H-bonded systems in general. In particular the water dimer is used as a simple model since it is the smallest hydrogen bonded water cluster, while the metal substrate permits application of a wide variety of surface science based structural probes. In this context STM experiments have been especially useful, for example by tracking the movement of individual water structures from the monomer up to the pentamer on Pd(111) an anomalously high diffusion rate of these clusters was established [157]. The diffusion rates at 40 K were found to be 2.3×10^{-3}, 50 and 1.0 Å^{2}s^{-1} for the monomer, dimer and trimer/tetramer respectively, while

the pentamer was found to be largely immobile. Ranea *et al.* [7] suggested that high mobility of the dimer could be explained by a quantum tunnelling mediated H-bond donor-acceptor interchange, coupled with the freedom of the acceptor water molecule to rotate around the donor. The water dimer H-bond exchange is thought to readily occur in the gas phase [158], however upon adsorption the exchange process is less understood. Subsequent low temperature STM experiments of a water dimer at Cu(110) by Kumagai *et al.* [4] sought to isolate the donor-acceptor interchange process. They observe blurring of the STM images, consistent with a transition taking place, and observe an isotope effect by performing the experiment with both $(H_2O)_2$ and $(D_2O)_2$, obtaining interchange rates of 60 ± 6 s^{-1} and 1.0 ± 0.1 s^{-1}. This is very strong evidence of a quantum tunnelling around the H-bond donor-acceptor, however the precise mechanism of the interchange process remains unclear. This system presents an important opportunity to improve on our general understanding of H-bonds at metal interfaces by considering QNEs, dispersion effects, and STM tip electric field effects.

In this work we extend upon recent advances in characterizing H-bonds for water at surfaces [6, 56]. Using the water dimer adsorbed on Cu(110) as a well defined model system, we give a detailed account of the effects of an electric field from an STM tip, dispersion, thermal or a quantum treatment of the nuclei. We also make connection with the experiments of Kumagai *et al.* [4] by comparing adsorption geometries with their reference STM images, and by considering the possibility of a H-bond interchange process due to tunnelling. After calculating the energies of many different adsorption configurations, we find three structures within 40 meV of each other (Fig. 4.1). One of these structures is identified as a TS between the other two, leading to the possibility of a rotational wagging of the dimer either side of the Cu(110) ridge. Due to the high barrier and oxygen movement involved we do not locate a mechanism for the rapid tunnelling mediated H-bond donor-acceptor exchange process. We do identify another process which involves the H-bond donor water rotating out of the surface plane, forcing the free hydrogen up and over to sit on the opposite side of the molecule. This flipping process is possible from any of the low energy adsorption geometries, and estimates from the

WKB approximation suggest a tunnelling rate of roughly 10^7 s^{-1}.

4.2 Methods

The DFT calculations used the VASP [144–147] code. PAW potentials [159] were used and wavefunctions of the valence electrons were expanded in terms of a plane wave basis set with a cutoff energy of 415 eV. The PBE [95] exchange-correlation functional was used throughout, although tests with the optB88-vdW non-local van der Waals functional are also discussed [50, 52]. For this the self-consistent implementation of vdW-DF added to VASP by Klimeš *et al.* [52] was used. The surface was represented as a p(2×4) periodic supercell, with the bottom two of the six layers fixed and 14 Å of vacuum in the z-direction, normal to the surface plane, and sampling of reciprocal space was done using a $4 \times 2 \times 1$ Monkhorst-Pack **k**-point mesh [111]. These choices of cutoff energy, slab thickness and **k**-points were made after an extensive set of convergence tests which focused specifically on accurately describing the relative energies of the three most stable geometries in Fig. 4.1. These established, for example, that the difference in adsorption energy obtained with an eight layer setup and $16 \times 8 \times 1$ **k**-points was only 5 meV away from that obtained with the chosen computational setup. We also checked the PAW potentials by calculating adsorption energies with "hard" versions of the PAW potentials, which have a smaller cutoff radius and in the case of copper include 17 valence electrons (the standard PAW potential contains 11 valence electrons). These give adsorption energies within 5 meV of the standard potentials used, and so for efficiency we used the standard PAW potentials.

MEPs were found using the CI-NEB method[119]. We used between four and sixteen images, depending on the transition path length, and converged the forces on each image to less than 0.01 eV/Å. The ZPE was calculated by computing the harmonic normal modes of the adsorbates with the finite displacements method and with the lattice fixed in the optimized configuration. The ZPE effects on energy barriers is seen as the ZPE energy difference between the initial state (IS) and TS structures. This is a semi-classical approximation for including some quantum ef-

k-points	Layers	(a) E_{ads} (eV)	(c) E_{ads} (eV)
4×2×1	6	0.707	0.665
8×4×1	6	0.707	0.665
12×6×1	6	0.709	0.666
16×8×1	6	0.710	0.667
4×2×1	8	0.712	0.671
8×4×1	8	0.708	0.668
12×6×1	8	0.709	0.670
16×8×1	8	0.708	0.670

Table 4.1: The adsorption energies E_{ads} of the water dimer, for various **k**-point meshes and thickness of the slab, in two of the low energy geometries (a) and (c) corresponding to Fig. 4.1.

fects of the nuclei. We also took a more rigorous approach to including quantum nuclear fluctuations by using the PIMD [62, 73, 74, 155] method implemented in VASP [59] at 50 K. We used 16 ring-polymer beads, which is sufficient to understand the trends due to QNEs [55, 56, 139]. These are compared to DFT-based MD simulations performed at the same temperature, with a Nosé-Hoover chain of thermostats [160, 161] and a time-step of 0.5 fs. The calculations were run for about 8100 (16000) PIMD (MD) steps. Simulated STM images come from the Tersoff-Hamann approach [162], considering states from 1.5 eV below the Fermi-level, up to the Fermi-level. A tip height of ~ 4 Å above the highest atom in each adsorption system was used.

4.3 A. Equilibrium dimer structures

The Cu(110) surface has a ridge and valley structure with close packed rows of Cu atom ridges along the 110 direction. To determine the initial geometry of the adsorption system a water dimer was placed at the surface of a Cu(110) slab in 11 different sites on the ridge and in the valley. These included the H-bond donor in the atop, short bridge and four-fold hollow site, with the dimer aligned along the

direction of the ridge, the short-bridge and angles in-between. After each structure is optimized all the lowest energy geometries are characterized by the fact they have the H-bond donor water molecule located at an atop site on the ridge, with the acceptor molecule positioned along the ridge or either side of it. The atop position is the most stable adsorption site for the water monomer [5], and the weaker coupling of the acceptor to the surface is consistent with the picture from previous DFT and STM studies on similar transition metal surfaces [2, 157, 163, 164]. The three most stable structures to come from this analysis are shown in Fig. 4.1. The bond lengths and adsorption energies for these structures[1], with corrections for ZPE, are shown in Table 4.2. The adsorbed water dimer has an O−O distance around 2.71–2.73 Å, which is significantly less than the gas phase DFT-PBE value of 2.95 Å. This shortening of the H-bond upon adsorption at metal surfaces has been seen before, and is understood to be due to the substrate increasing the polarisability of the water dimer [6]. The H-O-O bond angle (annotated in Fig. 4.2) varies between $7.8°$ and $2.7°$. The distance in height of the oxygen atoms is also important, since this dictates the minimum oxygen movement required for an interchange of the roles of H-bond donor and acceptor, as we see later.

Kumagai *et al.* interpreted their STM experiments as corresponding to structure (c), however here we find the lowest energy structure is Fig. 4.1(a) with an adsorption energy of about 710 meV, and the presence of an imaginary mode for (c) suggests it's a transition state joining structures (a) and (b). This has a classical barrier of about 40 meV and requires 1.4 Å of oxygen movement, which may occur as a rare event coupled with thermal vibrations of the copper ridge. It is possible the STM images observed by Kumagai *et al.* are a superposition of states (a), (b) and (c). Our value for the adsorption energy of geometry (c) is more stable by 90 meV compared with the value from Kumagai *et al.* [4] for the same basic structure. This relatively small difference in absolute adsorption energy is likely accounted for by

[1]Adsorption energy is calculated using the equation $E_{ads} = E_{(\mathrm{H_2O})_2} + E_{\mathrm{Cu}(110)} - E_{(\mathrm{H_2O})_2/\mathrm{Cu}(110)}$, where $E_{(\mathrm{H_2O})_2/\mathrm{Cu}(110)}$ is the total energy of the adsorbate/substrate system, $E_{(\mathrm{H_2O})_2}$ is the energy of a gas phase water dimer and $E_{\mathrm{Cu}(110)}$ is the energy of the clean substrate. The same sized cell was used for each calculation.

differences in computational setups (number of surface layers and supercell size). Since we are dealing with relatively small changes in energy we decided to carefully

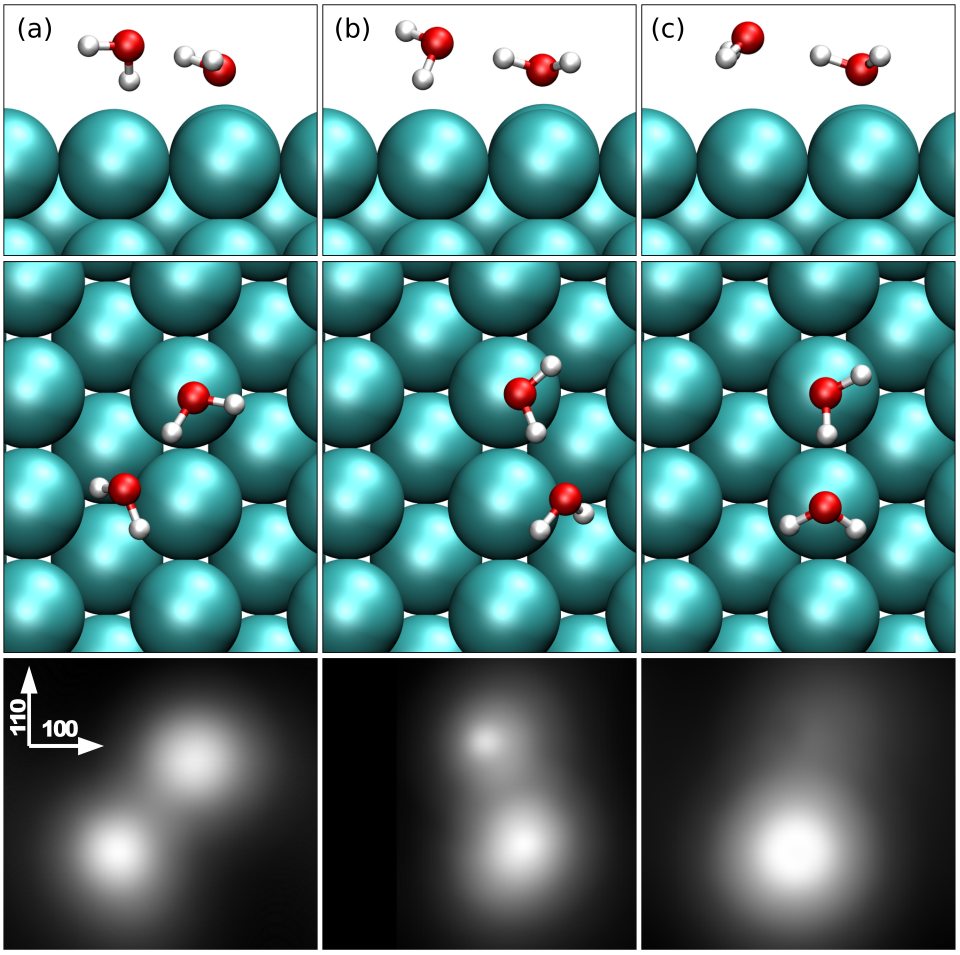

Figure 4.1: The three lowest energy configurations for 2 (H_2O)/Cu(110) as computed with DFT-PBE, shown from the side (top) and from above (middle). Structures (a) and (b) have the lowest energy, whereas structure (c) is a transition state. The simulated STM images for each of these structures is shown for comparison. Details of the adsorption structures and energies of these configurations are given in Table 4.2.

check if the structure of the dimer would be affected by electric field effects from the STM tip, van der Waals dispersion forces, thermal or quantum effects.

It is known that STM creates an electric field which can modify the orientation of molecules during the imaging process [165]. We used DFT to compute the influence of an applied electric field, normal to the surface, on the geometry of the

Property	(a)	(b)	(c)
E_{ads} (eV)	0.71	0.70	0.67
ZPE (eV)	0.03	0.04	0.02
H-bond length (Å)	1.72	1.71	1.73
$O_{donor}-$Cu distance (Å)	2.10	2.10	2.10
$\Delta_{O_{donor}-O_{acceptor}}$ (Å)	2.71	2.73	2.73
$\Delta^{x}_{O_{donor}-O_{acceptor}}$ (Å)	1.48	1.03	0.02
$\Delta^{z}_{O_{donor}-O_{acceptor}}$ (Å)	0.56	0.62	0.73
H-O-O bond angle (°)	7.8	2.7	3.6

Table 4.2: Some relevant DFT-PBE calculated properties for $(H_2O)_2$/Cu(110). E_{ads} is the adsorption energy of the water dimer relative to the a gas phase dimer. ZPE is the zero point energy correction of each structure computed from the vibrational modes of the adsorbed and gas phase dimer. $\Delta_{O_{donor}-O_{acceptor}}$ is the distance between the H-bond acceptor and donor oxygen atoms, while the $\Delta^{x}_{O_{donor}-O_{acceptor}}$ distance is the projection of this on to the 100 direction (a value of zero implies the dimer is aligned precisely along 110). $\Delta^{z}_{O_{donor}-O_{acceptor}}$ is the difference in heights of the oxygen atoms. For a definition of the H-O-O bond angle see the inset in Fig. 4.2.

water dimer at Cu(110). We computed the difference in total energy between the geometries shown in Fig. 4.1(a) and (c) for a range of applied electric fields (Table 4.3). There is very little change of the energetic ordering of the two geometries, and Fig. 4.1(a) remains the most stable structure. The electric fields we applied here are stronger than those in the STM studies by Kumagai *et al.* (~ 0.005 V/Å), so we conclude in this case that tip effects are unlikely to alter the initial geometry of the water dimer in this system.

The role van der Waals dispersion forces play in altering the adsorption structures and adsorption energies for molecules on surfaces is currently one of the hottest topics in theoretical condensed matter physics. Dispersion forces can often be very important (e.g. they have been shown to alter the relative energies of gas phase water clusters [166] and also alter the adsorption structure of organic molecules

Electric field (V/Å)	E_{diff} (eV)
-0.2400	-0.045
-0.0240	-0.041
-0.0024	-0.041
0.0000	-0.039
0.0024	-0.054
0.0240	-0.055
0.2400	-0.059

Table 4.3: The effect of an applied external electric field on the energy difference (E_{diff}) between structures in Fig. 4.1(a) and (c). $E_{diff} = E_{(a)} - E_{(c)}$, where $E_{(a)}$, $E_{(c)}$ refers to the energy of structure (a), (c) respectively.

on Cu(110) [167]). In order to investigate the influence of dispersion we examined the three adsorbed water dimer structures identified here with the optB88-vdW exchange-correlation functional [50, 109]. From these calculations we find that the structures obtained are relatively similar. Specifically the O−metal, O−O and O−H distances are the same as the PBE values to within 0.02 Å (see Table 4.2). Likewise the relative energies with optB88-vdW are very similar to PBE, and structure (a) remains the most stable with an adsorption energy of about 95 meV, which is ~ 200 meV larger than the PBE value. Thus we find that dispersion increases the adsorption energy but it does not alter the relative energies to any great extent, which is consistent with refs. [53, 168].

To determine what influence thermal effects have on the adsorption system MD calculations at 50 K have also been performed. By starting simulations in geometry (c), we consistently find that the system very quickly (i.e. within 1 ps) moves to one of the more stable geometries ((a) or (b)). The H-bond donor then remains pinned to the region atop one of the copper atoms, while the acceptor molecule moves a little more freely in the trough region between two 110 ridges. We measured some important properties of the system (O–O distance, O–Cu distance, H-bond length and the H-O-O angle) over the duration of our MD simulation (Fig. 4.2, red lines).

Most of these quantities are approximately the same as we obtained from our static structure calculations (Table 4.2).

To move beyond the approximation that the nuclei are classical point-like particles and to account for ZPE, non-harmonic effects and thermal effects simultaneously we applied the PIMD method. Starting from structure Fig. 4.1(c) as in the MD simulations we find the dimer rearranges to a structure similar to one of Fig. 4.1(a) or (b). By comparing the cumulative averages of the properties of the system in the MD and PIMD simulations after equilibration we can gain an insight into how QNEs alter the nature of the adsorption system. In Fig. 4.2 we see that the length of the $\mathrm{H}\cdots\mathrm{O}$, $\mathrm{O}-\mathrm{Cu}$ bond and the $\mathrm{O}-\mathrm{O}$ distance are all increased by approximately 0.04, 0.03 and 0.05 Å respectively due to QNEs. It is understood that the effect quantum mechanics has on a H-bond is directly related to the predicted strength of that H-bond (before QNEs are accounted for) [55]. One measure of H-bond strength, referred to as the H-bond strength index, is the ratio of the O-H stretching frequency in the dimer to the free monomer. This means that a higher strength index indicates a weaker H-bond [55]. Generally H-bonds with a strength index higher than about 0.7 are classed as weak. The free water dimer has a H-bond strength index of 0.95 [55], compared with the adsorbed water dimer H-bond strength index of 0.89. Also shown is a histogram of the MD properties and PIMD bead properties to show how the spread of each quantity is affected (Fig. 4.2, right) by QNEs. For most properties the size of the distributions are very similar, however there is a considerable increase in spread of the $\mathrm{H}-\mathrm{O}-\mathrm{O}$ bond angle, and larger bond angles become more likely (Fig. 4.2(d), right). The average of the bond angle is increased by about 6°. This is compatible with the findings by Li *et al.* [55], as the increase in H-bond bending due to QNEs indicates a weakening of the H-bond. A summary of how the structure of the adsorption system changes upon inclusion of dispersion or QNEs is shown in Table 4.4.

This sheds light on the H-bonded molecules adsorbed at a metal interface. We see from our PIMD simulations that the relatively weak H-bond present in a water dimer is made weaker by QNEs, consistent with previous studies for a gas water

Property	PBE	optB88-vdW	PBE MD (50 K)	PBE PIMD (50 K)
O−O (Å)	2.71	2.72	2.72	2.76
O−Cu (Å)	2.10	2.08	2.11	2.13
O−H (Å)	1.72	1.73	1.74	1.79
H−O−O (°)	7.8	7.4	8.2	13.2

Table 4.4: Comparison of some important structural properties using PBE, optB88-vdW, PBE with molecular dynamics and PBE based path-integral molecular dynamics for the water dimer at Cu(110).

dimer [55, 139].

4.4 B. Exchange process

It is thought the anomalously fast diffusion of smaller water clusters from the dimer up to the pentamer on metal surfaces is due to the fast interchange of the H-bond donor-acceptor [7, 157]. Kumagai *et al.* [4] used the present system to study this donor-acceptor exchange in-place (i.e. without diffusion of the molecule), since the copper ridges in the 110 direction prevent diffusion of the water dimer. We consider symmetric transitions starting from two initial configurations (a) and (c). Configuration (a) is the DFT predicted lowest energy structure for the adsorption system, however since this requires a significant amount of movement of the heavier oxygen atoms we also consider the transition state structure (c) as a starting geometry. For a starting configuration (a) the computed MEP is shown in Fig. 4.3, with snapshots from the transition path shown at the top of the figure. The barrier for this process is 128 meV and the transition involves a significant amount of lateral oxygen movement (more than 1.5 Å displacement of each oxygen atom). The coupling of the donor-acceptor exchange process with motion of the heavy oxygen atoms implies that tunnelling along this path should be extremely unlikely [2].

[2]For a barrier of approximately 0.1 eV and total oxygen displacement of 3 Å we estimate, from the WKB approximation, the lifetime between transitions to be longer than the age of the universe. We therefore do not see the transition presented here are a plausible mechanism on this surface.

If we instead use (c) as our IS for the donor-acceptor exchange transition we can obtain an energy barrier for the transition with the dimer aligned along the 110 ridge as was suggested by Kumagai *et al.* To obtain a narrower barrier we relax the oxygen atoms only perpendicular to the surface, effectively making use of corner-cutting of the MEP [3] which is seen in similar situations [152, 169]. Fig. 4.4 shows the resulting path with an energy barrier of 188 meV (60 meV higher than the MEP), which we will now use for the tunnelling reaction coordinate. The rate limiting step of the donor-acceptor exchange will likely be in bringing the two oxygens to the same height. This is due to the presence of a surface, and previous theoretical studies of this exchange process in the gas phase do not have such a restriction [158]. Movement of the oxygen atoms could happen either by thermal means (in particular the vertical vibrational component of the copper ion directly below the donating water molecule could reduce the displacement of the oxygen atoms), via quantum tunnelling, or a combination of both mechanisms. Considering the tunnelling probability from the WKB approximation for the H-bond donor-acceptor exchange but using only the oxygen movement with the energy profile in Fig. 4.4 gives an upper bound on the rate of about 1×10^{-11} s^{-1}. This suggests that if the donor-acceptor transition occurs at very low temperatures ($\sim$ 5 K) it is probably mediated by a combination of classical and quantum effects.

Another process that may be operable in adsorbed water clusters at low temperatures is simply the flipping of the "free" OH bond in the H-bond donor molecule. This would involve the H-bond donor water molecule flipping out of the surface-parallel plane, going up and over the oxygen atom and then coming down on the other side of the molecule (Fig. 4.5). This should be feasible with any of the computed geometries shown in Fig. 4.1 and it is possible that such a transition will produce a visible effect on STM imaging. Fig. 4.5 shows the path of this transition starting from geometry (c) (the transition starting from (a) or (b) is analogous). The energy profiles along their MEP for this "overtop" transition are shown

[3] If the oxygen atoms are allowed to completely relax in all directions there is a rotational "wagging" of the dimer about its center of mass, leading to an additional 0.4 Å of movement with a barrier of 158 meV.

in Fig. 4.6. The barrier is 65-70 meV, and the amount of oxygen movement is very small. Applying the WKB approximation [4] for the tunnelling rate of one hydrogen moving 2 Å through the potential barrier gives a rate of 10^7 s^{-1}. If $(H_2O)_2$/Cu(110) is replaced with $(D_2O)_2$/Cu(110) the rate is decreased to about 10^5 s^{-1}. These estimated rates should merely be treated as ball park figures but they do suggest that flipping of the free OH bonds for this, and other water clusters, is likely to be a very facile process at low temperatures.

4.5 Conclusions

We have considered the structure and dynamics of adsorbed water dimers on Cu(110) using DFT geometry optimisations, MD and PIMD. The purpose of this study was to obtain a deeper understanding of certain quantum aspects of a well defined H-bonded system, which has been the subject of a high resolution STM study [4]. We found two almost degenerate structures (Fig. 4.1(a) and (b)) connected by a third TS structure (c) 30 meV higher in energy. This is a different ordering from what appears to be observed in the STM experiments of the same system by Kumagai *et al.* The effects of dispersion and QNEs were included by using the vdW-DF and PIMD, however these do not change the energetic ordering of the structures. Taking cumulative averages of structural quantities measured throughout our MD and PIMD calculations we suggest that QNEs should cause a noticeable change in the structure of an adsorbed water cluster. In particular we observe a weakening of the H-bond consistent with the recent finding that QNEs should generally lead to a lengthening and weakening of already relatively weak H-bonds. Owing to oxygen movement and the relatively high barriers we were unable to find a simple mechanism for the H-bond donor-acceptor interchange in this case. If such a transition is possible on this surface then more advanced theoretical methods involving surface vibrations and quantum tunnelling along multiple reaction coordinates may be able to account for it [57, 75]. We did identify a transition involving the flipping of one hydrogen over the top of the dimer (Fig. 4.5), which should be possible from any

[4]The small amount of total oxygen movement (0.54 Å) is included in the WKB tunnelling approximation by considering the center of mass of the tunnelling species through the barrier.

of the low energy adsorption structures identified. Using the WKB approximation for the quantum tunnelling rate through a barrier of around 70 meV we believe this would be a regular event. We obtain a rate of 10^7 s^{-1} if the starting geometry is as shown in Fig. 4.1(c). Such an OH flipping transition is likely to occur in other systems [170, 171], and may have consequences for the aggregation of water molecules to form clusters at interfaces.

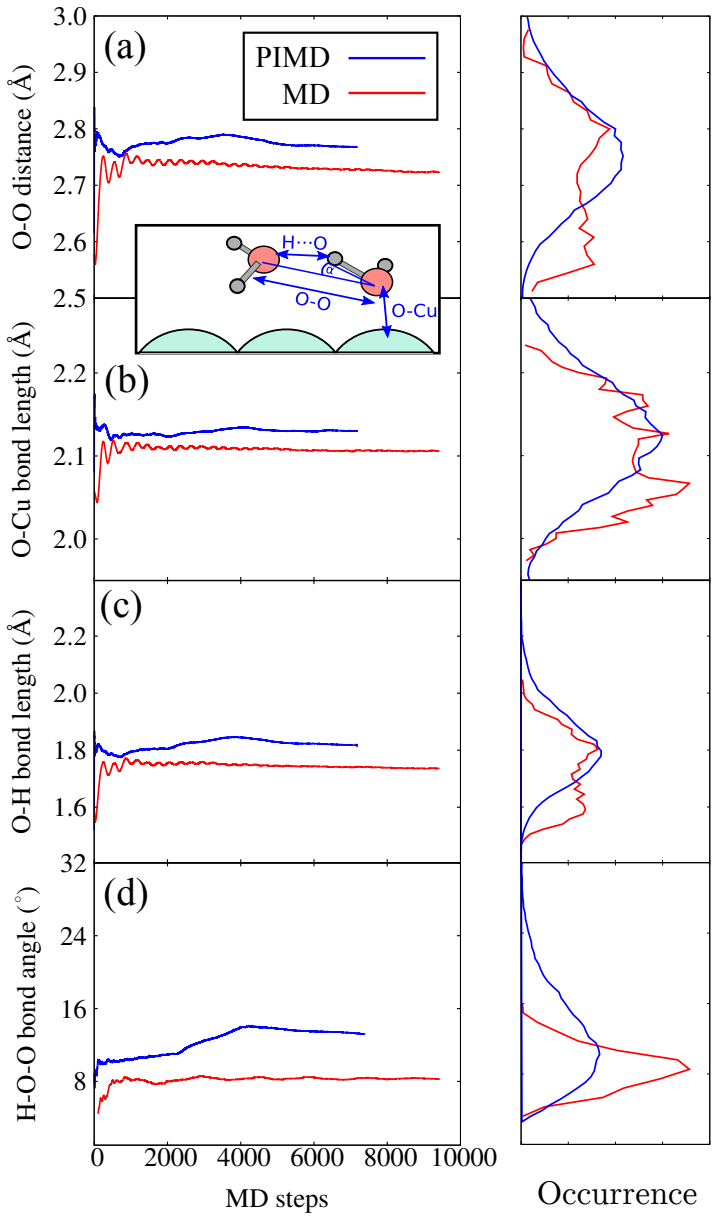

Figure 4.2: Structural properties of an adsorbed water dimer at Cu(110), taken from MD (labeled classical, red lines) and PIMD (labeled quantum, blue lines) calculations at 50 K. The solid lines on the left are cumulative averages. For the PIMD simulations the average is taken over all timesteps and all 16 beads. We plot a histogram of each quantity to give its relative occurrence (shown right). The first thousand MD or PIMD steps were discarded to allow for equilibration of the system. Here PIMD leads to a lengthening of the O$-$Cu, H$\cdots$O and O$-$O bonds about 0.03, 0.04 and 0.05 Å respectively. Figure (d) shows an increase in H$-$O$-$O bond angle (α) by about 6°. See the schematic between (a) and (b) for the meaning of each of these bond lengths.

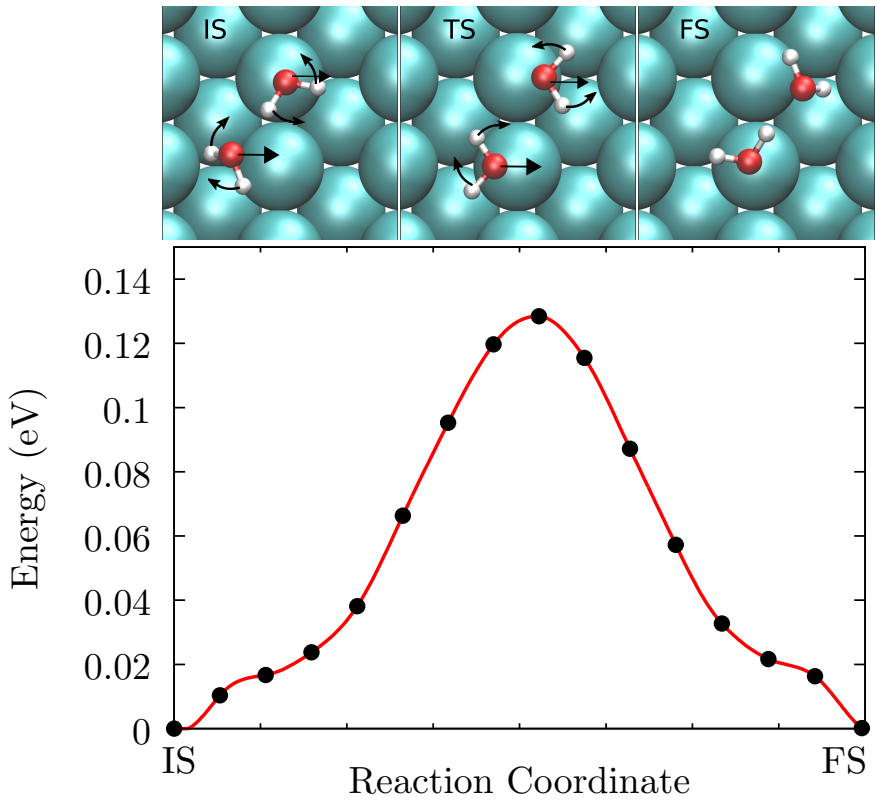

Figure 4.3: The energy profile along the MEP for the H-bond donor-acceptor exchange of 2 (H_2O)/Cu(110) from starting geometry (a). The barrier is 128 meV (110 meV if ZPE is included). The black dots are the NEB images used in the calculation and the smooth line a cubic spline interpolation of these using DFT forces. The initial state (IS), transition state (TS) and final state (FS) snapshots of the reaction coordinate are shown at the top. Here the reaction coordinate refers to the mass weighted path length along the MEP. The curved arrows show rotation of the water molecules, which is primarily movement of the hydrogen atoms. The straight arrows show the displacement of the overall water dimer laterally parallel to the surface plane. This highlights the amount of oxygen displacement, making such a transition due to tunnelling unlikely.

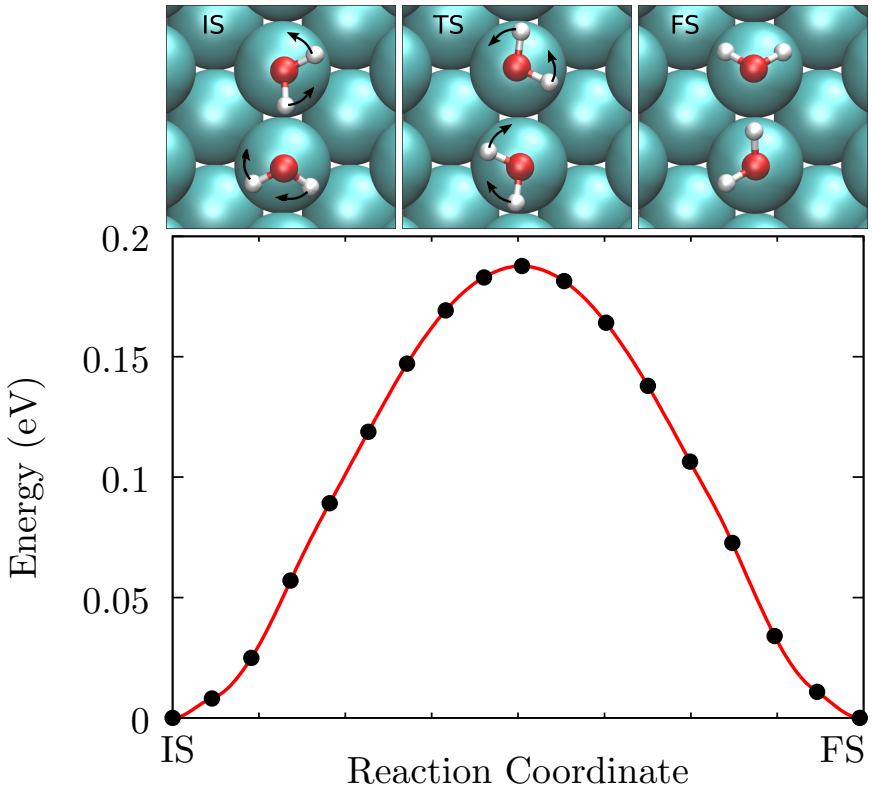

Figure 4.4: The energy profile along the MEP for the H-bond donor-acceptor exchange of 2 (H_2O)/Cu(110) from starting geometry (c). The oxygen atoms are fixed in the plane parallel to the surface and allowed to relax in the surface normal direction. The barrier is 188 meV (169 meV if ZPE is included). The black dots are the NEB images used in the calculation and the smooth line a cubic spline interpolation of these using DFT forces. Snapshots of the initial (IS), transition (TS) and final states (FS) are shown at the top. The curved arrows show rotation of the water molecules, which is primarily movement of the hydrogen atoms.

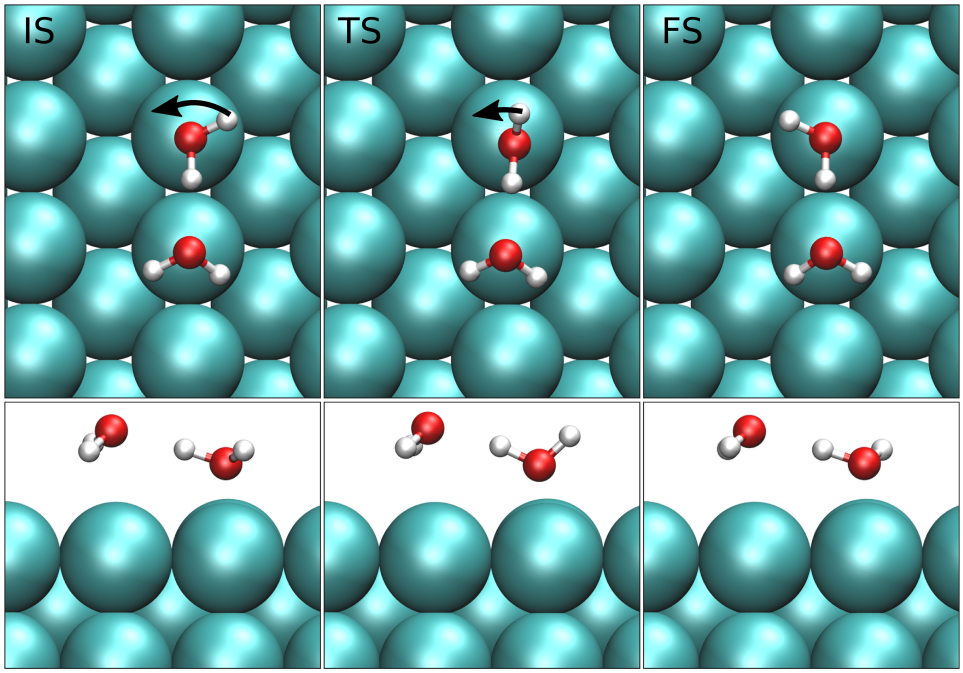

Figure 4.5: The initial (IS), transition (TS), and final (FS) structures for the donating water molecule's free hydrogen to flip up and over the oxygen. This process simply involves flipping of the free OH bond of the donor (i.e. this does not involve a H-bond exchange). Since we start from geometry (c) here the transition is completely symmetric and requires no oxygen displacement. The arrows highlight the path of the proton during the transition.

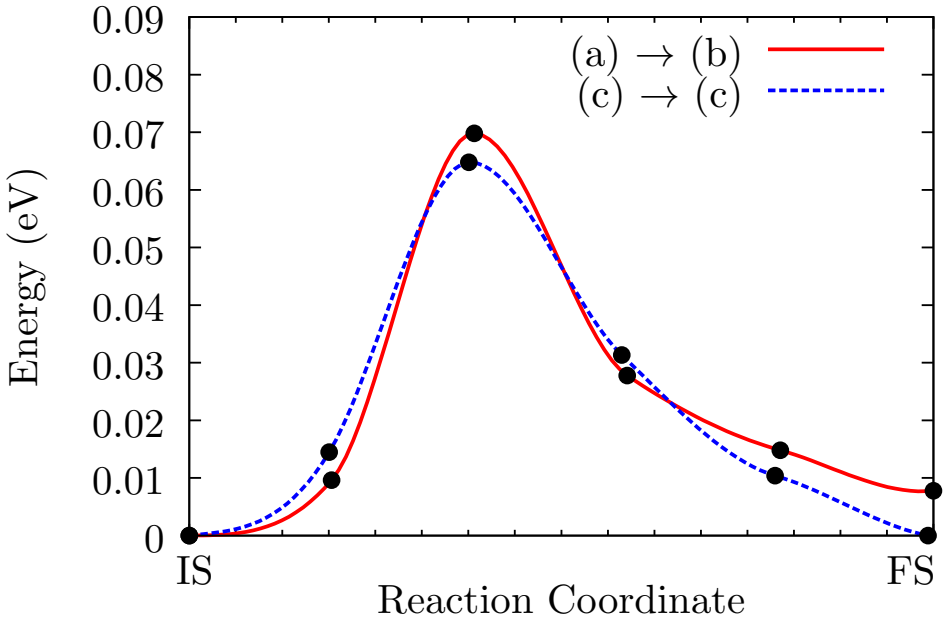

Figure 4.6: The energy profile along the MEP for the hydrogen flipping transition shown in Fig. 4.5. Two transitions are shown, corresponding to the geometry in Fig. 4.1(c) going to an equivalent structure (c), and the geometry in Fig. 4.1(a) going to structure (b). The energy barriers for the transitions are 65 and 70 meV respectively (69 and 65 meV including ZPE).

Chapter 5

Quantum mechanical and dispersion mediated adsorption of hydrogen on graphene and carbonaceous materials

Abstract

Carbonaceous grains are thought to catalyze the interstellar formation of H_2, however our theoretical understanding of this is surprisingly incomplete. This is mainly because state of the art computer simulation approaches predict a prohibitively high barrier for H chemisorption at grain surfaces. Here we use two model systems, H at graphene and at a polycyclic aromatic hydrocarbon, to show that with a proper account of both quantum nuclear effects and van der Waals dispersion the adsorption rate of H increases by many orders of magnitude. This lends support to the view that carbon-based materials can act as effective catalysts for low temperature H_2 formation in space, suggests that the low temperature hydrogenation of graphene is easier than previously thought, and emphasizes the general role of dispersion and quantum tunnelling on barriers for chemical processes at surfaces.

5.1 Introduction

The adsorption of atomic H on the surfaces of carbonaceous materials is of the utmost importance to a wide range of scientific disciplines. For example, carbon based materials such as graphite, carbon nanotubes and graphene have shown potential as materials for hydrogen storage.[172–174] H atom adsorption on graphene, which ultimately leads to graphane formation, offers the opportunity to control and tailor the band gap of graphene, raising the exciting possibility of engineering tunable semiconductors [175, 176]. In addition, H at graphene, graphite and polycyclic aromatic hydrocarbons (PAHs) are used as model systems to understand H_2 formation in the interstellar medium [9–25].

Considering the last area in more detail, important issues remain unresolved with regard to the mechanism of H_2 formation in the interstellar medium. While various mechanisms for H_2 formation have been proposed [177, 178], the most commonly and widely accepted mechanism involves H_2 formation catalyzed by carbonaceous dust grains [179]. At the lowest temperatures (< 30 K) there is experimental evidence that this can happen efficiently through the surface catalyzed recombination of H atoms that are physisorbed on the surface, i.e. atoms that interact with the surface through relatively long range van der Waals dispersion forces. However, in the slightly higher temperature regions of space ($\sim$ 30–100 K) physisorbed states evaporate quickly and so the H_2 formation reaction must involve chemisorbed H atoms, that is atoms that are adsorbed through a covalent C$-$H bond [180, 181]. Since chemisorption involves rehybridization and distortion of existing C$-$C bonds it is expected that there should be a barrier to chemisorption, but how this barrier can be overcome to enable H atom chemisorption on carbonaceous materials at the temperatures relevant to the interstellar medium remains a matter of debate [9, 10, 14–22, 182, 183].

From molecular beam studies Arèou *et al.* [184] were able to confirm the existence of a chemisorption barrier of between 25 and 250 meV on graphite at room temperature, as well as evidence that incoming H atoms can form H_2 upon meeting chemisorbed H atoms. The most widely used theoretical approach to study such

systems has been DFT, and so far such determinations of the adsorption barrier on graphene have been at the upper end of the experimental range at 200–250 meV (for a summary of computed physisorption energies and chemisorption barriers see Table 5.1). This barrier is high enough that the thermal H atom chemisorption rate at low temperatures is negligible. However, to date DFT studies on graphene have used GGA functionals that omit dispersion forces. Indeed a recent dispersion corrected DFT study (using the empirical DFT-D3 approach [106]) on the PAHs coronene predicted a reduction in the chemisorption barrier from 250 to 190 meV upon inclusion of van der Waals dispersion [9]. This leads to question marks over the role of van der Waals forces in this process on carbonaceous grains in general. Indeed understanding the role of van der Waals for adsorption processes in general is currently one of the more intriguing and active areas of research in computational materials science.

Another aspect to this process which remains largely untested by both experiment and theory is the role of quantum nuclear effects, such as tunnelling and ZPE. Given the low temperatures and light mass of H these effects can be expected to be large. The only work in this area to date comes from Goumans *et al.* [23, 24] who included quantum tunnelling effects for the chemisorption of H at the edge sites of benzene and pyrene (which have a smaller chemisorption barrier compared to the core sites [185]) and found an enhancement of the chemisorption rate at temperatures below $\sim$ 200 K. However, smaller PAHs are expected to be destroyed by photodissociation in the high UV regions of the interstellar medium, and so the hydrogenation of core sites within larger PAHs and graphitic surfaces is important for achieving a high rate of H_2 formation [186, 187].

It is clear that van der Waals and quantum nuclear effects are likely to be of importance to H_2 formation on carbonaceous surfaces and so here we address this head on with a combination of state of the art computer simulation approaches. Accurately describing dispersion interactions within DFT is a very active area of research, and several new methods to achieve this have already emerged, (see for example refs. [50, 106, 109, 188]). Here we use a modified version of the van der

Waals density functional (vdW-DF), and to account for quantum nuclear effects we use *ab initio* PIMD. PIMD is established as one of the most powerful schemes for considering ZPE, quantum tunnelling and delocalization of nuclei [55, 64, 189]. We find that upon including dispersion the physisorbed state is captured, which is missing from standard DFT, and the chemisorption barrier becomes lower and narrower. On graphene (coronene) the barrier is reduced from about 200 (230) to about 100 (140) meV. The classical free energy barrier for H at graphene – calculated from MD at 50 K – is similar to the underlying potential. However when we perform PIMD simulations at 50 K there is a dramatic reduction of the free energy barrier to just about 20 meV on graphene (50 meV on coronene). This is important as it increases the chance of a gas phase, or physisorbed, H atom chemisorbing at graphene and PAHs at low temperatures through quantum tunnelling and classical thermal mechanisms, hence subsequently enabling the formation of H_2. This work shows that the combined inclusion of both dispersion and quantum nuclear effects can greatly change the barriers for adsorption at surfaces and as such is vital for fully understanding the hydrogenation of graphene, hydrogen formation in space, and surface processes in general.

5.2 Methods

The DFT calculations presented here used the VASP [144–147] code. This includes a recent self-consistent implementation of the non-local vdW-DF method [52], and modifications for PIMD [59] which uses forces computed on-the-fly from the electronic structure calculations. Here we report results using PBE [95] and a modified version of the vdW-DF called optPBE-vdW, which uses exchange from an optimized PBE (optPBE) functional developed to yield more accurate interaction energies than the original choice of revPBE [50]. Two other vdW-DF based functionals, optB88-vdW and the original revPBE-vdW, lead to similar results (see appendix B). Benchmark studies on the performance of optPBE-vdW, including the application to adsorption, can be found in refs. [50, 52–54]. PAW potentials [159] and a plane-wave basis set were used with periodic supercells and a cutoff energy of 600 eV. For graphene we used a 3×3 unit cell with a $5 \times 5 \times 1$ **k**-point mesh,

System	Ref.	E_{phys} (eV)	Barrier (eV)	Method
H/graphene	[11]	0	0.2	Plane-wave DFT-PBE
H/graphene	[14]	0	0.22	Gaussian plane-wave DFT-PBE
H/graphite (4 layer)	[183]	0	0.2	Plane-wave DFT-PBE
H/graphite (4 layer)	[190]	0	0.2	Plane-wave DFT-PBE
H/coronene	[191]	0	0.2	Slater orbitals
H/graphene	[192]	-	0.25	Plane-wave DFT-PW91
H/pyrene (core site)	[24]	-	0.43	DFT-MPWB1K
H/pyrene (edge site)	[24]	-	0.125	DFT-MPWB1K
H/coronene	[9]	0.048	0.19	DFT-D3
H/graphene	[15]	0.005	-	DMC
H/benzene	[13]	0.04	-	MP2
H/coronene	[193]	0.1	0.1	LSD+PW91-GGA
H/coronene	[17]	0.038	-	DFT+vdW

Table 5.1: Summary of some of the physisorption energies (E_{phys}) and chemisorption barriers in the literature. The barriers for H atom chemisorption at graphene lie in the range $0.2 - 0.25$ eV. The physisorption energies are typically less than 0.05 eV.

and tests were performed on larger cells (see appendix B). Coronene was computed in a 15 Å cubic cell with a single (Γ) **k**-point. Since methods based on semi-local GGA exchange are known to underestimate reaction barriers, due to self-interaction errors, we used the Heyd, Scuseria and Ernzerhof (HSE) screened Coulomb hybrid exchange-correlation functional [102] to test the height of the barrier for the H at coronene system. HSE gives a chemisorption barrier of approximately 250 meV, only 20 meV higher than the PBE value, suggesting that self-interaction errors are not likely to be significant.

Total energy curves and MEP calculations used the CI-NEB method [119]. Finite temperature effects were accounted for by MD at 50 K. The free energy profile along the reaction coordinate for the H atom to go from gas phase to chemisorption was obtained using the PMF method. In this method the H is constrained at several

heights above the surface and for each height the component of force normal to the surface is averaged over a sufficient number of MD steps to obtain a converged average value. These average forces are then integrated to give the free energy barrier. Quantum nuclear effects are accounted for by the same PMF method with the height constraint placed on the centroid of the PIMD ring-polymer [62, 74, 122]. Our PIMD simulations used 16 imaginary time-slices (beads) with the Langevin thermostat, which is a reasonable compromise between accuracy and computational tractability (see appendix C). We also made use of the HQTST method (also called instanton) [125] on analytical potentials which have been fitted to the underlying DFT potential energy surface. These calculations used a total of 200 beads (see appendix D).

5.3 Results and Discussion

5.3.1 Hydrogen at graphene

We are mainly concerned with low densities of H at carbonaceous dust grains in the interstellar medium, so to begin we consider the adsorption of a single H atom in both the chemisorbed and physisorbed states. We discuss adsorption at the top site (directly above one carbon atom), since this is where chemisorption occurs, and the physisorption energies at the hollow, bridge and top sites are the same to within a few meV. The total energy profile using the standard PBE functional is shown in Fig. 5.1(a). PBE gives a chemisorption well of 800 meV with a H$-$C bond length of 1.13 Å and puckering of the top site carbon atom by ~ 0.4 Å. The barrier between the gas phase and the chemisorbed state is about 200 meV, consistent with many previous DFT studies [11, 14, 183, 190–192]. With PBE there is no physisorption state, which is again consistent with previous work and understandable given the lack of a long-range correlation term in GGA exchange-correlation functionals.

Using optPBE-vdW increases the chemisorption energy to about 950 meV. We also see a physisorption state at about 2.7 Å above the surface with a binding energy of approximately 100 meV. The barrier to go from the physisorbed to the chemisorbed state (in this case relative to the bottom of the physisorption well) is

reduced to about 90 meV. Due to the physisorbed state the barrier for a H atom to chemisorb is narrower and lower, two features which should increase the probability of a H atom chemisorbing on graphene by either thermal or quantum mechanical tunnelling mechanisms. The presence of a physisorbed state is consistent with experiment and other calculations with dispersion included, although the precise depth of the physisorption well is not well established [15, 194].

Previous theoretical studies of the chemisorption of H at graphene have generally been static calculations of total energy at absolute zero. An estimate based on the shape of the potential energy surface near the transition state [1] suggests a classical-quantum cross over temperature (the temperature below which classical and quantum regimes diverge [122]) of around 250 K. Therefore quantum nuclear effects are highly likely to be important at the temperatures relevant to H_2 formation in the interstellar medium (10 – 100 K). Here we report results at 50 K and we find that at this temperature the free energy profile (Fig. 5.1(b), solid pink line) is very similar to the underlying total energy profile (Fig. 5.1(a), solid green line). The physisorbed H state is virtually unchanged and the barrier to go from physisorption to chemisorption is smaller by about 20 meV (reduced from about 90 to about 70 meV). In contrast, when quantum effects are accounted for with PIMD we see a very pronounced difference. In particular the quantum free energy barrier obtained from PIMD is only about 20 meV. This barrier – which includes van der Waals, ZPE effects, quantum tunnelling and finite temperature effects – is approximately ten times smaller than barriers predicted for H atom chemisorption at graphene using traditional DFT-GGA methods [11, 14, 183, 190–192]. Although the barrier is substantially reduced the physisorption well remains relatively unperturbed, being shifted towards the gas phase by just ~ 0.3 Å.

It is interesting to consider the separate roles of ZPE and quantum tunnelling on the free energy barrier. Previous studies on other systems have found that the ZPE can be the dominant quantum nuclear effect [62, 139, 195–197]. Here we

[1] The quantum-classical crossover temperature as introduced by Gillan [Gillan, M. J. *J. Phys. C* **1987**, *20*, 3621] is given by $T_c = \hbar\omega_b/2\pi k_B$, where ω_b is the imaginary mode at the top of the transition barrier (approximately 3×10^{13} s^{-1}).

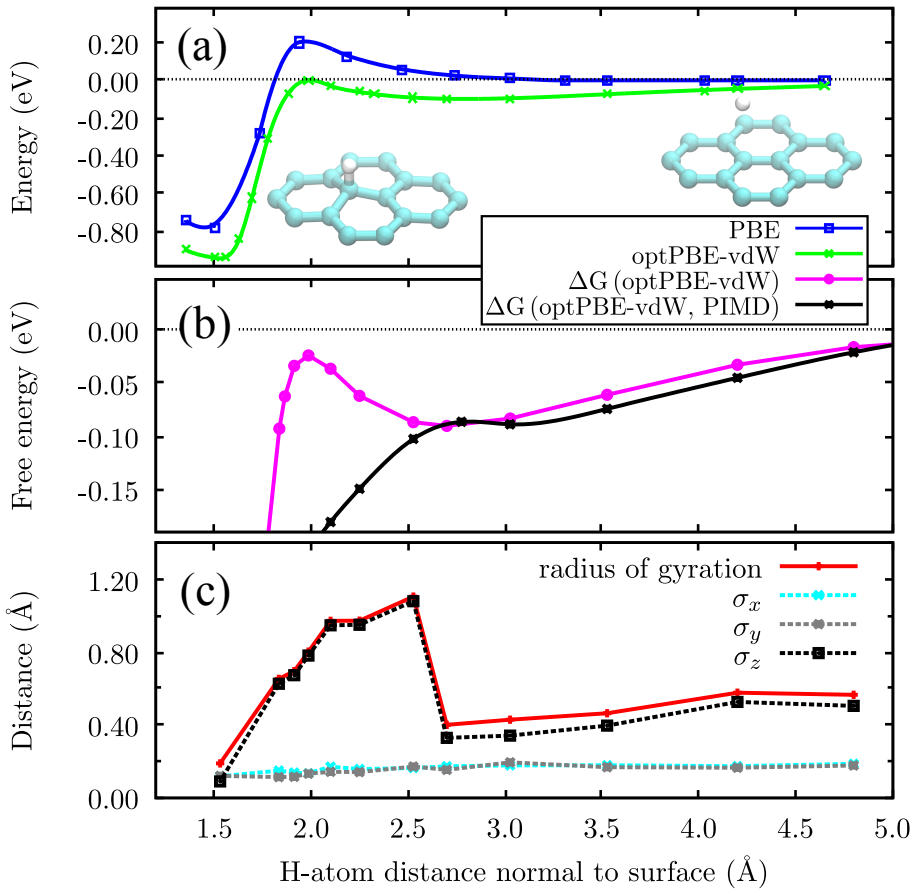

Figure 5.1: Total energy profiles calculated with the PBE and optPBE-vdW exchange-correlation functionals (a), and free energy profiles calculated with optPBE-vdW (b) for a single H atom at graphene. The H atom height above the surface is measured from the surface plane of the graphene sheet prior to chemisorption. The energies presented are relative to the completely desorbed H atom and a clean graphene sheet. The free energy profiles (ΔG, in (b)) are computed using both *ab initio* MD and *ab initio* PIMD approaches at 50 K. The statistical uncertainties on each point along the free energy profiles are typically less than about 7 meV. While the free energy profile with classical nuclei (pink line, circles) is a close match to the underlying optPBE-vdW potential energy curve (a), the inclusion of quantum nuclear effects (black line, crosses) very significantly lowers the free energy barrier to chemisorption to about 20 meV. The radius of gyration for the path-integral ring-polymer is shown in (c). This is decomposed into lateral (x,y) and normal (z) components relative to the surface plane.

estimate the ZPE effects on the barrier by taking the difference between the sum of the real-valued vibrational frequencies at the transition state and in the physisorbed state. The ZPE in each state is computed using vibrational modes from the finite displacement method on the fully relaxed classical structure. This analysis reveals that ZPE effects actually increase the barrier by about 40 meV. A small increase in the barrier is to be expected since the lateral motion of the H atom becomes more constrained as it approaches the surface, and is consistent with previous calculations for H adsorption on pyrene [24].

As ZPE cannot account for the reduced free energy barrier obtained from PIMD, it is constructive to consider how the H atom tunnels in more detail. To this end we start by examining the spread of the path-integral ring polymer at different heights above the surface. We do this first by aggregating all the bead positions along our MD trajectory for different heights of the centroid above the surface as shown in Fig. 5.2. This shows that for a centroid height of 3.5 Å there is a rather broad spread of bead positions, with the beads slightly more spread out in the direction of the surface normal than in the lateral directions (Fig. 5.2(a)). However, close to the transition state at a height of 2 Å there is a large spread of the beads in the z direction. This is shown in Fig. 5.2(b), where at this height it can also be seen that some of the beads already appear to be interacting chemically with the graphene. Some lateral squeezing of the beads at the classical saddle point can also be seen. In the fully chemisorbed state (Fig. 5.2(c)) the beads are pulled together producing a much narrower distribution due to the strength of the C$-$H chemical bond.

A more quantitative measure of the delocalisation is obtained by computing the radius of gyration (R_{gyr}) of the ring-polymer at each point on the quantum free energy profile (Fig. 5.1(c)) using the equation,

$$(R_{gyr})^2 = \sum_{i=1}^{N} (\sigma_x^2 + \sigma_y^2 + \sigma_z^2), \tag{5.1}$$

where N is the number of PIMD beads and σ_x, σ_y, σ_z are the standard deviations of the H atom beads in the x, y and z directions. Here we choose z to lie perpendicular to the surface, x and y lie parallel to the surface plane. This gives us a quantitative measure of the spread of the ring-polymer, and allows us to see the quantum char-

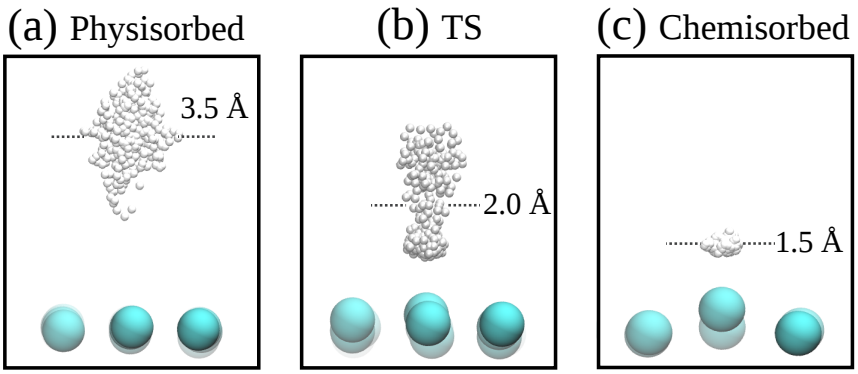

Figure 5.2: Snapshots from PIMD calculations at 50 K for the ring-polymer centroid constrained close to the physisorption well at 3.5 Å (a), at the transition state (TS) at 2 Å (b), and unconstrained in the chemisorbed state at 1.5 Å above the graphene sheet (c). The snapshots are an aggregation of bead positions for several hundred PIMD steps. In (a) the beads are only slightly more spread out in the direction of the surface normal than in the lateral directions. In (b) there is much more broadening of the beads normal to the surface. Some of the beads are chemisorbed while others are in the physisorbed state and there is slight lateral squeezing of the beads at the height of the classical transition state. In (c) the beads are squeezed together in the chemisorbed state due to the strong bonding with the surface.

acter of the H atom as it approaches the barrier. At a distance of ~ 4 Å from the surface the beads are quite spread out (R_{gyr} is about 0.5 Å), more so in the perpendicular direction (σ_z) because the underlying classical potential is pulling the beads towards the physisorption well. There is a very slight reduction of σ_z at 2.7 Å because the beads are squeezed together by the physisorption well. Upon approaching the chemisorption barrier (~ 2.5 Å) there is a dramatic increase in σ_z to 1.2 Å, due to spreading of the ring-polymer through the energy barrier towards the chemisorbed state. This is a clear indication that the H is able to tunnel through the energy barrier towards the chemisorbed state. As the centroid is brought closer to the surface (< 2 Å) the beads are compressed by the chemisorption well. From both Fig. 5.1(c) and Fig. 5.2 it is clear the H atom is much "more quantum" in the physisorbed and transition state than in the chemisorbed state. This is to be expected given the shape of the underlying potential and so is not necessarily a surprising result. It is however

a very clear demonstration of how differences in quantum effects can occur for such relatively small geometric changes. In this case by simply moving the H atom ~ 1 Å closer to the surface from the physisorbed to the chemisorbed states the spread of the path-integral beads is reduced and the wavefunction of the H atom is localized.

5.3.2 Effects of quantum tunnelling and dispersion on the rates of chemisorption and H_2 formation

We now briefly consider how the reduction in chemisorption barrier affects the rate of H chemisorption on the surface. Of course, there are many methods to compute transition rates (for example refs. [118, 198–200]), however here we are primarily interested in a qualitative understanding of the effects of dispersion and tunnelling and so rely on a basic transition state theory approach [2]. From this we find that the chemisorption rate across the 50 K free energy barrier is $\sim 1000\text{s}^{-1}$, which increases to 10^9s^{-1} when quantum nuclear effects are introduced via PIMD (Table 5.2). This large increase in the rate for H chemisorption at graphene is comparable with the increase in rate observed in related studies on the edge sites of PAHs [23, 24].

As discussed in the introduction, one of the motivations for this work was to understand the formation of H_2 at carbonaceous surfaces and molecules. It is understood that there needs to be chemisorption of H atoms for this to be efficient at temperatures above 30 K [180, 181]. Having established that the rate of H chemisorption is in fact much greater than previously calculated, we now examine the H_2 formation process. To this end we explore the reaction of a chemisorbed H with a physisorbed H. Previous computational studies – in which dispersion was not accounted for – have found that the closely related process of a gas phase H atom recombining with

[2] For the potential energy barriers ΔE we use the expression $R^{\text{phys-chem}} = A\exp(-\Delta E/k_BT)$ where the prefactor A ($\sim 10^{13}$ s^{-1}) is computed by taking a ratio of the product of frequencies at the initial (physisorbed) state with the product of frequencies at the transition state, within the harmonic approximation. No rate is reported for PBE since there is no physisorption state for the H atom and so no initial state frequency along the reaction coordinate. For the free energy barriers we compute the rate from $R^{\text{phys-chem}} = \kappa_a \exp(-\Delta F/k_BT)$, where the attempt frequency κ_a ($\sim 10^{12}$ s^{-1}) is the vibrational mode of the physisorbed H acting along the reaction coordinate.

	PBE	optPBE-vdW	optPBE-vdW (MD, 50 K)	optPBE-vdW (PIMD, 50 K)
E_{phys} (meV)	0	95	90	89
Barrier (meV)	203 [244]	87 [127]	66	16
κ (50 K)	10^{-21}	10^{-10}	10^{-9}	10^{-3}
$R^{\text{phys-chem}}$ (s^{-1})	-	~ 100	~ 1000	$\sim 10^{9}$

Table 5.2: Summary of some of the key properties for the physisorption and chemisorption of H at graphene. E_{phys} is the energy of the physisorption well relative to a gas phase (desorbed) H atom. The barrier is reported relative to the physisorbed state or in the case of PBE, where there is no physisorbed state, to the gas phase (desorbed) H atom. Values in square brackets are corrected for ZPE. The transition probability κ is computed from the Boltzmann factor at 50 K. $R^{\text{phys-chem}}$ is the rate constant to go from the physisorbed to the chemisorbed state, computed from transition state theory at 50 K [2]. The final column in which van der Waals and quantum effects are all taken in to consideration is the most accurate data reported in this article.

a chemisorbed H atom is barrierless [182, 190]. Here we find that the recombination between the chemisorbed and physisorbed H atoms is also barrierless. This means that the chemisorption of H atoms is the rate-limiting step in the formation of H_2 at graphene, emphasizing the importance of an accurate understanding of the chemisorption process on graphene.

5.3.3 Hydrogen at polycyclic aromatic hydrocarbons (PAHs)

The chemisorption of H at PAHs is a very popular and closely related model system for studying the formation of H_2 at dust grains [9, 10, 13, 15, 17, 23, 24, 185, 193, 201]. It is already known that quantum tunnelling facilitates chemisorption at the outer edge sites of small PAHs [24], however an understanding of chemisorption at the core sites is vital in generalizing this to larger PAHs and carbonaceous materials. Here we compute the barrier for a H atom to chemisorb at one of the core C atoms

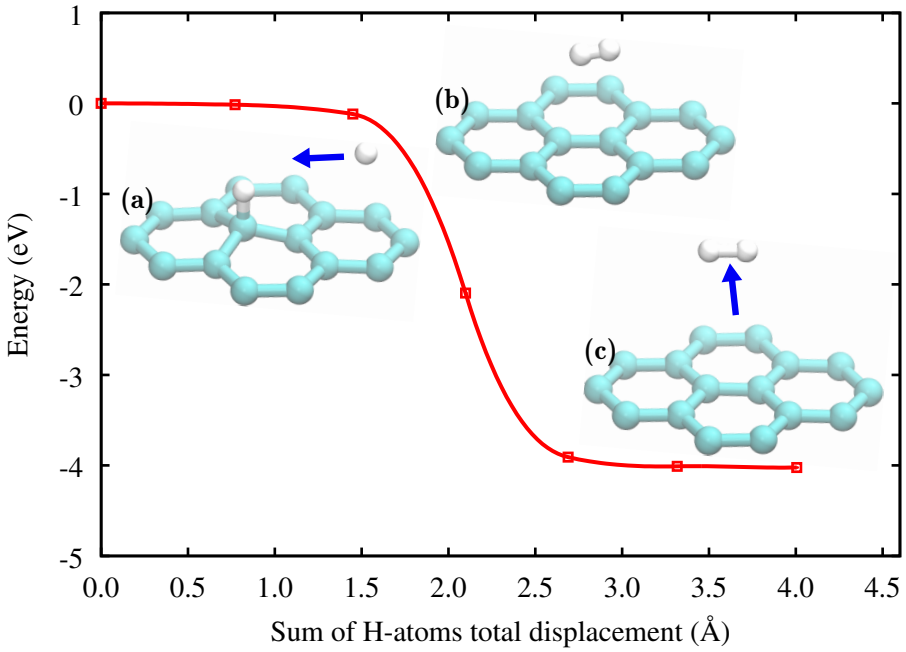

Figure 5.3: Total energy profile for the recombinative desorption of two H atoms from a chemisorbed and physisorbed state, computed with the optPBE-vdW functional. The line is computed by taking a cubic spline using the forces computed from DFT. Snapshots of the initial state, intermediate state and final states are shown pictorially as (a), (b) and (c) respectively. The final point on the profile corresponds to a H_2 height of about 3.9 Å above the graphene sheet.

of coronene again using the PBE and optPBE-vdW exchange-correlation functionals. Overall the results obtained are consistent with those on graphene. With PBE there is a chemisorption barrier of about 230 meV, a chemisorption state of about 670 meV, and no physisorption state. Using optPBE-vdW there is a physisorption well of 88 meV at 2.85 Å from the lateral plane of the coronene molecule. The chemisorption energy is increased to 730 meV and the chemisorption barrier is reduced to 140 meV, relative to the physisorption state. Thus again we find that accounting for dispersion forces introduces a physisorption minimum and reduces the chemisorption barrier.

To include quantum nuclear effects on this system we use the HQTST (instanton) method on an analytical one-dimensional potential (Fig. 5.4, solid green line) fitted to the underlying potential from optPBE-vdW. This is an alternative and

more economical Feynman path-integral based method which computes quantum tunnelling by the spread of beads over the barrier. The spread of the beads into the wells either side of the potential barrier to lower their energy is in competition with the mass and temperature dependent springs connecting the beads in a ring-polymer. Before using instanton theory on coronene we verified that on graphene very similar results were obtained to those from PIMD. This is shown in Fig. 5.4(a), where an instanton quantum energy barrier of ~ 20 meV is obtained, comparable to the quantum free energy barrier obtained from PIMD. The results from the instanton calculation on H at coronene (Fig. 5.4(b)) reveal a picture similar to the one that emerged on graphene: the quantum free energy barrier is about 50 meV relative to the physisorption well, substantially lower than the 140 meV potential energy barrier (including dispersion). This is slightly higher than for chemisorption at graphene because the barrier at coronene is slightly wider and higher. Thus on a model PAHs, as well as graphene, quantum effects and dispersion dramatically increase the probability of covalent C$-$H bond formation at low temperatures.

5.4 Conclusions

We have applied various state of the art simulation methods to better understand the formation of H_2 at graphene and coronene. The most striking result to come from this study is that quantum nuclear effects and dispersion work together to dramatically increase the likelihood of H atoms chemisorbing on graphene and at the core sites of PAHs. This shows that the role of quantum nuclear effects in the hydrogenation of carbonaceous surfaces is much greater than previously thought, and not just restricted to the edge sites of small PAHs where the barrier is lower [23, 24, 185]. This result is particularly relevant to low temperature H_2 formation since we have also shown how a gas phase (or physisorbed) H atom can react with the chemisorbed H in a barrierless recombination process to produce H_2. STM and DFT studies by Hornekær *et al.* [11] and Rougeau *et al.* [191] determined that once a single H atom has chemisorbed the barrier for subsequent H atoms to chemisorb locally is much smaller. Considered in concert with our findings this therefore facilitates the low temperature hydrogenation of large regions of graphene.

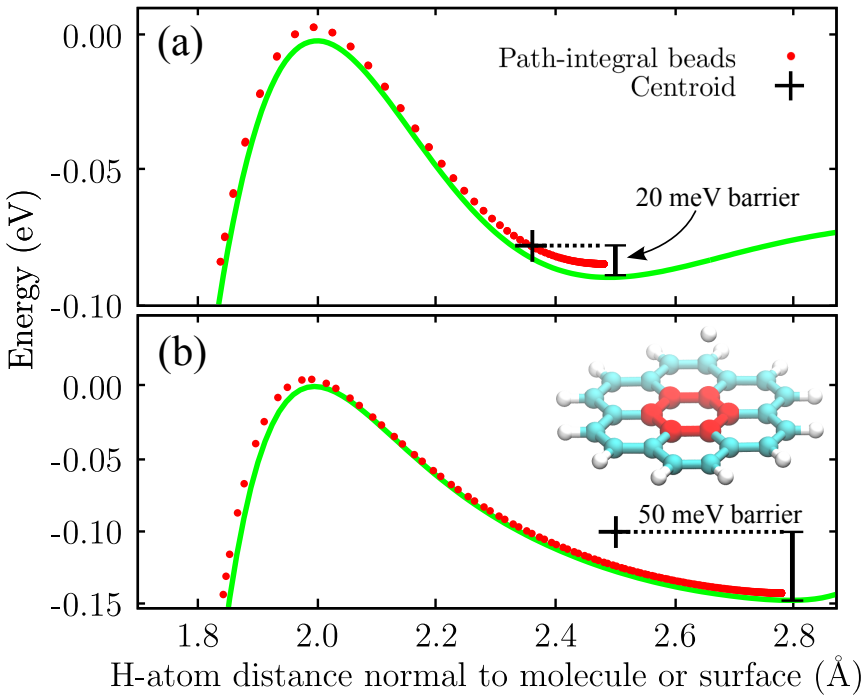

Figure 5.4: Plots of the heights and energies of the path-integral beads from instanton (HQTST) calculations at 50 K for H at graphene (top) and coronene (bottom). The solid green lines show the fit to the underlying optPBE-vdW potential energy curve. The instanton path-integral beads are shown as red dots. The average of these beads (the centroid, shown as a black cross) gives the HQTST free energy barrier. The structure of the H/coronene adsorption system is shown in the lower panel. The carbon atoms drawn in red are the core atoms, where we consider chemisorption in this work.

A proper account of quantum nuclear effects yields a significantly lower free energy barrier to H chemisorption and our analysis reveals that this is due to quantum tunnelling since ZPE effects actually slightly increase the chemisorption barrier. The use of PIMD in particular has enabled us to examine in detail the quantum nature of the H atom as it approaches the surface, revealing that the quantum behaviour of a H atom changes dramatically at different heights above the surface. This is most clearly seen in Fig. 5.2 where we see that upon approaching the surface the H goes from being quantum mechanically spread out in the physisorbed state to being highly localized in the chemisorbed state, via the classical saddle point where the H atom spreads out by about 1 Å normal to the surface. Clearly the location of a

particle at a surface has a direct effect on the amount of quantum mechanical spread, hence the importance of a quantum mechanical description of the system.

In this study we have improved upon the standard GGA (PBE) description of H atom adsorption by making use of the recently developed optPBE-vdW functional. The reduction in the barrier when including dispersion forces predicted here is also consistent with a recent DFT-D3 study on coronene where a decrease of the chemisorption barrier from 250 meV to 190 meV was found [9]. These small differences between the approaches used here and DFT-D3 only serve to highlight that the calculation of accurate adsorption energies for atoms and molecules on surfaces is currently a major challenge for modern electronic structure methods [156]. The vdW-DF based exchange-correlation functional used here predicts a physisorbed state and for several selected systems examined predicts adsorption energies in better agreement with the reference values than PBE [50, 53, 202]. It is, of course, unclear what the "exact" potential energy barrier is and how close optPBE-vdW comes to it. Indeed it would be very interesting to explore the chemisorption process with more sophisticated theoretical methods than used here, such as e.g. diffusion quantum Monte Carlo, but this is beyond the scope of the current study (see appendix E). Aside from theory, there is also much scope for improving our experimental understanding of this system. Previous molecular beam studies have been performed (at room temperature and at 150 K) which places the barrier in the 25–250 meV range [184, 203]. Building on this work with a detailed study employing a range of incident energies (e.g. 20–300 meV) at range of temperatures for both H and D would be instrumental in determining the chemisorption barrier as well as the presence of a quantum isotope effect.

We have focused on the recombination of H_2 at graphitic surfaces, however the findings here are also relevant to graphane production. Our results suggest that the chemisorption of a first H at carbonaceous materials is easier than previous theoretical studies have anticipated. At higher temperatures than considered here the free energy barrier to chemisorption will increase as the H atom behaves more like a classical particle. We expect this will be useful for those developing kinetic models of

H_2 formation at carbonaceous surfaces, which can include preferential chemisorption, evaporation of the physisorbed states, and surface temperature. Finally this work outlines the general necessity to use a combined quantum mechanical and dispersion treatment for surface processes involving H, which has only become possible in recent years due to improved methods for dispersion in DFT and the resources for large PIMD simulations.

Chapter 6

Can tunnelling cause proton transfer in ice Ih?

Abstract

Recent quasielastic neutron scattering experiments [L. E. Bove *et al.* Phys. Rev. Lett., **103**, 4 (2009)] provided some evidence of a concerted proton transfer event around an ice hexamer within ice Ih. The experiments were done at temperatures between 5 K and 260 K and estimated a transfer rate of about 2.7×10^{11} s^{-1}. Using calculations based on the density-functional theory coupled with the nudged elastic band method we attempt to provide insight into the dynamics of a possible quantum mechanical tunnelling event in this system. Searches for a path for proton tunnelling around an ice hexamer all reveal barriers much too high to give any agreement with the high rate from experiment. On the other hand we find that trapped Bjerrum defects could potentially anneal out of ice at low temperatures mediated by quantum mechanical tunnelling. We calculate a rate for this process of approximately 10^6 s^{-1}.

6.1 Introduction

Water ice is a commonly studied system due to its abundance on Earth, and its importance to terrestrial and planetary chemistry. In perfect ice Ih each water molecule is H-bonded to neighbouring water molecules in a distorted tetrahedral structure. This arrangement of water molecules in ice gives rise to a hexagonal symmetry, cor-

rugated up-down to form a bilayer structure. There are six distinct orientations of a water molecule in such a H-bonded network, which leads to ice Ih being proton disordered [204]. The protons sit in a symmetric double-well potential between the two oxygens, with a hop distance of about 0.75 Å between the well minima.

It was discussed in the previous chapters how the low H mass means it is capable of overcoming certain energy barriers by tunnelling through them. Of particular interest here is the symmetrization of H-bonds in ice, which has been proposed for both water overlayers on the 111 facet of some transition metals [56], and also in high pressure ice [65]. This is discussed in section 4.1, but the important point is that upon reducing the O$-$O distance in ice Ih quantum effects can lead to a sharing of the proton along the H-bond. While this is important, it only shows the possibility of proton transfer and sharing in ice under special conditions, such as much higher pressures than normally encountered.

The recent experimental work by Bove *et al.* [77] was interpreted as providing evidence of a concerted proton transfer event in ice Ih (and Ic) at temperatures between 5 K and 260 K (5 K and 160 K for Ic). They estimate that roughly 4% of the protons in the ice sample are involved in the transition, which corresponds approximately to the number of *ordered loops* (where hydrogens occupy the equivalent site around the hexagonal loop, i.e. $1/32$ – see Fig. 6.1). A proton jump distance of 0.75 Å was suggested from a fit of the Q-value dependence of the quasielastic incoherent structure factor (QISF) to the model double-well potential for a powder sample, and the rate of 2.7×10^{11} s^{-1} was extracted from the half width at half maximum of the quasielastic contribution to the intensity. The effect was assumed to be related to proton disorder, since the transition occurs in ice Ih and Ic, but not with ice VIII.

The prospect of a quantum mechanically mediated concerted proton transfer commonly occurring in a material as ubiquitous as ice Ih is very interesting, however it is not clear how such an event can be possible, particularly at the high experimental rate reported. Here we look for plausible transitions compatible with the hypothesis made by Bove *et al.* of proton tunnelling around an ice hexamer. Due

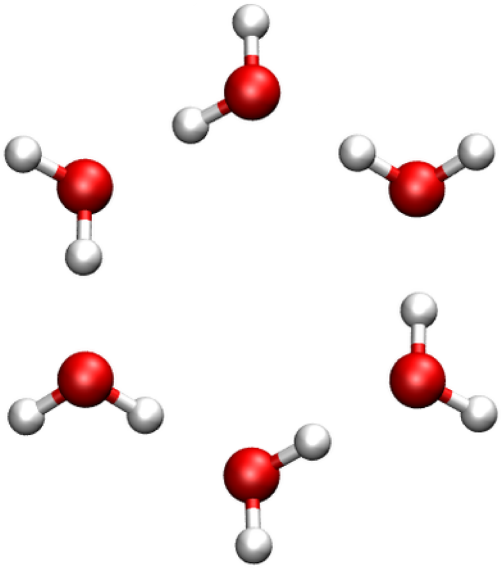

Figure 6.1: Example of one ordered loop ice hexamer. Note how all the hydrogen atoms around the ring occupy the same site, enabling a concerted proton transfer of six hydrogen atoms. The chance of any ice hexamer being ordered is $1/32$.

to the very high rate they report, the most interesting transitions will have a very low barrier and very little oxygen movement. Considering both direct translation of the protons and rotations of the water molecules, the concerted and non-concerted tunnelling of six protons around a hexamer are found to be very unlikely due to the high barriers involved. This places doubt on the experimental findings, and more experiments are needed to determine is such proton transfer events are really possible. We therefore present the tunnelling assisted annealing of Bjerrum defects as an alternative possible transition since the DFT predicted barriers are smaller, and oxygen movement is minimal. The barrier for a single Bjerrum defect to anneal is approximately 120 meV, which gives a rate from WKB of around 10^6 s^{-1}. We suggest that tunnelling could be a mechanism for the annealing of isolated Bjerrum defects in ice, and that this may be the effect observed in the experiments by Bove *et al.*

6.2 Methods

The DFT calculations used the VASP [144–147] code. PAW potentials [159] were used and wavefunctions were expanded in terms of a plane wave basis set with a cutoff energy of 415 eV. The PBE [95] exchange-correlation functional was used throughout. The ice was represented by 48 water molecules (18 ice hexamers). The lattice constants a and c of our simulation cell are set to agree with experiment [205], $c/a = 1.628$. Sampling of reciprocal space was done using a $1 \times 1 \times 2$ Monkhorst-Pack **k**-point mesh [111]. These choices of cutoff energy, and **k**-points were made after an extensive set of convergence tests which focused specifically on minimising the error in the lattice energy per water molecule. These tests established that the lattice energy per water molecule obtained with $4 \times 4 \times 8$ **k**-points and a cutoff energy of 1000 eV was only 3 meV away from the chosen computational setup (see Table 6.1). The lattice energy of 0.669 eV obtained here is within 30 meV of the value determined by Feibelman [206, 207] using the PBE exchange-correlation with the VASP code, the difference we account to the choice of lattice parameters for our ice structure.

We ran benchmark calculations on an isolated ice hexamer using the second order Møller-Plesset perturbation theory (MP2) method [208] as implemented in the Gaussian 03 code [209]. Calculations used the aug-cc-pVTZ basis set, which is large enough to give accurate relative energies between different hexamer configurations [166].

6.3 Results

In this work we start by considering a direct transition, involving proton transfer from one oxygen to the next around a single ice hexamer within the ice structure. This requires the breaking of covalent bonds. Then we consider various concerted rotations of the water molecules which only involve the breaking of H-bonds.

First we consider the most intuitively simple concerted proton transfer possible in ice Ih: the direct hopping of a hydrogen along the H-bond per each water molecule within a single hexagon of ice. A concerted proton transfer process of six

k-point mesh	Cutoff energy (eV)	Lattice energy / H_2O (eV)
$1 \times 1 \times 2$	300	-0.666
	400	-0.671
	415	-0.669
	500	-0.665
	600	-0.665
	700	-0.665
$4 \times 4 \times 8$	1000	-0.672

Table 6.1: Convergence of the lattice energy per water molecule of our ice structure with respect to increasing the **k**-point mesh density and the plane-wave cutoff energy.

hydrogens in a hexamer of ice is identified, involving large movement of the water molecules and a high barrier of 900 meV (600 meV when ZPE is included). In the first stage of the transition we find that the hexagon shrinks (the O$-$O bond length reduces from 2.74 Å to 2.48 Å) decreasing the proton transfer barrier height and width, until the protons are able to hop to their neighbouring oxygen atom. Finally the hexagon returns to the equilibrium size. These stages are shown in Fig. 6.2, and the corresponding energy profile for this transition path is shown in Fig. 6.3. The ZPE effects on the barrier height are included approximately by considering the difference between the harmonic frequencies at the IS and the TS. A regular GGA such as PBE will often underestimate the barriers involved in the breaking of covalent bonds due to self-interaction errors [210]. For this reason we used MP2 to benchmark the barrier height by comparing the barrier for an equivalent concerted proton transfer process for a single gas phase cyclic hexamer with PBE and MP2. The PBE barrier was 400 meV less than MP2, which suggests the PBE barrier in ice is underestimated by a similar amount. Along this MEP for the direct proton transfer there is a lot of oxygen movement, so we checked the barrier with fixed oxygens however this resulted in a very high barrier (3 eV). It is clear that tunnelling will not be likely along these paths (it is simple to see this by applying the WKB approxi-

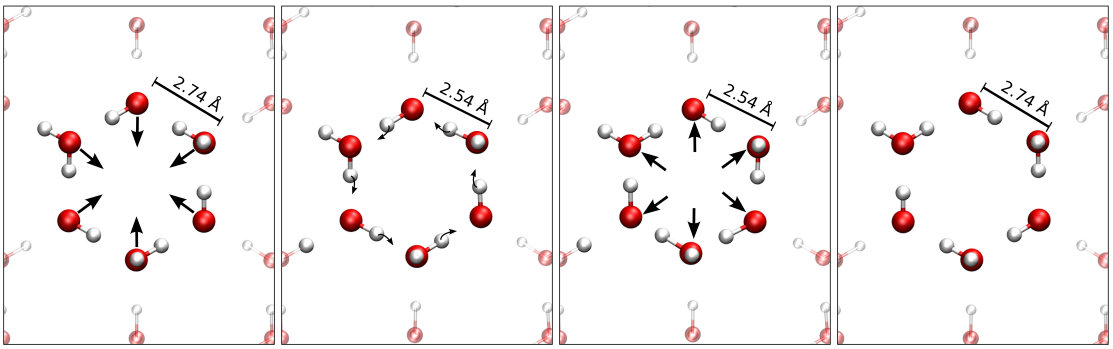

Figure 6.2: Concerted transfer of 6 protons in a loop. The arrows indicate the breathing motion of the ring. The transition process here consists of three steps: squeezing of the ice hexamer, a hopping of the hydrogens and the ice hexamer expanding to its original size again. The initial O−O distance is about 2.74 Å. The MEP follows the minimum frequency mode, which promotes movement of the heavier oxygen ions. As such the O−O distance decreases down to about 2.48 Å. After the protons hop across the barrier the hexagon relaxes to the final state.

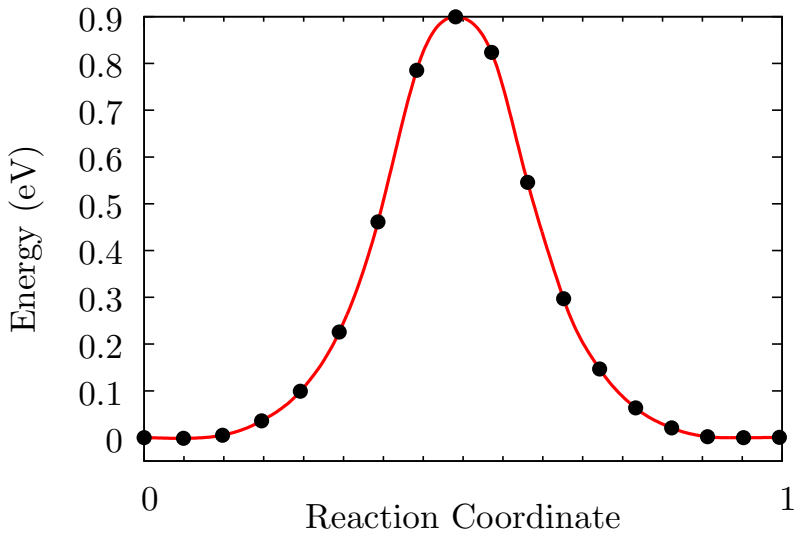

Figure 6.3: The MEP energy profile for the classical direct proton transfer as shown in Fig. 6.2. This is generated from a NEB calculation using 16 images interpolated by a cubic spline. The energies here are classical DFT energies not inclusive of ZPE. Harmonic mode calculations suggest the ZPE would lower the energy of this barrier by approximately 300 meV.

mation for tunnelling rate [1]), so we consider other transitions.

[1]By including the ZPE contribution in the frequency mode of the hexamer compression (which

The rotation of all the water molecules in a planar hexagonal ring is a simple transition which avoids the breaking of any O−H covalent bonds; instead two H-bonds per water molecule are broken. To calculate the MEP for this simple concerted rotation the NEB method was used, with trial transition state as shown in Fig. 6.4. The transition state moves away from the trial one, making the reaction coordinate a domino-like sequential transition of one water molecule rotating before the next one in the ring rotates. This leads to the temporary formation of a Bjerrum LD defect pair [211] near the TS, which is an unstable structure due to repulsive electrostatic forces, hence this process has an associated barrier of approximately 1 eV. To avoid the electrostatic repulsion of neighbouring H atoms at the transition state we now consider another process where the water molecules rotate out of the molecular plane.

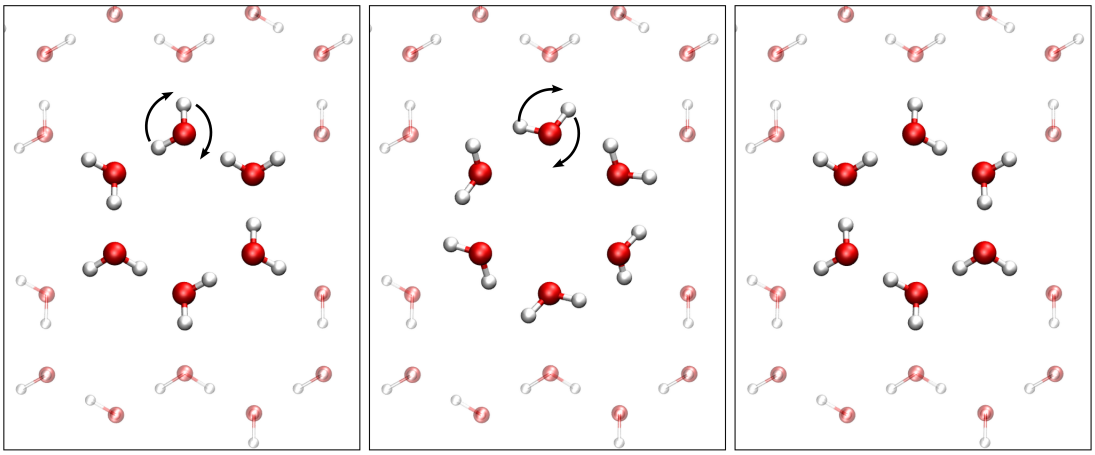

Figure 6.4: The initial state (IS), trial transition state (TS) and final state (FS) in the simple concerted rotation of the water molecules about the oxygen site. Each water molecule simultaneously rotates in-plane around the oxygen site. In this figure arrows indicate the rotation of one of the water molecules (for clarity only one set of arrows is shown, the other waters rotate in an identical fashion).

Choosing a transition where the molecules rotate out of the hexagonal plane

is essentially the first step of the classical MEP) we can estimate the amplitude of the O-O distance during this vibration. This gives a minimum O-O distance of 2.58 Å. The barrier for the hydrogens to subsequently tunnel is therefore reduced to 0.9 eV. Even this gives a rate much too low to be considered here.

leads to a process where only one H-bond is broken per water molecule in the hexamer. Due to the buckled bilayer structure of ice each H atom must only rotate through about $120°$. The initial trial transition state for this is shown in Fig. 6.5. Our NEB calculation shifts this transition to another domino effect transition with a

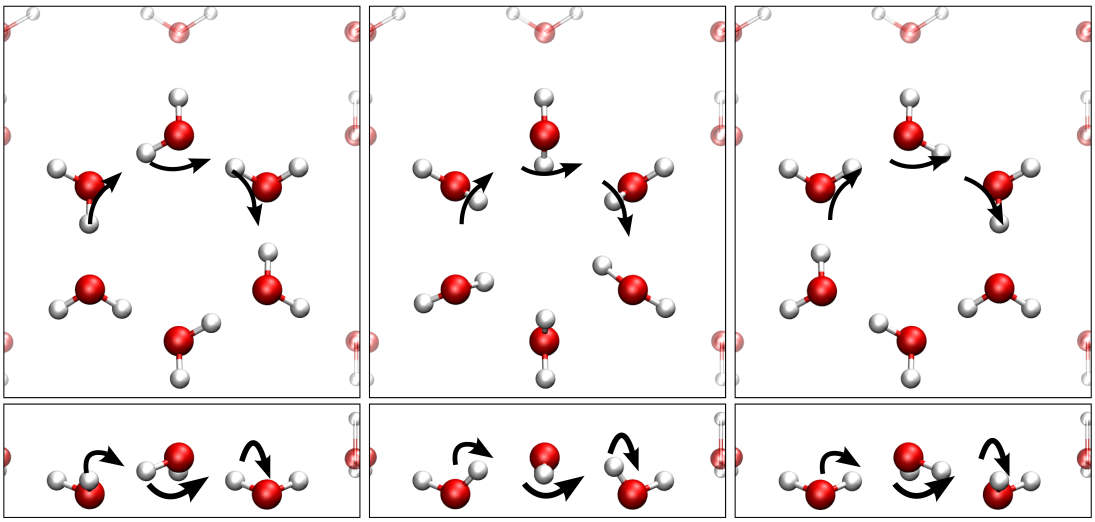

Figure 6.5: The concerted path for the out-of-plane (OOP) transition. The tunnelling hydrogens move out of the hexagon plane, so the transition state corresponds with temporarily filling the "gap" which results from the bilayer structure of ice. The arrows in this figure indicate the path moved by each hydrogen (for clarity arrows are only shown on three of the protons, in total six protons go through the same transition).

barrier of about 1 eV. The barrier to break H-bonds calculated by DFT are usually too large [212], so we once more use MP2 to check this barrier. Using a gas-phase ice hexamer and comparing the energies of the initial state and transition state with PBE and MP2 we find the PBE barrier to be higher by about 400 meV. This still leaves a 600 meV transition barrier.

As a final attempt to find a reasonable concerted proton transfer we consider a combination of Fig. 6.4 and Fig. 6.5, where half the molecules rotate in the plane about the oxygen centre, and the other half flip out of the plane. This requires the breaking of just one H-bond per water molecule and maintains a large H$-$H distance throughout the transition, which should aid in preventing the large electro-

static repulsion between the hydrogen atoms at the TS. The barrier calculated from this transition is about 1.3 eV, and as with the previous rotation based transitions the MEP involves a domino-like TS.

The transitions considered so far have been concerted and sequential transitions involving proton transfer of hydrogens around a hexagonal ring in ice Ih. All of these transitions have barriers which are too high to be reasonably considered as a probable reaction coordinate for quantum tunnelling (even at much lower rates than the 2.7×10^{11} s^{-1} reported by Bove *et al.* [77]). In addition nothing with a 0.75 Å jump length is observed. Discussions with the author revealed that their fit to the quasielastic incoherent structure factor (QISF) involved two jump distances. Although not discussed in their original publication this introduces a further two free parameters in their model (the jump distance and the amplitude), giving a total of four free parameters. Unfortunately this means the choice of jump distances 0.75 and 3.4 Å are not unique in their capacity to fit the experimental data. This puts the jump distance of 0.75 Å into question (for more details see appendix F).

In light of this, and the lack of a facile concerted tunnelling event in ice Ih we turned our efforts towards looking for the possibility of simpler transitions which could give a noticeable quasielastic neutron scattering (QENS) signal. We consider the annealing of a Bjerrum defect (Fig. 6.6) by quantum tunnelling. The structure for the defect was motivated by the DFT-converged structure from de Koning *et al.* [213].

We computed that the barrier for this defect to anneal is about 120 meV (see Fig. 6.7). A quantum tunnelling event on this barrier would require the oxygens move 0.36 Å and each hydrogen moves about 1 Å. The ZPE contribution to this barrier lowers it by 34 meV, and further slightly decreases the distance through which the hydrogen and oxygen must tunnel. If we ignore oxygen movement and treat the transition as the rotation of two hydrogens by about 60 degrees each about the oxygen we can estimate a tunnelling transmission coefficient of approximately 10^{-4} s^{-1}. Coupled with a typical atomic frequency of 10^{13} s^{-1} we can suggest that tunnelling will affect the rate of diffusion of Bjerrum defects in ice. It is possible that this

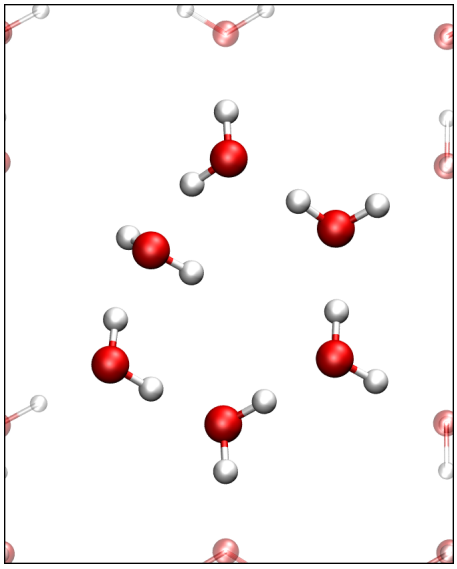

Figure 6.6: The relaxed DFT structure obtained by optimising a typical Bjerrum LD defect. This structure is 460 meV less stable than the fully relaxed ice Ih structure, although the defect remains throughout the duration of our MD and PIMD calculations at 100 K and 300 K.

effect may have been observed in the QENS experiments by Bove *et al.*, otherwise it is likely that future experiments could be used to confirm this result.

6.4 Conclusions

We have used DFT and the NEB methods to compute the energy barriers for many feasible proton transfer transitions around an ice Ih hexamer. All barriers we find are much too high to give a rate in agreement with the recent work of Bove *et al.* [77]. We look beyond a simple proton transfer around the hexamer to other effects which could be observed in a QENS experiment. In doing so we identify another transition possible when there are Bjerrum defects present in an ice sample, as there is a much lower barrier for these to anneal out than for them to form. The process for a single Bjerrum defect to anneal is a simple rotation of the affected water molecule, with a barrier of 120 meV. Using the WKB approximation we estimate a rate for this process of about 10^9 s^{-1}. It is possible that the experiments by Bove *et al.* were observing the annealing of Bjerrum defects trapped in ice.

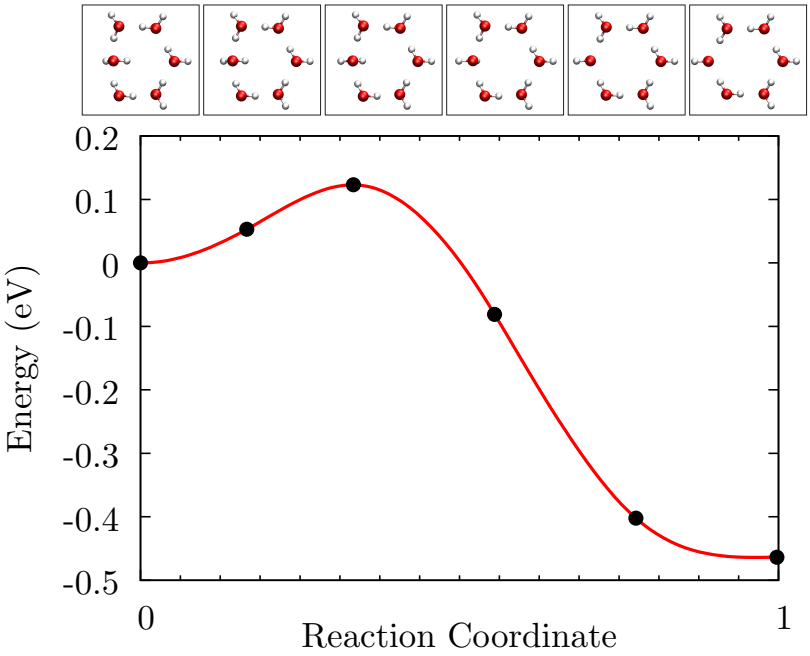

Figure 6.7: The energy profile along the MEP for the diffusion of a Bjerrum defect (as shown in Fig. 6.6) to ice Ih. The barrier is 120 meV, and the energy released by such a transition is 460 meV. The black circular dots are the NEB images used in the calculation and the smooth line a cubic spline interpolation of these using DFT forces.

Chapter 7

Summary and outlook

In this thesis various state of the art simulation methods have been used to study well-defined systems, and add to our existing understanding of how dispersion and QNEs affect hydrogen in materials.

DFT was used to study the flipping of a hydroxyl at Cu(110) between two energetically degenerate configurations. A moderate barrier for this process of about 170 meV was identified, and the MEP computed by CI-NEB was found to contain a lot of superfluous "wagging" of the oxygen atom. Since oxygen is relatively heavy any reaction coordinate containing a lot of oxygen movement will be associated with a low tunnelling probability, so instead the system tunnels along a separate direct path connecting the initial and final states on the potential energy surface. This is a phenomena known in the literature as corner-cutting of the MEP [152]. While it is easy to predict corner-cutting in a simple 2-dimensional transition just by visualising the possible reaction coordinates, in higher-dimensional systems this presents a larger challenge. Very recently methods to optimise tunnelling paths have been developed, and these will certainly be useful in the future [75, 214].

H-bonds are very important due to their prevalence in some of the most important substances, particularly DNA and water. As such there has been ongoing work to fully understand the nature of H-bonds in different situations. Chapter 4 presents a systematic study of the effects of dispersion, temperature and QNEs on the $(H_2O)_2$/Cu(110) adsorption system. This is the smallest H-bonded water cluster, but it's also a system which can be probed experimentally and for which quantum

tunnelling is thought to play a role [4, 7, 157]. The simulations showed that the strength of the H-bond in the adsorbed water dimer weakens when QNEs are included with the PIMD method, which is compatible with the recent predictions of Li *et al.* [55]. Dispersion increases the adsorption energy of the dimer, although it does not change the energetic ordering of different adsorption structures. A simple facile H-bond donor-acceptor interchange of the form suggested in [7] is not identified, and so a conclusive interpretation of the fuzzing present in the STM images measured by Kumagai *et al.* [4] remains a question for future work. Similarly a full understanding of the H-bond donor-acceptor interchange process will require a combined experimental and theoretical study on many different transition metal surfaces. In particular different surfaces will lead to different heights of the donor and acceptor water molecules, so it is important to understand what effect this has on the rate.

The roles of QNEs and dispersion on a chemisorption barrier were considered in chapter 5. The chemisorption of H at graphene is thought to be a precursor to the formation of H_2 in space, an important process within the fields of astrophysics and surface science. Traditional DFT calculations predict a barrier for this of around 200 meV which is too high to allow H chemisorption at the low temperatures of the interstellar medium. Our first finding is that dispersion (included via the vdW-DF) reduces the height of this barrier and produces a physisorption state. Since this barrier is lower and narrower than the traditional DFT barrier there was reason to believe QNEs, especially tunnelling, would be enhanced. QNEs were examined by comparing the classical free energy barrier with the quantum free energy barrier, both computed using the potential of mean force at 50 K. The physisorption state was shifted slightly (0.3 Å) away from the graphene sheet, and the quantum free energy barrier was significantly decreased. Further examination of the spread of the path-integral ring-polymer revealed this was due to the H tunnelling through the chemisorption barrier. The implications of this are significant. First H_2 formation in space may be easier than first thought since the chemisorption of H at carbonaceous materials is thought to be the rate limiting step in the process. Furthermore this suggests that the hydrogenation of graphene to produce band-gap tunable semi-

conductors may be easier. Calculating accurate physisorption energies is currently a major challenge, and we cannot expect the vdW-DF exchange-correlation functionals we used here to give the exact chemisorption barrier. It would be helpful to use, for example, the random phase approximation (RPA)[215] or diffusion quantum Monte Carlo (DMC), however this is beyond what we can do at present due to the computational challenge and the need to have a transition state structure very close to the true RPA or DMC transition state. Once an accurate estimate of the barrier is known it would be worthwhile to obtain an accurate value for the transition rate with a fully converged ring-polymer chain. A method such as ring-polymer molecular dynamics [64, 75] is ideal for this as it works well for asymmetric potentials, and includes recrossing of the barrier.

Motivated by experimental findings [77] we searched for possible proton quantum tunnelling events in ice Ih. All the barriers identified were too large for quantum tunnelling to be significant, although it is plausible that Bjerrum defects could anneal at low temperatures due to tunnelling. We have presented one issue with the experimental interpretations in appendix F, and as a result of this argue that more experiments need to be conducted to identify possible proton transfer events.

In this thesis we have made some progress in furthering the understanding of how quantum tunnelling can be important for hydrogen and H-bonds in materials. This work also outlines the general importance of a thorough combined treatment of both van der Waals dispersion and QNEs in systems where they are likely to be significant, for example the dissociative adsorption of molecules at surfaces (an important step in heterogeneous catalysis). There is a lot more work to be done to understand these effects in general, and we have highlighted further research that would be particularly useful in the near future.

Appendix A

Effect of the DFT-D3 damping function on the chemisorption barrier

A recent paper utilizing the DFT-D3 scheme observed a reduction in the height of the barrier [9] for a H atom to chemisorb at coronene. This is interesting, as it gives reasonable agreement with our results on H both at coronene and at graphene computed with the vdW-DF method. Here we demonstrate how the choice of the damping function, and damping parameters, in DFT-D3 affects the height of the barrier. The general form of the DFT-D3 dispersion correction energy term is,

$$E_{disp} = -\frac{1}{2}\sum_{A\neq B} s\frac{C_6^{AB}}{R_{AB}^6} f_{damp}(R_{AB}), \tag{A.1}$$

where s is a functional dependent scaling factor, C_6^{AB} and R_{AB} are the dispersion coefficients and internuclear distances of atomic species A and B. The damping function f_{damp} is responsible for E_{disp} diverging as R_{AB} goes to zero. There are two main damping functions used in DFT-D3. The first, which was used in the original DFT-D3 [106], reduces the dispersion correction to zero at very short distances (damping-to-zero). The second damping function, developed by Becke and Johnson (BJ) [216], reduces the dispersion energy to a constant non-zero value as $R_{AB} \to 0$ (see equation A.2).

$$E_{disp} = \frac{1}{2}\sum_{A\neq B} s_6\frac{C_6^{AB}}{R_{AB}^6 + (f(R_{AB}^0))^6} + s_8\frac{C_8^{AB}}{R_{AB}^8 + (f(R_{AB}^0))^8}, \tag{A.2}$$

with

$$f(R^0_{AB}) = a_1 R^0_{AB} + a_2, \text{ and } R^0_{AB} = \sqrt{\frac{C_8^{AB}}{C_6^{AB}}}. \tag{A.3}$$

The parameters a_1 and a_2 affect the steepness and position of the damping respectively, and these are determined from a fit to higher order data for noncovalent interactions[217]. Switching from damping-to-zero (original DFT-D3) to BJ damping reduces the chemisorption barrier relative to the physisorption well by 22 meV. We also tried making small changes to the damping function parameters ($a_{1,2}$) and found that while these gave a relatively small change in the physisorption energy they yielded a significantly larger change to the chemisorption barrier (Fig. A.1).

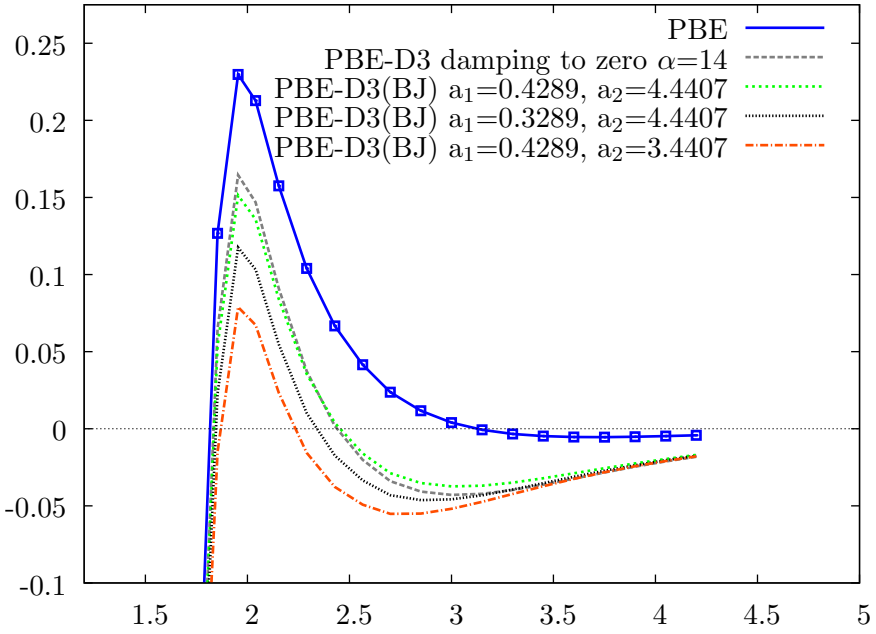

Figure A.1: The energy profile for a H atom approaching a coronene molecule at a carbon atom top core site computed with PBE and DFT-D3 with several different choices of damping function.

Appendix B

Comparison of vdW-DF exchange-correlation functionals and cell size for H at graphene

The behaviour of each of the vdW-DF we considered here is very similar, with a physisorption state predicted about 2.7 Å above the lattice and physisorption energy approximately 100 meV. In particular optPBE-vdW and optB88-vdW give binding energies that are almost identical (the difference is 3 meV). The revPBE-vdW functional gives a slightly weaker physisorption energy, consistent with revPBE exchange being more repulsive at close range and the least binding in the physisorbed state [52]. Upon considering unit cells from 3×3 to 6×6 we find essentially no dependence of the physisorbed energy on the size of the cell (Table B.1). Similarly we tested the dependence of the chemisorption barrier relative to the physisorption well on the cell size. Going from a 3×3 cell to a 5×5 cell gives a 10 meV increase in the barrier height using the optPBE-vdW exchange-correlation functional, or a 6 meV increase in the barrier height using the revPBE-vdW exchange-correlation functional.

The binding energy profiles using each of the exchange-correlation functionals are shown in B.1. The chemisorption barrier relative to the physisorption well with optPBE-vdW, optB88-vdW and revPBE-vdW are 87 meV, 86 meV and 135 meV respectively.

Supercell size	optB88-vdW	optPBE-vdW	revPBE-vdW
3×3	95	98	81
4×4	95	98	81
5×5	96	99	81
6×6	96	99	79

Table B.1: The energies (in meV) of the physisorbed state above a graphene surface computed for different supercell sizes and for different vdW-DF exchange-correlation functionals. The physisorption energy of the hollow, top, bridge and interstitial sites are equal (within 1 meV), so only the binding energy at the top site is shown here.

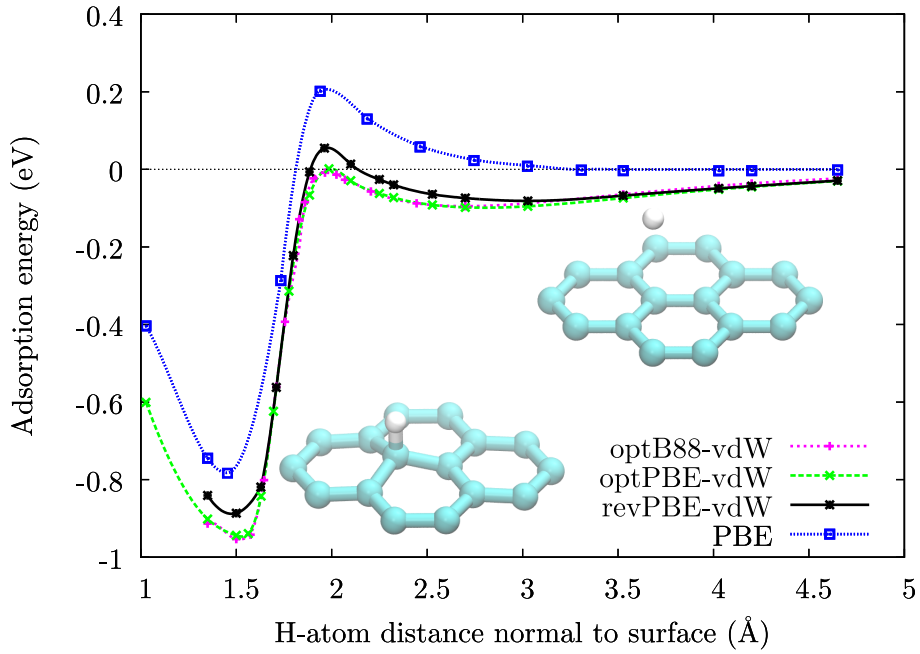

Figure B.1: Binding energy profile for a single H atom calculated with several vdW-DF and GGA based exchange-correlation functionals on a 3×3 cell. The CI-NEB method was used and the energies presented are relative to the completely desorbed hydrogen atom and clean graphene sheet. There is no physisorbed state present with PBE. The PBE calculations give a barrier of 0.2 eV, whereas methods which include dispersion give lower barriers (around 0.1 eV). The drawings show the geometries of the chemisorbed and physisorbed states. The lines connecting the data are drawn using a cubic spline interpolation.

Appendix C

Converging the number of path-integral molecular dynamics beads for H at graphene

To find out how many beads are necessary to obtain an accurate potential of mean force from PIMD, while not wasting computational resources we performed benchmark calculations with 8, 16 and 32 beads. First we tested the length of the ring-polymer (Table. C.1). Then we checked that force on the constrained centroid is comparable (Fig. C.1). We find the length of the ring-polymer is within 0.06 Å, and the force on the centroid of the H atom is similar for 8, 16 and 32 beads.

Beads	Ring-polymer length (Å)
8	0.95
16	0.89
32	0.98

Table C.1: The ring-polymer chain lengths (in Å) for PIMD calculations with the centroid constrained at 2.25 Å above the graphene surface for 8, 16 and 32 beads.

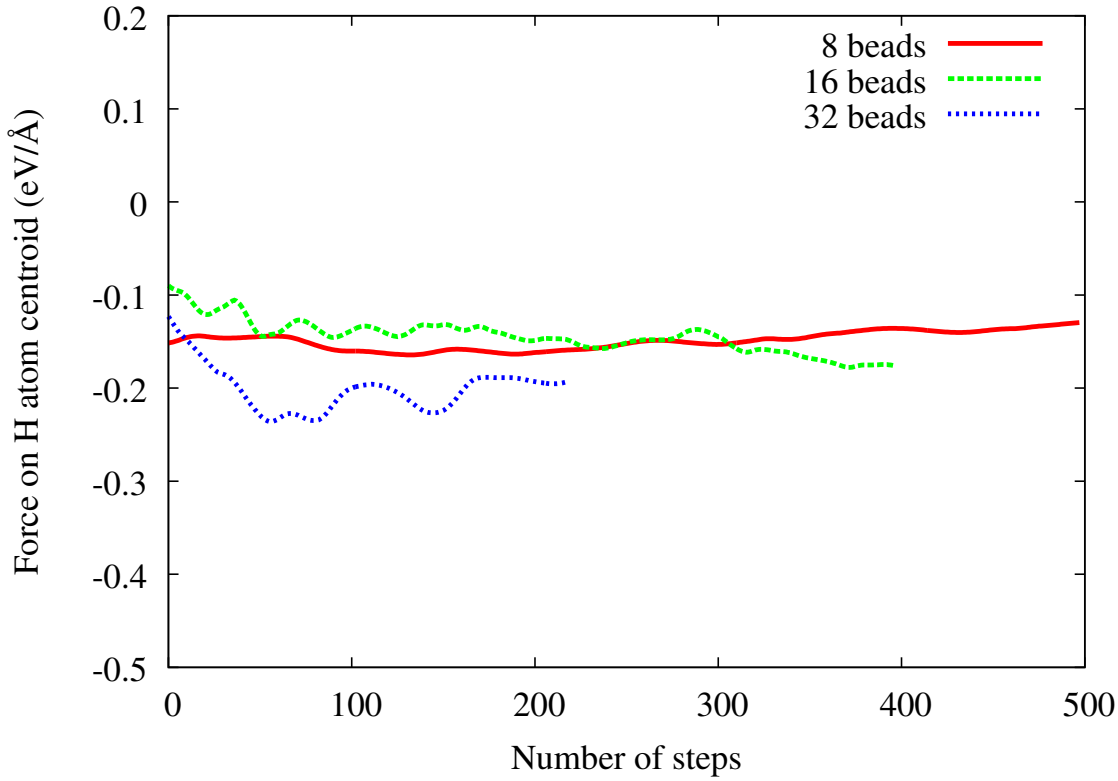

Figure C.1: The force on the centroid of the ring-polymer for both 8, 16 and 32 beads for the centroid position constrained at a height of 2.25 Å above the graphene surface.

Appendix D

Convergence of the number of HQTST beads for H at graphene

The convergence of the instanton (HQTST) calculations with the increasing number of the path-integral beads is shown in Table D.1. We used 200 beads in our calculations, which is extremely well converged relative to our reference calculations with 1000 beads.

Beads	Centroid energy (eV)	Ring-polymer length (Å)
100	0.0222	1.282
200	0.0223	1.286
1000	0.0223	1.287

Table D.1: The centroid energies (in eV) and ring-polymer chain lengths (in Å) for HQTST calculations on the optPBE-vdW barrier for 100, 200 and 1000 beads.

Appendix E

Transition state puckering of C atom effect on barrier height

If we were to do a DMC calculation on the height of the barrier we would need to use a structure taken from another method, e.g. DFT-PBE. However it is very unlikely PBE and DMC share the exact same transition state structure. Here we demonstrate that small perturbations to the puckering of the top-site carbon at the transition state give rise to large changes in the height of the chemisorption barrier (Fig. E.1), and so it is unsuitable to use the PBE structure in this case.

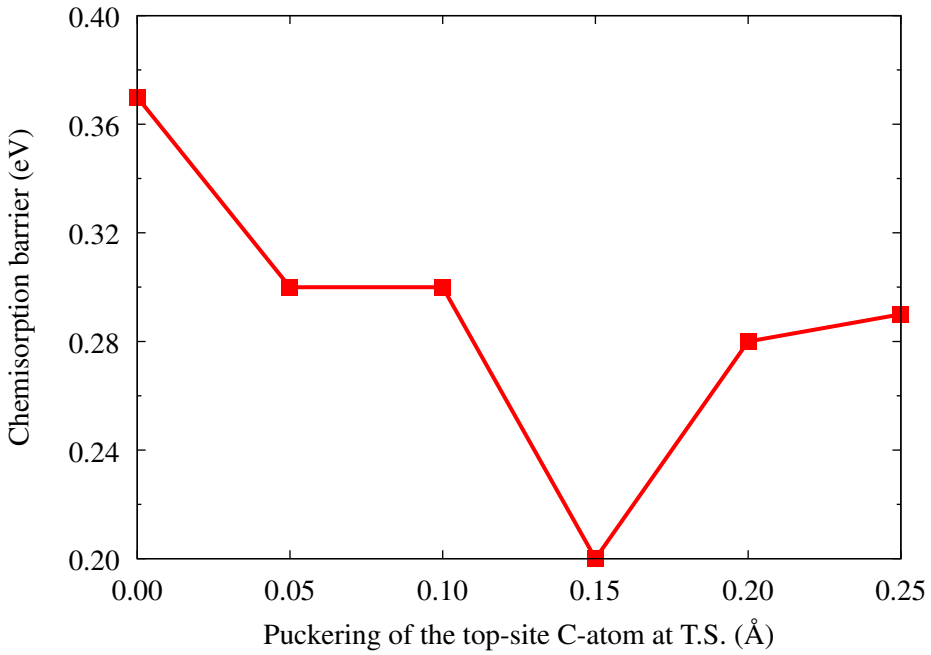

Figure E.1: The height of the chemisorption barrier for a single H atom to chemisorb at graphene for different puckering heights of the top-site carbon atom at the transition state. The barriers are calculated with PBE relative to a completely desorbed H atom at a flat graphene sheet. The point at 0.15 Å puckering and 0.2 eV barrier corresponds to the lowest energy PBE transition state.

Appendix F

Discussion of the experimentally proposed jump distance

The authors Bove *et al.* [77] argued that the proton jump distance was about 0.75 Å based on a fit of the integrated intensities from the QISF to the double well potential for a powder sample,

$$C(Q,T) = 2C(T)\left[1 - sin(Qd)/Qd\right], \tag{F.1}$$

where $C(T)$ is the product of the occupation numbers of the two sites which are separated by a distance d. I attempted to repeat the fitting by Bove *et al.*, however the form of the plot in Fig. 3 from [77] does not match the shape of Eq. F.1. From e-mails with the primary author I found that the actual equation used to fit the integrated intensities was,

$$C(Q,T) = a_1\left[1 - sin(Qd_1)/Qd_1\right] + a_2\left[1 - sin(Qd_2)/Qd_2\right], \tag{F.2}$$

where there are now two jump distances $d_{1,2}$ and two intensities $a_{1,2}$. From this equation Bove *et al.* determined jump distances of $d_1 = 0.75$ Å and $d_2 = 3.4$ Å, however 3.4 Å is an extremely large distance for a H atom to tunnel. Furthermore there are four free parameters in Eq. F.2, and so the values for $d_{1,2}$ given by Bove *et al.* are not necessarily unique. A comparison of the fits using Eq. F.1 and Eq. F.2 at 5 K are given in Fig. F.1, using the jump distances above with intensity factors $a_1 = 0.05$ and $a_2 = 0.015$.

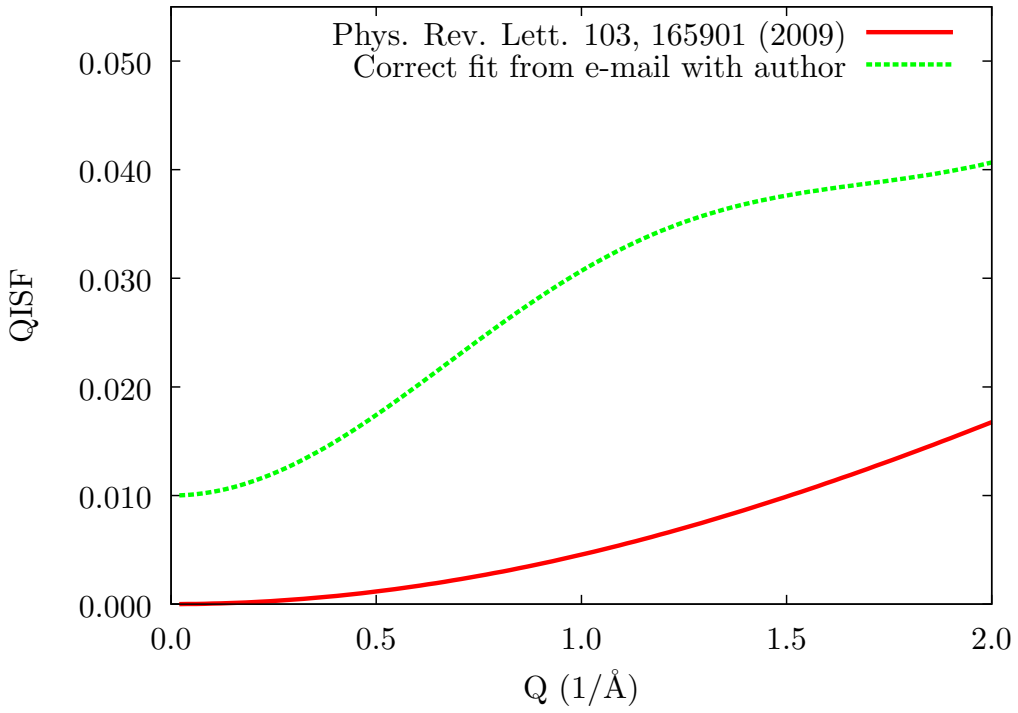

Figure F.1: The red (solid) line is the fit as presented in ref. [77] using Eq. F.1, however comparing to Fig. 3 in the same paper it is clear this fit doesn't not match the data. The green (dashed) line is the fit using Eq. F.2, which is the equation they actually used to fit their experimental data at 5 K.

Bibliography

[1] M. J. Gillan. The virtual matter laboratory. *Contemp. Phys.*, 38:115, 1997.

[2] A. Michaelides. Simulating ice nucleation, one molecule at a time, with the 'DFT microscope'. *Faraday Discuss.*, 136:287, 2007.

[3] A. Michaelides and K. Morgenstern. Ice nanoclusters at hydrophobic metal surfaces. *Nature Mater.*, 6:597, 2007.

[4] T. Kumagai, M. Kaizu, S. Hatta, H. Okuyama, T. Aruga, I. Hamada, and Y. Morikawa. Direct observation of hydrogen-bond exchange within a single water dimer. *Phys. Rev. Lett.*, 100:166101, 2008.

[5] J. Carrasco, A. Michaelides, M. Forster, S. Haq, R. Raval, and A. Hodgson. A one-dimensional ice structure built from pentagons. *Nature Mater.*, 8:427, 2009.

[6] A. Hodgson and S. Haq. Water adsorption and the wetting of metal surfaces. *Surf. Sci. Rep.*, 64:381, 2009.

[7] V. A. Ranea, A. Michaelides, R. Ramírez, P. L. de Andres, J. A. Vergés, and D. A. King. Water dimer diffusion on Pd(111) assisted by an H-bond donor-acceptor tunneling exchange. *Phys. Rev. Lett.*, 92:136104, 2004.

[8] H. Jónsson, G. Mills, and K. W. Jacobsen. *Nudged Elastic Band Method for Finding Minimum Energy Paths of Transitions*, page 385. World Scientific, 1998.

[9] N. Rougeau, D. Teillet-Billy, and V. Sidis. On the PES for the interaction of an H atom with an H chemisorbate on a graphenic platelet. *Phys. Chem. Chem. Phys.*, 13:17579, 2011.

[10] M. Bonfanti, S. Casolo, G. F. Tantardini, and R. Martinazzo. Surface models and reaction barrier in Eley-Rideal formation of H(2) on graphitic surfaces. *Phys. Chem. Chem. Phys.*, 13:16680, 2011.

[11] L. Hornekær, E. Rauls, W. Xu, Z. Šljivančanin, R. Otero, I. Stensgaard, E. Lægsgaard, B. Hammer, and F. Besenbacher. Clustering of chemisorbed H(D) atoms on the graphite (0001) surface due to preferential sticking. *Phys. Rev. Lett.*, 97:186102, 2006.

[12] L. Hornekær, Z. Šljivančanin, W. Xu, R. Otero, E. Rauls, I. Stensgaard, E. Lægsgaard, B. Hammer, and F. Besenbacher. Metastable structures and recombination pathways for atomic hydrogen on the graphite (0001) surface. *Phys. Rev. Lett.*, 96:156104, 2006.

[13] M. Bonfanti, R. Martinazzo, G. F. Tantardini, and A. Ponti. Physisorption and diffusion of hydrogen atoms on graphite from correlated calculations on the H-coronene model system. *J. Phys. Chem. C*, 111:5825, 2007.

[14] V. V. Ivanovskaya, A. Zobelli, D. Teillet-Billy, N. Rougeau, V. Sidis, and P. R. Briddon. Hydrogen adsorption on graphene: a first principles study. *Eur. Phys. J. B*, 76:481, 2010.

[15] J. Ma, A. Michaelides, and D. Alfè. Binding of hydrogen on benzene, coronene, and graphene from quantum Monte Carlo calculations. *J. Chem. Phys.*, 134:134701, 2011.

[16] M. Hirama, T. Ishida, and J. I. Aihara. Possible molecular hydrogen formation mediated by the radical cations of anthracene and pyrene. *J. Comp. Chem.*, 24:1378, 2003.

[17] R. M. Ferullo, N. F. Domancich, and N. J. Castellani. On the performance

of van der waals corrected-density functional theory in describing the atomic hydrogen physisorption on graphite. *Chem. Phys. Lett.*, 500:283, 2010.

[18] D. A. Williams, D. E. Williams, D. C. Clary, A. Farebrother, A. Fisher, J. Gingell, R. Jackman, N. Mason, A. Meijer, J. Perry, S. Price, and J. Rawlings. page 99. Cambridge Contemporary Astrophysics. Cambridge Univ Press, Cambridge, 2000.

[19] P. Ehrenfreund, H. J. Fraser, J. Blum, J. H. E. Cartwright, J. M. García-Ruiz, E. Hadamcik, A. C. Levasseur-Regourd, S. Price, F. Prodi, and A. Sarkissian. Physics and chemistry of icy particles in the universe: answers from microgravity. *Planet. Space Sci.*, 51:473, 2003.

[20] A. J. H. M. Meijer, A. J. Farebrother, D. C. Clary, and A. J. Fisher. Time-dependent quantum mechanical calculations on the formation of molecular hydrogen on a graphite surface via an EleyRideal mechanism. *J. Phys. Chem. A*, 105:2173, 2001.

[21] A. J. H. M. Meijer, A. J. Farebrother, and D. C. Clary. Isotope effects in the formation of molecular hydrogen on a graphite surface via an Eley-Rideal mechanism. *J. Phys. Chem. A*, 106:8996, 2002.

[22] A. J. H. M. Meijer, A. J. Fisher, and D. C. Clary. Surface coverage effects on the formation of molecular hydrogen on a graphite surface via an Eley-Rideal mechanism. *J. Phys. Chem. A*, 107:10862, 2003.

[23] T. P. M. Goumans and J. Kastner. Hydrogen-atom tunneling could contribute to H-2 formation in space. *Angew. Chem. Int. Ed.*, 49:7350, 2010.

[24] T. P. M. Goumans. Hydrogen chemisorption on polycyclic aromatic hydrocarbons via tunnelling. *Mon. Not. R. Astron. Soc.*, 415:3129, 2011.

[25] W. Iqbal, K. Acharyya, and E. Herbst. Kinetic monte carlo studies of H-2 formation on grain surfaces over a wide temperature range. *Astrophys. J.*, 751, 2012.

[26] M. Pozzo, C. Davies, D. Gubbins, and D. Alfè. Thermal and electrical conductivity of iron at Earth's core conditions. *Nature*, 485:355, 2012.

[27] E. Sola, J. P. Brodholt, and D. Alfè. Equation of state of hexagonal closed packed iron under Earth's core conditions from quantum Monte Carlo calculations. *Phys. Rev. B*, 79:024107, 2009.

[28] M. J. Gillan, D. Alfè, J. P. Brodholt, L. Vocadlo, and G. D. Price. First-principles modelling of Earth and planetary materials at high pressures and temperature: insights from ab-initio molecular dynamics. *Rep. Prog. Phys.*, 69:2365, 2006.

[29] D. Alfè, M. J. Gillan, and G. D. Price. The melting curve of iron at the pressures of the Earth's core from ab initio calculations. *Nature*, 401:462, 1999.

[30] D. Marx. Proton transfer 200 years after von Grotthuss: Insights from ab initio simulations. *ChemPhysChem*, 7:1848, 2006.

[31] C. J. Pickard, M. Martinez-Canales, and R. J. Needs. Density functional theory student of phase IV of solid hydrogen. *Phys. Rev. B*, 85:214114, 2012.

[32] Weerasinghe G. L., R. J. Needs, C. J. Pickard, and R. J. Needs. Computational search for iron carbide in the Earth's inner core. *Phys. Rev. B*, 84:174110, 2011.

[33] D. J. Wales and J. P. K. Doye. Global optimization by basin-hopping and the lowest energy structures of Lennard-Jones clusters contaning up to 110 atoms. *J. Phys. Chem. A*, 101:5111, 1997.

[34] D. J. Wales and H. A. Scheraga. Review: Chemistry – global optimization of clusters, and biomolecules. *Science*, 285:1368, 1999.

[35] T. S. Bush, C. R. A. Catlow, and P. D. Battle. Evolutionary programming techniques for predicting inorganic crystal–structures. *J. Mater. Chem.*, 1995.

[36] N. L. Abraham and M. I. J. Probert. A periodic genetic algorithm with real-space representation for crystal structure and polymorph prediction. *Phys. Rev. B*, 73:224104, 2006.

[37] A. R. Oganov and C. W. Glass. Crystal structure prediction using ab initio evolutionary techniques: Principles and applications. *J. Chem. Phys.*, 124:224704, 2006.

[38] G. Trimarchi and A. Zunger. Global space-group optimization problem: finding the stablest crystal structure without constraints. *Phys. Rev. B*, 75:104113, 2007.

[39] S. Ono, T. Kikegawa, and Y. Ohishi. High-pressure transition of CaCO(3). *Am. Miner.*, 92:1246, 2007.

[40] D. C. Johnson. Solid-state chemistry – new order for lithium bromide. *Nature*, 454:174, 2008.

[41] G. Hautier, A. Jain, and P. O. Shyue. From the computer to the laboratory: materials discovery and design using first-principles calculations. *J. Mater. Sci.*, 47:7317, 2012.

[42] G Ceder, Y. M. Chiang, D. R. Sadoway, M. Aydinol, , Y. I. Jang, and B. Huang. Identification of cathode materials for lithium batteries guided by first-principles calculations. *Nature*, 392:694, 1998.

[43] H. Chen, G. Hautier, A. Jain, C. Moore, B. Kang, R. Doe, L. Wu, Y. Zhu, Y. Tang, and G. Ceder. Carbonophosphates: A new family of cathode materials for Li-ion batteries identified computationally. *Chem. Mater.*, 24:2009, 2012.

[44] S. V. Alapati, J. K. Johnson, and D. K. Sholl. Identification of destabilized metal hydrides for hydrogen storage using first principles calculations.

[45] J. Lu, Z. Z. Fang, Y. J. Choi, and H. Y. Sohn. Potential of binary lithium magnesium nitride for hydrogen storage applications. *J. Phys. Chem. C*, 111:12129, 2007.

[46] J. K. Nørskov, T. Bligaard, J. Rossmeisi, and C. H. Christensen. Towards the computational design of solid catalysts. *Nature Chem.*, 1:37, 2009.

[47] J. Greeley, T. F. Jaramillo, J. Bonde, I. Chorkendorff, and J. K. Nørskov. Computational high-throughput screening of electrocatalytic materials for hydrogen evolution.

[48] T. V. Mourik and R. J. Gdanitz. A critical note on density functional theory studies on rare-gas dimers. *J. Chem. Phys.*, 116:9620, 2002.

[49] J. Vondrášek, L. Bendová, V. Klusák, and P. Hobza. Unexpectedly strong energy stabilization inside the hydrophobic core of small protein rubredoxin mediated by aromatic residues: correlated ab initio quantum chemical calculations. *J. Am. Chem. Soc.*, 127:2615, 2005. *ibid*, **127**, 8232 (2005).

[50] J. Klimeš, D. R. Bowler, and A. Michaelides. Chemical accuracy for the van der Waals density functional. *J. Phys.: Condens. Matter*, 22:022201, 2010.

[51] J. Klimeš and A. Michaelides. Advances and challenges in treating dispersion in density functional theory. *submitted*.

[52] J. Klimeš, D. R. Bowler, and A. Michaelides. Van der Waals density functionals applied to solids. *Phys. Rev. B*, 83:195131, 2011.

[53] J. Carrasco, B. Santra, J. Klimeš, and A. Michaelides. To wet or not to wet? dispersion forces tip the balance for water ice on metals. *Phys. Rev. Lett.*, 106:026101, 2011.

[54] T. J. Lawton, J. Carrasco, A. E. Baber, A. Michaelides, and E. C. H. Sykes. Visualization of hydrogen bonding and associated chirality in methanol hexamers. *Phys. Rev. Lett.*, 107:256101, 2011.

[55] X. Z. Li, B. Walker, and A. Michaelides. Quantum nature of the hydrogen bond. *Proc. Natl. Acad. Sci. U.S.A.*, 108:6369, 2011.

[56] X. Z. Li, M. I. J. Probert, A. Alavi, and A. Michaelides. Quantum nature of the proton in water-hydroxyl overlayers on metal surfaces. *Phys. Rev. Lett.*, 104:066102, 2010.

[57] M. Pavese, S. Jang, and G. A. Voth. Centroid molecular dynamics: A quantum dynamics method suitable for the parallel computer. *Parallel Comput.*, 26:1025, 2000.

[58] B. Walker and A. Michaelides. Direct assessment of quantum nuclear effects on hydrogen bond strength by constrained-centroid ab initio path integral molecular dynamics. *J. Chem. Phys.*, 133:174306, 2010.

[59] D. Alfè and M. J. Gillan. Ab initio statistical mechanics of surface adsorption and desorption. II. nuclear quantum effects. *J. Chem. Phys.*, 133:044103, 2010.

[60] J. A. Morrone and R. Car. Nuclear quantum effects in water. *Phys. Rev. Lett.*, 101:017801, 2008.

[61] B. Chen, I. Ivanov, M. L. Klein, and M. Parrinello. Hydrogen bonding in water. *Phys. Rev. Lett.*, 91:215503, 2003.

[62] M. E. Tuckerman, D. Marx, M. L. Klein, and M. Parrinello. On the quantum nature of the shared proton in hydrogen bonds. *Science*, 275:817, 1997.

[63] M. Benoit, D. Marx, and M. Parrinello. Tunnelling and zero-point motion in high-pressure ice. *Nature*, 392:258, 1998.

[64] B. J. Braams and D. E. Manolopoulos. On the short-time limit of ring polymer molecular dynamics. *J. Chem. Phys.*, 125:124105, 2006.

[65] M. Benoit, D. Marx, and M. Parrinello. Tunnelling and zero-point motion in high-pressure ice. *Nature*, 392:258–261, 1998.

[66] A. Kohen and J. P. Klinman. Enzyme catalysis: Beyond classical paradigms. *Acc. of Chem. Res.*, 31:397, 1998.

[67] A. Kohen, R. Cannio, S. Bartolucci, and J. P. Klinman. Enzyme dynamics and hydrogen tunnelling in a thermophilic alcohol dehydrogenase. *Nature*, 399:496, 1999.

[68] M. Nishijima, H. Okuyama, N. Takagi, T. Aruga, and W. Brenig. Quantum delocalization of hydrogen on metal surfaces. *Surf. Sci. Rep.*, 57:113, 2005.

[69] M. J. Gillan. Quantum simulation of hydrogen in metals. *Phys. Rev. Lett.*, 58:563, 1987.

[70] H. Okuyama, W. Siga, N. Takagi, M. Nishijima, and T. Aruga. Path and mechanism of hydrogen absorption at Pd(100). *Surf. Sci.*, 401:344, 1998.

[71] C. Zhang and A. Michaelides. Quantum nuclear effects on the location of hydrogen above and below the palladium (100) surface. *Surf. Sci.*, 605:689, 2011.

[72] W. A. Oates and A. M. Stoneham. Strain-induced interaction energies between hydrogen atoms in palladium. *J. Phys.*, F13:2424, 1983.

[73] D. Marx and M. Parrinello. Ab-initio path-integral molecular-dynamics. *Z. Phys. B*, 95:143, 1994.

[74] D. Marx and M. Parrinello. Structural quantum effects and 3-center 2-electron bonding in CH5+. *Nature*, 375:216, 1995.

[75] I. R. Craig and D. E. Manolopoulos. A refined ring polymer molecular dynamics theory of chemical reaction rates. *J. Chem. Phys.*, 123:034102, 2005.

[76] R. P. Feynman and A. R. Hibbs. *Quantum mechanics and path integrals*. McGraw-Hill Companies, 1965.

[77] L. E. Bove, S. Klotz, A. Paciaroni, and F. Sacchetti. Anomalous proton dynamics in ice at low temperatures. *Phys. Rev. Lett.*, 103:4, 2009.

[78] P. Hohenberg and W. Kohn. Inhomogeneous electron gas. *Phys. Rev*, 136:B864, 1964.

[79] W. Kohn and L. J. Sham. Self-consistent equations including exchange and correlation effects. *Phys. Rev*, 140:A1133, 1965.

[80] R. G. Parr and W. Yang. *Density-functional theory of atoms and molecules*. Oxford University Press, New York, USA, 1994.

[81] R. M. Martin. *Electronic structure: Basic theory and practical methods*. Cambridge University Press, Cambridge, UK, 2004.

[82] M. Born and R. Oppenheimer. Zur quantentheorie der molekeln. *Ann. Phys.*, 389:457, 1927.

[83] J. Behler, B. Delley, S. Lorenz, K. Reuter, and M. Scheffler. Dissociation of O_2 at Al(111): The role of spin selection rules. *Phys. Rev. Lett.*, 94:036104, 2005.

[84] J. Behler, K. Reuter, and M. Scheffler. Nonadiabatic effects in the dissociation of oxygen molecules at the Al(111) surface. *Phys. Rev. B*, 77:115421, 2008.

[85] A. C. Luntz, M. Persson, and G. O. Sitz. Theoretical evidence for nonadiabatic vibrational deexcitation in H-2(D-2) state-to-state scattering from Cu(100). *J. Chem. Phys.*, 124:4, 2006.

[86] C. Carbogno, J. Behler, K. Reuter, and A. Groß. Signatures of nonadiabatic O_2 dissociation at Al(111): First-principles fewest-switches study. *Phys. Rev. B*, 81:035410, 2010.

[87] L. H. Thomas. The calculation of atomic fields. *Math. Proc. Cambridge Philos. Soc.*, 23:542, 1927.

[88] E. Fermi. Un metodo statistico per la determinazione di alcune prioprietà dell'atomo. *Rend. Accad. Naz. Lincei*, 6:602, 1927.

[89] D. C. Langreth and J. P. Perdew. Theory of nonuniform electronic systems. I. Analysis of the gradient approximation and a generalization that works. *Phys. Rev. B*, 21:5469, 1980.

[90] D. C. Langreth and M. J. Mehl. Beyond the local-density approximation in calculations of ground-state electronic properties. *Phys. Rev. B*, 28:1809, 1983.

[91] J. P. Perdew and W. Yue. Accurate and simple density functional for the electronic exchange energy: Generalized gradient approximation. *Phys. Rev. B*, 33:8800, 1986.

[92] J. P. Perdew. Density-functional approximation for the correlation energy of the inhomogeneous electron gas. *Phys. Rev. B*, 33:8822, 1986.

[93] D. M. Ceperley and B. J. Alder. Ground-state of the electron-gas by a stochastic method. *Phys. Rev. Lett.*, 45:566, 1980.

[94] M. C. Payne, M. P. Teter, D. C. Allan, T. A. Arias, and J. D. Joannopoulos. Iterative minimization techniques for abinitio total-energy calculations - molecular-dynamics and conjugate gradients. *Rev. Mod. Phys.*, 64:1045, 1992.

[95] J. P. Perdew, K. Burke, and M. Ernzerhof. Generalized gradient approximation made simple. *Phys. Rev. Lett.*, 77:3865, 1996. $ibid$, **78**, 1396 (1997).

[96] D. Alfè and M. J. Gillan. The energetics of oxide surfaces by quantum MonteCarlo. *J. Phys. Condens. Matter*, 18:L435, 2006.

[97] J. P. Perdew, S. Kurth, Aleš Zupan, and P. Blaha. Accurate density functional with correct formal properties: A step beyond the generalized gradient approximation. *Phys. Rev. Lett.*, 82:2544, 1999. $ibid$, **82**, 5179 (1999).

[98] Jianmin Tao, John P. Perdew, Viktor N. Staroverov, and Gustavo E. Scuseria. Climbing the density functional ladder: Nonempirical meta-generalized gradient approximation designed for molecules and solids. *Phys. Rev. Lett.*, 91:146401, 2003.

[99] J. P. Perdew, A. Ruzsinszky, G. I. Csonka, L. A. Constantin, and J. Sun. Workhorse semilocal density functional for condensed matter physics and

quantum chemistry. *Phys. Rev. Lett.*, 103:026403, 2009. *ibib*, **106**, 179902 (2011).

[100] Carlo Adamo, Matthias Ernzerhof, and Gustavo E. Scuseria. The meta-GGA functional: Thermochemistry with a kinetic energy density dependent exchange-correlation functional. *J. Chem. Phys.*, 112:2643–2649, 2000.

[101] C. Adamo and V. Barone. Toward reliable density functional methods without adjustable parameters: The PBE0 model. *J. Chem. Phys.*, 110:6158, 1999.

[102] J. Heyd, G. E. Scuseria, and M. Ernzerhof. Hybrid functionals based on a screened coulomb potential. *J. Chem. Phys.*, 118:8207, 2003.

[103] P. J. Stephens, F. J. Devlin, C. F. Chabalowski, and M. J. Frisch. Ab initio calculation of vibrational absorption and circular dichroism spectra using density functional force fields. *J. Phys. Chem.*, 98:11623, 1994.

[104] S. Grimme. Accurate description of van der waals complexes by density functional theory including empirical corrections. *J. Comput. Chem.*, 25:1463, 2004.

[105] S. Grimme. Semiempirical GGA-type density functional constructed with a long-range dispersion correction. *J. Comp. Chem.*, 27:1787, 2006.

[106] S. Grimme, J. Antony, S. Ehrlich, and H. Krieg. A consistent and accurate ab initio parametrization of density functional dispersion correction (DFT-D) for the 94 elements h-pu. *J. Chem. Phys.*, 132:154104, 2010.

[107] H. B. G. Casimir and D. Polder. The influence of retardation on the London-van der Waals forces. *Phys. Rev.*, 73:360, 1948.

[108] Alexandre Tkatchenko and Matthias Scheffler. Accurate molecular van der Waals interactions from ground-state electron density and free-atom reference data. *Phys. Rev. Lett.*, 102:073005, 2009.

[109] M. Dion, H. Rydberg, E. Schröder, D. C. Langreth, and B. I. Lundqvist. Van der Waals density functional for general geometries. *Phys. Rev. Lett.*, 92:246401, 2004.

[110] N. W. Ashcroft and N. D. Mermim. *Solid state physics*. Orlando: Harcourt, 1976.

[111] H. J. Monkhorst and J. D. Pack. Special points for Brillouin-zone integrations. *Phys. Rev. B*, 13:5188, 1976.

[112] M. C. Muoz and M. P. López Sancho. Electronic-structure calculations of the Cr/GaAs(001) interface. *Phys. Rev. B*, 41:8412, 1990.

[113] P. E. Blöchl. Projector augmented-wave method. *Phys. Rev. B*, 50:17953, 1994.

[114] H. Eyring. The activated complex in chemical reactions. *J. Chem. Phys.*, 3:107, 1935.

[115] G. Henkelman and H. Jónsson. A dimer method for finding saddle points on high dimensional potential surfaces using only first derivatives. *J. Chem. Phys.*, 111:7010, 1999.

[116] A. Heyden, A. T. Bell, and F. J. Keil. Efficient methods for finding transition states in chemical reactions: Comparison of improved dimer method and partitioned rational function optimization method. *J. Chem. Phys.*, 123:224101, 2005.

[117] A. Kuki and P. G. Wolynes. Electron-tunneling paths in proteins. *Science*, 236:1647, 1987.

[118] G. Mills, H. Jónsson, and G. K. Schenter. Reversible work transition-state theory - application to dissociative adsorption of hydrogen. *Surf. Sci.*, 324:305, 1995.

[119] G. Henkelman, B. P. Uberuaga, and H. Jónsson. A climbing image nudged elastic band method for finding saddle points and minimum energy paths. *J. Chem. Phys.*, 113:9901–9904, 2000.

[120] S. A. Trygubenko and D. J. Wales. A doubly nudged elastic band method for finding transition states. *J. Chem. Phys.*, 120:2082, 2004.

[121] R. E. Gillilan and K. R. Wilson. Shadowing, rare events, and rubber bands - a variational verlet algorithm for molecular-dynamics. *J. Chem. Phys.*, 97:1757, 1992.

[122] M. J. Gillan. Quantum-classical crossover of the transition rate in the damped double well. *J. Phys, C*, 20:3621, 1987.

[123] D. E. Makarov and M. Topaler. Quantum transition-state theory below the crossover temperature. *Phys. Rev. E*, 52:178, 1995.

[124] G. Mills, G.K. Schenter, D.E. Makarov, and H. Jónsson. Generalized path integral based quantum transition state theory. *Chem. Phys. Lett.*, 278:91, 1997.

[125] A. Arnaldsson. *Calculation of quantum mechanical rate constants directly from ab initio atomic forces*. PhD thesis, University of Washington, 2007.

[126] N. Metropolis, A. W. Rosenbluth, Rosenbluth M. N., and E. Teller, A. H. an Teller. Equation of state calculations by fast computing machines. *J. Chem. Phys.*, 21:1087, 1953.

[127] W. K. Hastings. Monte Carlo sampling methods using Markov chains and their applications. *Biometrika*, 57:97, 1970.

[128] M. Creutz and B. Freedman. A statistical approach to quantum-mechanics. *Ann. Phys.*, 132:427, 1981.

[129] S. Duane, A.D. Kennedy, B. J. Pendleton, and D. Roweth. Hybrid Monte Carlo. *Phys. Lett. B*, 195:216, 1987.

[130] M. E. Tuckerman, B. J. Berne, G. J. Martyna, and M. L. Klein. Efficient molecular dynamics and hybrid Monte Carlo algorithms for path integrals. *J. Chem. Phys.*, 99:2796, 1993.

[131] G. J. Martyna and A. Hughes. Molecular dynamics algorithms for path integrals at constant pressure. *J. Chem. Phys.*, 110:3275, 1999.

[132] M. E. Tuckerman. *Statistican Mechanics: Theory and Molecular Simulation*. Oxford University Press, 2010.

[133] H Kleinert. *Path Integrals in Quantum Mechanics, Statistics and Polymer Physics*. World Scientic, 1994.

[134] H. C. Andersen. Molecular-dynamics simulations at constant pressure and-or temperature. *J. Chem. Phys.*, 72:2384, 1980.

[135] B. J. Berne and D. Thirumalai. On the simulation of quantum-systems - path integral methods. *Ann. Rev. Phys. Chem.*, 37:401, 1986.

[136] M. Ceriotti, D. E. Manolopoulos, and M. Parrinello. Accelerating the convergence of path integral dynamics with a generalized Langevin equation. *J. Chem. Phys.*, 134:084104, 2011.

[137] M. Ceriotti, M. Parrinello, T. E. Markland, and D. E. Manolopoulos. Efficient stochastic thermostatting of path integral molecular dynamics. *J. Chem. Phys.*, 133:124104, 2010.

[138] T. F. Miller and D. E. Manolopoulos. Quantum diffusion in liquid water from ring polymer molecular dynamics. *J. Chem. Phys.*, 123:154504, 2005.

[139] B. Walker and A. Michaelides. Direct assessment of quantum nuclear effects on hydrogen bond strength by constrained-centroid ab initio path integral molecular dynamics. *J. Chem. Phys.*, 133:174306, 2010.

[140] Y. Fukai. *The metal-hydrogen system: basic bulk properties*. Springer Verlag, 2005.

[141] L. J. Lauhon and W. Ho. Direct observation of the quantum tunneling of single hydrogen atoms with a scanning tunneling microscope. *Phys. Rev. Lett.*, 85:4566, 2000.

[142] T. Kumagai, M. Kaizu, H. Okuyama, S. Hatta, T. Aruga, I. Hamada, and Y. Morikawa. Tunneling dynamics of a hydroxyl group adsorbed on Cu(110). *Phys. Rev. B*, 79:035423, 2009.

[143] S. J. Clark, M. D. Segall, C. J. Pickard, P. J. Hasnip, M. I. J. Probert, K. Refson, and M. C. Payne. First principles methods using CASTEP. *Zeitschrift für Kristallographie*, 220:567, 2005.

[144] G. Kresse and J. Hafner. Ab initio molecular dynamics for liquid metals. *Phys. Rev. B*, 47:558, 1993.

[145] G. Kresse and J. Hafner. Ab initio molecular-dynamics simulation of the liquid-metal–amorphous-semiconductor transition in germanium. *Phys. Rev. B*, 49:14251, 1994.

[146] G. Kresse and J. Furthmüller. Efficiency of ab-initio total energy calculations for metals and semiconductors using a plane-wave basis set. *Comp. Mater. Sci.*, 6:15, 1996.

[147] G. Kresse and J. Furthmüller. Efficient iterative schemes for ab initio total-energy calculations using a plane-wave basis set. *Phys. Rev. B*, 54:11169, 1996.

[148] F.D. Murnaghan. The compressibility of media under extreme pressures. *Proceedings of the National Academy of Sciences*, 30:244, 1944.

[149] J. Paier, M. Marsman, and G. Kresse. Why does the B3LYP hybrid functional fail for metals? *J. Chem. Phys.*, 127:10, 2007.

[150] Jr. M. W. Chase, editor. *NIST-JANAF Thermochemical Tables*. AIP, New York, 1998.

[151] J. L. F. Da Silva, C. Stampfl, and M. Scheffler. Converged properties of clean metal surfaces by all-electron first-principles calculations. *Surf. Sci.*, 600:703, 2006.

[152] B. C. Garrett, D. G. Truhlar, A. F. Wagner, and T. H. Dunning. Jr. Variational transition state theory and tunneling for a heavy–light–heavy reaction using an ab initio potential energy surface. *J. Chem. Phys.*, 78:4400, 1983.

[153] M. Dyer, C. J. Zhang, and A. Alavi. Quantum diffusion of hydrogen and isotopes in metals. *ChemPhysChem*, 6:1711, 2005.

[154] G. C. Groenenboom and H. M. Buck. Solving the discretized time-independent Schrödinger equation with the Lanczos procedure. *J. Chem. Phys.*, 92:4374, 1990.

[155] M. E. Tuckerman, D. Marx, M. L. Klein, and M. Parrinello. Efficient and general algorithms for path integral Car-Parrinello molecular dynamics. *J. Chem. Phys.*, 104:5579, 1996.

[156] J. Carrasco, A. Hodgson, and A. Michaelides. A molecular perspective of water at metal interfaces. *Nature Mater.*, 11:667, 2012.

[157] T. Mitsui, M. K. Rose, E. Fomin, D. F. Ogletree, and M. Salmeron. Water Diffusion and Clustering on Pd(111). *Science*, 297:1850, 2002.

[158] J. O. Richardson, S. C. Althorpe, and D. J. Wales. Instanton calculations of tunneling splittings for water dimer and trimer. *J. Chem. Phys.*, 135:124109, 2011.

[159] P. E. Blöchl. Projector augmented-wave method. *Phys. Rev. B*, 50:17953, 1994.

[160] S. Nosé. A unified formulation of the constant temperature molecular-dynamics methods. *J. Chem. Phys.*, 81:511, 1984.

[161] W. G. Hoover. Canonical dynamics - equilibrium phase-space distributions. *Phys. Rev. A*, 31:1695, 1985.

[162] J. Tersoff and D. R. Hamann. Theory of the scanning tunneling microscope. *Phys. Rev. B*, 31:805, 1985.

[163] S. Meng, E. G. Wang, and S. Gao. Water adsorption on metal surfaces: A general picture from density functional theory studies. *Phys. Rev B*, 69:195404, 2004.

[164] A. Michaelides, V. A. Ranea, P. L. de Andres, and D. A. King. General model for water monomer adsorption on close-packed transition and noble metal surfaces. *Phys. Rev. Lett.*, 90:216102, 2003.

[165] H. Gawronski, J. Carrasco, A. Michaelides, and K. Morgenstern. Manipulation and control of hydrogen bond dynamics in absorbed ice nanoclusters. *Phys. Rev. Lett.*, 101:136102, 2008.

[166] B. Santra, A. Michaelides, M. Fuchs, A. Tkatchenko, C. Filippi, and M. Scheffler. On the accuracy of density-functional theory exchange-correlation functionals for H bonds in small water clusters. II. The water hexamer and van der Waals interactions. *J. Chem. Phys.*, 129:14, 2008.

[167] P. Sony, P. Puschnig, D. Nabok, and C. Ambrosch-Draxl. Importance of van der waals interaction for organic molecule-metal junctions: Adsorption of thiophene on Cu(110) as a prototype. *Phys. Rev. Let.*., 99:176401, 2007.

[168] W. Lew, M. C. Crowe, C. T. Campbell, J. Carrasco, and A. Michaelides. The energy of hydroxyl coadsorbed with water on Pt(111). *J. Phys. Chem. C*, 115:23008, 2011.

[169] E. R. M. Davidson, A. Alavi, and A. Michaelides. Dynamics of quantum tunneling: Effects on the rate and transition path of OH on Cu(110). *Phys. Rev. B*, 81:153410, 2010.

[170] T. Kumagai, A. Shiotari, H. Okuyama, S. Hatta, T. Aruga, I. Hamada, T. Frederiksen, and H. Ueba. H-atom relay reactions in real space. *Nature Mater.*, 11:167, 2012.

[171] T. Kumagai, H. Okuyama, S. Hatta, T. Aruga, and I. Hamada. Water clusters on Cu(110): Chain versus cyclic structures. *J. Chem. Phys.*, 134:024703, 2011.

[172] L. Schlapbach and A. Zuttel. Hydrogen-storage materials for mobile applications. *Nature*, 414:353, 2001.

[173] D. J. Browning, M. L. Gerrard, J. B. Lakeman, I. M. Mellor, R. J. Mortimer, and M. C. Turpin. Studies into the storage of hydrogen in carbon nanofibers: Proposal of a possible reaction mechanism. *Nano Lett.*, 2:201, 2002.

[174] W. Q. Deng, X. Xu, and W. A. Goddard. New alkali doped pillared carbon materials designed to achieve practical reversible hydrogen storage for transportation. *Phys. Rev. Lett.*, 92:4, 2004.

[175] E. J. Duplock, M. Scheffler, and P. J. D. Lindan. Hallmark of perfect graphene. *Phys. Rev. Lett.*, 92:225502, 2004.

[176] D. C. Elias, R. R. Nair, T. M. G. Mohiuddin, S. V. Morozov, P. Blake, M. P. Halsall, A. C. Ferrari, D. W. Boukhvalov, M. I. Katsnelson, A. K. Geim, and K. S. Novoselov. Control of graphene's properties by reversible hydrogenation: Evidence for graphane. *Science*, 323:610, 2009.

[177] H. Kreckel, H. Bruhns, M. Cizek, S. C. O. Glover, K. A. Miller, X. Urbain, and D. W. Savin. Experimental results for H-2 formation from H^- and H and implications for first star formation. *Science*, 329:69, 2010.

[178] K. Sakimoto. Ion-molecule reactions at extremely low energies - $H^- + H^- \rightarrow H_2 + e$. *Chem. Phys. Lett.*, 164:294, 1989.

[179] D. Hollenbach and E. E. Salpeter. Surface recombination of hydrogen molecules. *Astrophys. J.*, 163:155, 1971.

[180] S. Cazaux and A. G. G. M. Tielens. Molecular hydrogen formation in the interstellar medium. *Astrophys. J.*, 575:L29, 2002.

[181] S. Cazaux and A. G. G. M. Tielens. Formation on grain surfaces. *Astrophys. J.*, 604:222, 2004.

[182] R. Martinazzo and G. F. Tantardini. Quantum study of Eley-Rideal reaction and collision induced desorption of hydrogen atoms on a graphite surface. I. H-chemisorbed case. *J. Chem. Phys.*, 124:14, 2006.

[183] X. W. Sha, B. Jackson, and D. Lemoine. Quantum studies of Eley-Rideal reactions between h atoms on a graphite surface. *J. Chem. Phys.*, 116:7158, 2002.

[184] E. Aréou, G. Cartry, J. M. Layet, and T. Angot. Hydrogen-graphite interaction: Experimental evidences of an adsorption barrier. *J. Chem. Phys.*, 134:014701, 2011.

[185] E. Rauls and L. Hornekaer. Catalyzed routes to molecular hydrogen formation and hydrogen addition reactions on neutral polycyclic aromatic hydrocarbons under interstellar conditions. *Astrophys. J.*, 679:531, 2008.

[186] H. W. Jochims, E. Ruhl, H. Baumgartel, S. Tobita, and S. Leach. Size effects on dissociation rates of polycyclic aromatic hydrocarbon cations: Laboratory studies and astophysical implications. *Astrophys. J.*, 420:307–317, 1994.

[187] T. Allain, S. Leach, and E. Sedlmayr. Photodestruction of PAHs in the interstellar medium. I. Photodissociation rates for the loss of an acetylenic group. *Astron. Astrophys.*, 305:602, 1996.

[188] Alexandre Tkatchenko and Matthias Scheffler. Accurate molecular van der Waals interactions from ground-state electron density and free-atom reference data. *Phys. Rev. Lett.*, 102:073005, 2009.

[189] M. E. Tuckerman and D. Marx. Heavy-atom skeleton quantization and proton tunneling in "intermediate-barrier" hydrogen bonds. *Phys. Rev. Lett.*, 86:4946, 2001.

[190] X. W. Sha and B. Jackson. First-principles study of the structural and energetic properties of H atoms on a graphite (0001) surface. *Surf. Sci.*, 496:318, 2002.

[191] N. Rougeau, D. Teillet-Billy, and V. Sidis. Double H atom adsorption on a cluster model of a graphite surface. *Chem. Phys. Lett.*, 431:135, 2006.

[192] Z. Šljivančanin, E. Rauls, L. Hornekær, W. Xu, F. Besenbacher, and B. Hammer. Extended atomic hydrogen dimer configurations on the graphite(0001) surface. *J. Chem. Phys.*, 131:084706, 2009.

[193] L. Jeloaica and V. Sidis. DFT investigation of the adsorption of atomic hydrogen on a cluster-model graphite surface. *Chem. Phys. Lett.*, 300:157, 1999.

[194] E. Ghio, L. Mattera, C. Salvo, F. Tommasini, and U. Valbusa. Vibrational-spectrum of H and D on the (0001) graphite surface from scattering experiments. *J. Chem. Phys.*, 73:556, 1980.

[195] K. Ando and J. T. Hynes. Molecular mechanism of HCl acid ionization in water: Ab initio potential energy surfaces and Monte Carlo simulations. *J. Phys. Chem. B*, 101:10464, 1997.

[196] D. Marx, M. E. Tuckerman, J. Hutter, and M. Parrinello. The nature of the hydrated excess proton in water. *Nature*, 397:601, 1999.

[197] T. Kumagai, M. Kaizu, H. Okuyama, S. Hatta, T. Aruga, I. Hamada, and Y. Morikawa. Symmetric hydrogen bond in a water-hydroxyl complex on Cu(110). *Phys. Rev. B*, 81:045402, 2010.

[198] P. Hänggi, P. Talkner, and M. Borkovec. Reaction-rate theory: fifty years after Kramers. *Rev. Mod. Phys.*, 62:251, 1990.

[199] D. G. Truhlar and B. C. Garrett. Variational transition-state theory. *Acc. Chem. Res.*, 13:440, 1980.

[200] C. Dellago, P. G. Bolhuis, F. S. Csajka, and D. Chandler. Transition path sampling and the calculation of rate constants. *J. Chem. Phys.*, 108:1964, 1998.

[201] V. V. Ivanovskaya, A. Zobelli, D. Teillet-Billy, N. Rougeau, V. Sidis, and P. R. Briddon. Enhanced H(2) catalytic formation on specific topological defects in interstellar graphenic dust grain models. *Phys. Rev. B*, 82:245407, 2010.

[202] W. Lew, M. C. Crowe, C. T. Campbell, J. Carrasco, and A. Michaelides. The energy of hydroxyl coadsorbed with water on Pt(111). *J. Phys. Chem. C*, 115:23008, 2011.

[203] T. Zecho, A. Güttler, X. W. Sha, D. Lemoine, B. Jackson, and J. Küppers. Abstraction of D chemisorbed on graphite(0001) with gaseous H atoms. *Chem. Phys. Lett.*, 366:188, 2002.

[204] W. F. Kuhs and M. S. Lehmann. The geometry and orientation of the water molecule in ice-Ih. *J. Phys. (Paris) Colloq.*, 48:3, 1987.

[205] K. Rottger, A. Endriss, J. Ihringer, S. Doyle, and W. F. Kuhs. Lattice-constants and thermal-expansion of H2O and D2O ice Ih between 10 and 265 K. *Acta Crystallogr. Sect. B*, 50:644, 1994.

[206] P. J. Feibelman. Lattice match in density functional calculations: ice Ih vs. beta-AgI. *Phys. Chem. Chem. Phys.*, 10:4688, 2008.

[207] B. Santra, J. Klimeš, D. Alfè, B. Slater, A. Michaelides, R. Car, and M. Scheffler. Hydrogen bonds and van der Waals forces in ice at ambient and high pressures. *Phys. Rev. Lett.*, 107:185701, 2011.

[208] Chr. Møller and M. S. Plesset. Note on an approximation treatment for many-electron systems. *Phys. Rev.*, 46:618, 1934.

[209] M. J. Frisch, G. W. Trucks, and H. B. Schlegel. Gaussian 03, Revision C.02. Gaussian, Inc., Wallingford, CT, 2004.

[210] B. G. Johnson, C. A. Gonzales, P. M. W. Gill, and J. A. Pople. A density functional study of the simplest hydrogen abstraction reaction. Effect of self-interaction correction. *Chem. Phys. Lett.*, 221:100, 1994.

[211] N. Bjerrum. Structure and properties of ice. *Science*, 115:385, 1952.

[212] J. Ireta, J. Neugebauer, M. Scheffler, A. Rojo, and M. Galvan. Density functional theory study of the cooperativity of hydrogen bonds in finite and infinite alpha-helices. *J. Phys. Chem. B*, 107:1432, 2003.

[213] M. de Koning, A. Antonelli, A. J. R. da Silva, and A. Fazzio. Orientational defects in ice Ih: An interpretation of electrical conductivity measurements. *Phys. Rev. Lett.*, 96:075501, 2006.

[214] J. O. Richardson and S. C. Althorpe. Ring-polymer molecular dynamics rate-theory in the deep-tunneling regime: Connection with semiclassical instanton theory. *J. Chem. Phys.*, 131:214106, 2009.

[215] D. Bohm and D. Pines. A collective description of electron interactions: III. coulomb interactions in a degenerate electron gas. *Phys. Rev.*, 92:609, 1953.

[216] A. D. Becke and E. R. Johnson. A density-functional model of the dispersion interaction. *J. Chem. Phys.*, 123:154101, 2005.

[217] S. Grimme, S. Ehrlich, and L. Goerigk. Effect of the damping function in dispersion corrected density functional theory. *J. Comput. Chem.*, 32:1456, 2011.